AIRCRAFT STABILITY DERIVATIVE ESTIMATION FROM FINITE ELEMENT ANALYSIS

By

DERIC AUSTIN BABCOCK

Bachelor of Science

Oklahoma State University

Stillwater, Oklahoma

2002

Submitted to the Faculty
of the Graduate College of
Oklahoma State University
in partial fulfillment of
the requirements for
the Degree of
MASTER OF SCIENCE
July, 2004

AIRCRAFT STABILITY DERIVATIVE

ESTIMATION FROM FINITE

ELEMENT ANALYSIS

Thesis Approved:

Dr. Arena
Thesis Advisor

Dr. Falk

Dr. Young

Dr. Carlozzi
Dean of the Graduate College

ACKNOWLEDGEMENTS

First, I would like to thank my wife, Caitlin, for her love and support throughout this entire process. Her patience, comfort, and encouragement made this work possible. I would also like to thank my mother, Sandy, for teaching me the importance of education and the rewards of hard work. I am astonished that you were able to raise Shane and me while working three jobs and pursuing higher education.

I would like to thank Dr. Arena for his guidance and input into my thesis. He encouraged me not to settle for a sub-par performance and helped me focus on the research objective. I also want to thank Dr. Arena, as well as the NASA Oklahoma Space Grant, for funding my research. I am greatly thankful for the F-18 surface model provided by NASA Dryden, so I would especially like to thank Tim Doyle, Ed Hahn, and Dr. Gupta.

Finally, I would like to thank all who have worked in the CASE Lab for helping lay the foundations upon which my work is based, and especially those who have been helpful during the course of this work: Anthony Boeckman, Nic Moffitt, and Charles O'Neill. Thank you all.

TABLE OF CONTENTS

LIST OF FIGURES

NOMENCLATURE

ARMA	AutoRegressive Moving Average
b	Wing Span
c	Airfoil Chord
CASE Lab	Computational AeroServoElasticity Laboratory
CFD	Computational Fluid Dynamics
C_l	Roll Moment Coefficient
C_m	Pitch Moment Coefficient
C_n	Yaw Moment Coefficient
Datcom	United States Air Force Stability and Controls Datcom
displ	Dimensionless Amplitude of Excitation Signal
FEA	Finite Element Analysis
Ma	Mach Number
MIMO	Multi-Input Multi-Output
minpt	Minimum Number of Points at Highest Frequency
NACA	National Advisory Committee for Aeronautics
NASA	National Aeronautics and Space Administration
na	Number of Force Terms in Model
nb	Number of Motion Terms in Model
np	Number of Points for Identification
npt	Number of Previous Terms

nr	Degrees of Freedom
over	Overdetermination Factor
p	Body-Fixed Roll Rate
psi	Pounds per square inch
q	Body-Fixed Pitch Rate
Q_∞	Dynamic Pressure
r	Body-Fixed Yaw Rate
RMS	Root Mean Square
STARS	STructural Analysis RoutineS
SVD	Singular Value Decomposition
t	Time
U	Free Stream Velocity
u	x-component of velocity
v	y-component of velocity
V_{max}	Dimensionless Maximum Velocity of Excitation Signal
w	z-component of velocity
α	Angle of Attack
β	Angle of Sideslip
θ	Euler Pitch Angle
ϕ	Euler Roll Angle
ρ	Density
ω	Angular Frequency / Sweep Frequency
ψ	Euler Yaw Angle

CHAPTER 1

INTRODUCTION

1.1 Background

Flight is a balancing act. For steady, level flight, all the forces and moments on the aircraft must sum to zero; this is the equilibrium, or trim, condition. However, an imbalance in forces must be created in order to maneuver the vehicle. If the aircraft requires a large force to deviate from the reference position, it will be slow to respond to pilot inputs. If instead, the vehicle requires little force to change course, then the pilot must constantly correct for minor atmospheric disturbances. A balance must be struck between resistance to disturbances and maneuverability.

The initial tendency of the system to return to equilibrium is termed static stability. The classic representation of static stability can be seen in the three images of Figure 1.1. A marble in equilibrium at the bottom of the bowl will initially try to return to the bottom if the marble is moved then released, as seen in the top left image. This is a statically stable system. In the top right image, the bowl is now inverted and the marble is balanced at the top, any disturbance will cause the marble to diverge from the equilibrium point, creating a statically unstable system. A statically neutral system is in equilibrium at every position, with no preference to a particular position, as in the bottom image.

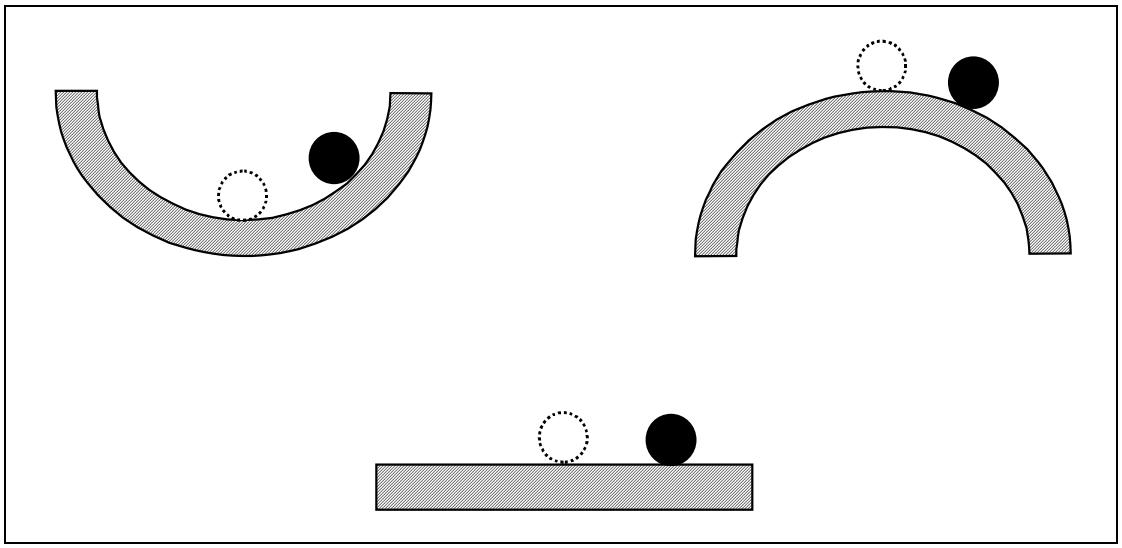

Figure 1.1: Illustration of Static Stability

Dynamic stability is another matter. While the initial response defines the static stability, the time history determines the dynamic stability. A system is dynamically stable if the amplitude of the disturbance diminishes over time, as seen in the top image of Figure 1.2. The amplitude of a disturbance in a dynamically unstable system grows with time, as illustrated in the bottom left image. Finally, the bottom right image of Figure 1.2 depicts a dynamically neutral system in which the amplitude remains constant. It is important to note that a system can be statically stable but dynamically unstable. In this case, the initial response may tend toward the equilibrium condition but overshoot and not return. A dynamically stable system must be statically stable.

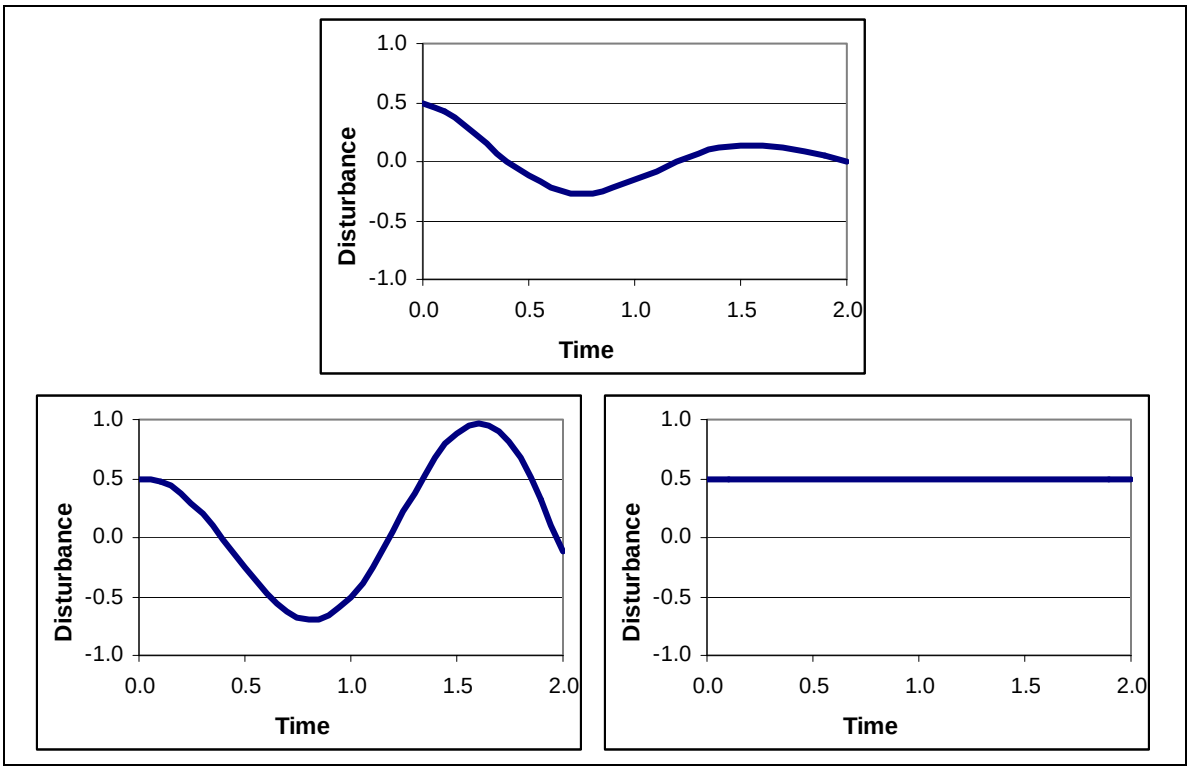

Figure 1.2: Illustration of Dynamic Stability

In order to balance the inherent stability, or instability, of an aircraft with the desire to maneuver the craft, the National Committee of Aeronautics (NACA) compared pilot evaluations with the dynamic response of the vehicle. Pilots rated a broad range of aircraft on both the amount of effort required for both steady and maneuvering flight and how comfortable the vehicle was to fly. By comparing the desired handling qualities expressed by the pilots with the physical dynamics of the aircraft, NACA determined what terms were important and established guidelines for balancing the stability and maneuverability of the vehicle based on the aircraft's stability derivatives.

Stability derivatives relate how the aerodynamic forces and moments vary with changes in the vehicle's orientation or changes in the atmosphere. G. H. Bryan first proposed the idea of expressing the forces and moments on a vehicle about the trim

condition as a function of small perturbations from the trim condition [Nelson 1998]. For example, the change in pitch moment on an aircraft could be expressed as follows:

$$\Delta M = \frac{\partial M}{\partial \alpha} \cdot \Delta\alpha + \frac{\partial M}{\partial q} \cdot \Delta q + \frac{\partial M}{\partial \delta} \cdot \Delta\delta$$

The partial derivatives in the above equation are the stability derivatives. The problem with this method is that the stability derivatives must be known before the model can be used. Hence, stability derivative estimation is important for the evaluation of handling quality and for the prediction of aerodynamic forces.

1.2 Motivation

The motivation for the current study is to reduce the time, costs, and restrictions involved in the prediction of static and rate dependent stability derivatives. Calculating stability derivatives typically means either making estimates from empirical data and basic theory or conducting wind tunnel experiments and flight tests. Many of the drawbacks of these methods can be eliminated through computational means, which are becoming a more attractive alternative with the growing power and processing speed of modern computers.

Analytical methods, such as those outlined in the USAF Stability and Control Datcom [1978], are laden with assumptions and geometric restrictions as well as limitations on the flight regime where the equations are applicable. Many of the methods presented are empirical relations based on experiments. While the methods provided in the Datcom yield insight into the dominant terms affecting the stability of an aircraft and while this may be sufficient for the preliminary design process, more accurate results for a broader range of geometries are desired.

Time and cost are the prominent disadvantages of experimental methods. The long delay between a design decision and the results from an experiment prevent wind tunnel testing from being an effective design tool in all but the most general cases. The cost of constructing a model and testing facilities also deter the experimental method. If design changes are made or modifications are needed, cost increases yet again. Wind tunnel testing is most beneficial before flight-testing after the design is finalized. A quicker, more cost efficient method is needed to determine the effects of decisions during the design process.

In addition to safety hazards, flight-testing has many of the same drawbacks as wind tunnel testing. If the behavior of the aircraft is not fully known for a given flight regime, then a great deal of caution is needed to ensure the safety of the pilot. Correcting stability and control problems is also more costly once the aircraft is built and ready for testing than if the issues were discovered and resolved during the design process. Flight-testing is a vital step in aircraft production, but with knowledge of how design decisions will affect the stability and control of the aircraft, many problems can be avoided. With a better understanding of the aircraft's response, flight-testing can be safer and more cost efficient through the proper design of the experiment.

Improvements in the capabilities of computers and the robustness Computational Fluid Dynamics (CFD) solvers are making computational methods more useful. Changes in the design can be implemented easier in the computer model as opposed to a physical model. The costs associated with CFD calculations are also much less than those of experimental methods; and, reasonably accurate results can be obtained in a timeframe suitable for the design process. Another benefit of a computational experiment is the

ability to exactly control the inputs and measure the outputs. A computer model can be forced through oscillations that would be unsafe, or even impossible, for flight and wind tunnel tests, but necessary for proper identification of the stability derivatives. Furthermore, unlike empirical methods, CFD allows for the determination of stability derivatives of an arbitrary geometry with a minimum of assumptions; however, since CFD calculates forces through an integration of pressure, one must ensure that the pressure is solved and integrated correctly for the given problem, and that the solution is both grid and time-step converged.

1.3 Objective

The objective of this work is to investigate and implement an efficient procedure for the accurate prediction of aircraft stability derivatives using finite element analysis (FEA). This procedure should combine analytical, experimental, and computational methods in order to retain the benefits of each while reducing the overall number of limitations. The lessons and techniques learned through wind tunnel and flight tests, such as excitation signals, model forms, and fitting procedures, will be applied in a computational manner. The results of the computational experiments will then be used to find and fit the best model to the data. Once the model has been found, analytical small-disturbance theory will be used to extract the static and rate dependent stability derivatives from the model. Alterations of the above procedure may be necessary in order to maximize the benefits of the computational implementation, which is not limited by the same constraints as experimental methods.

In order to achieve this end, the procedure should be able to calculate the stability derivatives for an arbitrary geometry without any prior knowledge or estimates of the

values of the stability derivatives. Since most of today's high performance aircraft are either unconventional or carry external stores, the method should not assume any symmetry. Additionally, full advantage should be taken of any benefit that can be gained through the computational implementation of this procedure, even at the expense of a physically consistent motion as long as accuracy is maintained.

CHAPTER 2

LITERATURE REVIEW

Estimating stability derivatives with the forced oscillation technique consists of four main steps: exciting the system with a signal, recording the outputs of the flow solver, fitting a model to the data, and finally extracting derivatives from the model. This chapter presents the investigation into each of these steps and discusses the options that best utilize the benefits of computational implementation.

2.1 Flow Solvers

The accuracy of a stability derivative estimate is dependent on the accuracy of the forces calculated by the flow solver. The model is only as good as the data used to fit it. Therefore, great care should be given to the proper selection of a flow solver. While using a complex, all-encompassing CFD routine that can handle any flow regime or phenomena would be computationally inefficient; the use of an inadequate solver is futile. Due to the broad range of solvers available, this work is designed to be effective with any solver. The forms of the input and output may be different, but the methodology will be similar. To this end, the best solver is the one best suited for the flow regime of interest.

2.1.1 General Requirements

For this effort, the desired solver should be accurate over a broad range of Mach numbers and able to capture the flow physics relevant to general stability derivative

analysis. Because the emphasis is placed on regions where theory is incomplete or unavailable, the solver should be capable of analyzing compressible fluid flow with and without shockwaves. The effects of vortices and wake development are also important in stability analysis, and should therefore be included. If a forced-oscillation technique is to be used, the CFD routine must be able to calculate unsteady, time-dependent flows in a non-inertial frame.

The inclusion of viscous effects greatly increases the computational requirements and time costs of a numerical solution. While induced drag will be calculated properly with the inviscid assumption, parasitic or form drag will not be. For stability derivative determination, the values of the forces are not as important as the changes in the values of the forces. If the drag calculations are incorrect by a constant, the derivatives will be unaffected. In application, however, the inviscid assumption will affect the results to a limited degree. Berry [1986] found the inclusion of viscosity into the CFD routine had minimal impact on airfoil stability below the onset of stall. Therefore, to achieve the best estimates of the stability derivatives, a viscous solver should be used; however, for this research the effects of viscosity are neglected due to the time required to run a viscous solution and the accuracy of the inviscid assumption. If the geometry or flow regime is viscous dominated, a viscous solver may be appropriate, if not necessary. As such, these flows are to be avoided when using an inviscid solver.

An example of a viscous dominated flow would be flow separation on smooth bodies. Euler solvers can accurately model separation around sharp corners [Kandil 1990] due to the vortex domination of this type of separation. Boundary layer separation, or stall, around smooth bodies such as wings or other aerodynamically shaped bodies is

viscous dominated. For the accurate estimation of stability derivatives in areas above stall, viscosity effects must be included. However, as White [1991] stated, "As long as the angle of attack is below stall, the lift can be predicted by inviscid theory and the friction by boundary-layer theory." While viscous solvers are limited by computational expense, inviscid solvers are limited to flow regimes below the predicted onset of stall.

Although the current work is focused on rigid-body stability derivative extraction, real aircraft are flexible. This flexibility can greatly alter the vehicle's response. A general solver should have the potential for incorporating elastic analysis. The control derivatives may also need to be calculated. The ability to excite the control surfaces while maintaining the aircraft at a fixed position would allow for the similar identification of control derivatives. Likewise, the control derivative estimates could be performed both with and without elasticity; therefore, a general solver should have aeroservoelastic capability.

2.1.2 Panel Methods

Panel methods solve potential flows: flows that are incompressible, irrotational, and inviscid. These numerical routines are typically quite computationally efficient because they seek to define the boundary conditions on the body instead of solving for the whole flow field [Katz 2001]. While corrections can be added to the routine in order to account for compressibility and viscosity, they reduce the efficiency of panel methods; the compressibility corrections can only correct for low Mach number compressibility effects and cannot describe shock waves. If the reference flight condition were to have local shocks, panel methods would be incapable of capturing these effects.

Another difficulty for complex geometries is the specifications of wake panels; the location, shape, and strength of the wake panels must be specified for a unique solution. As Katz [2001] states, "[the wake's] geometry clearly affects the solution." To properly model the wake would require some prior knowledge to the location, shape, and strength of the wake. For low subsonic cases, a panel method may be adequate. Park [1999] and Pesonen [2000] investigated panel methods without and with viscosity corrections respectively, and achieved accurate results at and below a Mach number of 0.6. Compressibility corrections could not be accurately extended beyond this range. Unfortunately, theory is limited to this range as well. In order to extend prediction beyond the current limit on theory, a transonic solver is needed.

2.1.3 STARS

Developed at NASA Dryden Flight Research Center, STructural Analysis RoutineS (STARS) integrates CFD, heat transfer, aeroservoelasticity, and both static and dynamic structural routines for multidisciplinary design and analysis [Gupta 2001]. Euler3D, developed by Cowan [2003], can solve the unsteady Euler equations in a non-inertial reference frame with a time-marching, finite element routine. Through rigorous verification and validation with theoretical and experimental test cases, Euler3D has demonstrated its ability to accurately capture the relevant flow physics.

In addition to the non-inertial motion specification, STARS is also capable of simulating small amplitude motions through transpiration, which is well documented in literature. Transpiration simulates motion by changing the normal vector to the surface elements before applying the no-flow boundary conditions on wall elements. The surface flow is then forced to travel perpendicular to the altered normal vector thereby

approximating the flow around a moving surface. Stephens [1998] discusses transpiration further as well as the limits on the small amplitude assumption.

As an Euler solver, STARS can solve compressible, rotational flows over a broad range of Mach numbers, but the flow must be inviscid. The wake issues of the panel methods are minimized in this implementation as well. General knowledge of where wakes will develop is still important for the proper distribution of elements, but shape and strength issues are eliminated. Unlike panel methods, the STARS solution is independent of the unnecessary elements that increase computational costs.

A drawback to this CFD routine is that FEA solves the flow at every node in the flow field, not just surface nodes. The computational costs can become quite high for large, complex cases. As with other inviscid solvers, STARS is limited to pre-stall flight conditions. However, given the capability to achieve accurate results in the transonic regime, the computational costs may be worthwhile.

2.1.4 Piston-Perturbation Solver

Hunter [1997] used piston theory to predict the aerodynamic forces on a body in a supersonic flow. Piston theory relates the surface normal at a node on the body to the surface pressure on that node. This simple relation bypasses a great deal of computational work; however, it is not self-sufficient. For accurate results, the piston theory must be applied about a reference condition, hence a piston perturbation method. The perturbation pressure about the reference condition is a function of the steady state pressure, and the change in the normal vector as seen in the following equation.

$$\frac{p'}{p_\infty} = \frac{p_0}{p_\infty} \cdot \left[1 + \frac{\gamma - 1}{2} \cdot M_0 \cdot \sin\left(\theta' - \theta_0\right) \right]^{2 \cdot \gamma / \gamma - 1}$$

A finite-element Euler solver, such as STARS, is first used to compute the steady state solution, and then the above equation calculates the pressure changes. This extremely fast solution, as previously mentioned, is limited to the supersonic range, again where adequate theory is typically available.

2.2 Excitation Signals

In order to determine the stability derivatives, the response of the aircraft to a known input must be recorded. During forced-oscillation experiments, this input alone controls the motion of the aircraft; the CFD solver simply calculates the forces and moments acting on the body due to the motion. The signal, not the forces and moments, dictate the motion of the aircraft. Numerous excitation signals are available, but the signal must properly excite the correct terms. O'Neill [2003] investigated various signals for system identification of aeroelastic systems, and outlined the benefits of each signal. However, these signals must be reevaluated based on the requirements for stability derivative calculations instead of aeroelastic identification. The following section outlines the requirements of the excitation signal. Various signals are then evaluated on these criteria to determine the best form for the excitation signal.

2.2.1 Signal Requirements

The initial requirements of the excitation signal stem from the definition of stability derivatives and the assumptions of small disturbance theory used to extract them from the data. Namely, the vehicle must start at a steady flight condition, which requires the signal to have a from-rest initial condition. Second, the stability derivatives are assumed linear within small perturbations of the flight condition. The reference flight

condition may be in the nonlinear range, but the disturbances from this condition must be in a local linear range. This requires that the signal be capable of fully exciting the important terms to an acceptable degree while maintaining small displacements from the reference condition. In flight-testing, designing an experiment that generates a pitch rate large enough to accurately estimate the pitch damping term, C_{mq}, and keep the angle of attack in the linear range is quite difficult [Klein 1998]. However, in a numerical experiment, the pitch rate can be excited beyond the normal flight envelope for proper identification, and the angle of attack maintained at minimal values.

A final intrinsic requirement of the excitation signal is that the boundary condition specification must be physically consistent for a time accurate representation. For instance, a step change in position would create an infinite velocity, distorting the pressure calculations and the resulting forces and moments. However, a step change can be used if only the steady or quasi-steady state response is desired; the solution is no longer required to be time accurate.

Once a signal has met the above requirements, it may be judged further. In order to generate data that can be used to train the model, the excitation of the input variables must be seen in the output variables. If the input motions are excited in a manner that produces little change in the output forces, some parameters will be unidentifiable and the quality of the estimates of other parameters will be reduced [Klein 1998]. As a general rule, if the user can see the effects of an input on the output when the response is plotted, the routine which solves for the unknown parameters can as well. Klein also discovered that exciting the system through control surfaces lowered the sensitivity of the outputs to the inputs for parameter other than those associated with control derivatives. In a

computational implementation, the motion of the aircraft can be prescribed without using control surfaces. This not only improves the sensitivity of the output but also reduces the correlation of input variables; the effects of controls can be separated from the motion effects. Iliff [1997] similarly concluded that the independent excitation of inputs yields the best data for parameter identification.

In order to see the effect of the inputs, the excitation signal should contain sufficient power at useful frequencies. Since steady and quasi-steady stability derivatives are inherently low frequency, low-order terms, the power of the signal should be concentrated over these lower frequencies. However, the range of important frequencies is not clearly defined, so the power should be relatively constant over a sufficient range of low frequencies to ensure that a reduction in power does not occur at important frequencies.

Other implementation concerns include the ease with which the signal can be specified. For instance, the specification of the maximum displacement or maximum velocity should be intuitive, and the frequency range easily determined. Also of importance is the robustness of the signal; one must determine whether small changes in the description of the signal greatly alter the content of the signal. Because little may be known about the aircraft response initially, the excitation signal should be somewhat forgiving. The amount of work and computational resources required to implement a signal must be considered as well. With these requirements in mind, the next section describes the signals investigated for this study, and the results of that research.

2.2.2 Signal Characteristics

The following sections present each signal examined along with its advantages and disadvantages. This discussion forms the knowledge base on which the appropriate signal will be selected, and relies heavily on the results of O'Neill's thesis work [2003]. However, since the current effort is the identification of stability derivatives and not an aeroservoelastic system, care must be taken in extrapolating from O'Neill's results.

2.2.3 3211 Multistep

The multistep, seen in Figure 2.1, is the standard signal for wind tunnel and flight-testing experiments for numerous reasons. First, the signal is simple and easy for a pilot to input. For a numerical implementation, a series of if-statements defines the signal. Also, the multistep contains sufficient power at lower frequencies. The specification is straightforward as well; the maximum displacement is the amplitude of the square wave.

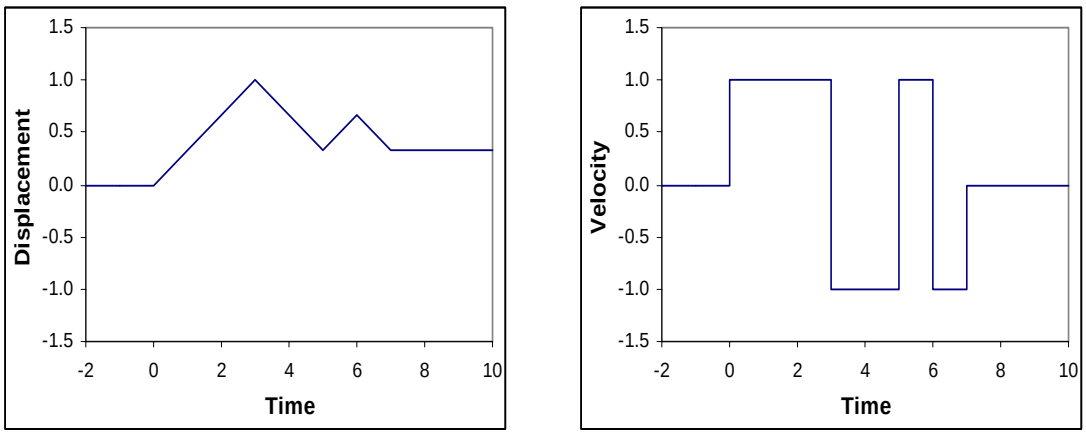

Figure 2.1: 3211 Multistep Applied to Velocity

While the 3211 has many benefits, the drawbacks are equally numerous. In experiments, the multistep is typically applied to the displacement of control surfaces, making the velocity and acceleration terms of little importance. Thus, the system can be most fully excited by a full displacement of the control surface in alternating directions.

However, to use this signal in a forced-oscillation method, the multistep must be applied to the velocity in order to maintain a physically consistent boundary condition as discussed previously, see Figure 2.1. In this implementation, the velocity and acceleration terms are more important, and not fully excited. The model, which is later fitted to the data, will incorrectly account the nonphysical step change in velocity, leading to further errors. Regular gaps in the power spectrum of the multistep also hinder the chances of accurately exciting the necessary terms for the identification process.

2.2.4 Chirp

The chirp signal, seen in Figure 2.2, is in a class of signals that linearly sweep the frequency range. By sweeping over a specified range of frequencies, the signal avoids gaps in the power spectrum. In addition, the sinusoidal function excites the velocity and acceleration terms. As seen in the following equations, displacement oscillates with the same amplitude while the amplitude of velocity increases linearly with time and the amplitude of acceleration increase with the square of time. Since the frequency increases linearly with time, the specification of the frequency range is intuitively related to the signal length.

$$D(t) = \sin\left(\omega \cdot t^2\right)$$

$$V(t) = 2 \cdot \omega \cdot t \cdot \cos\left(\omega \cdot t^2\right)$$

$$A(t) = 2 \cdot \omega \cdot \cos\left(\omega \cdot t^2\right) - 4 \cdot \omega^2 \cdot t^2 \cdot \sin\left(\omega \cdot t^2\right)$$

Referring to the example given in Section 2.2.1, this signal allows for ample excitation of pitch rate while maintaining a minimal angle of attack change. That the continuous

function specifies physically consistent boundary conditions with no step change is yet another benefit to using a chirp signal.

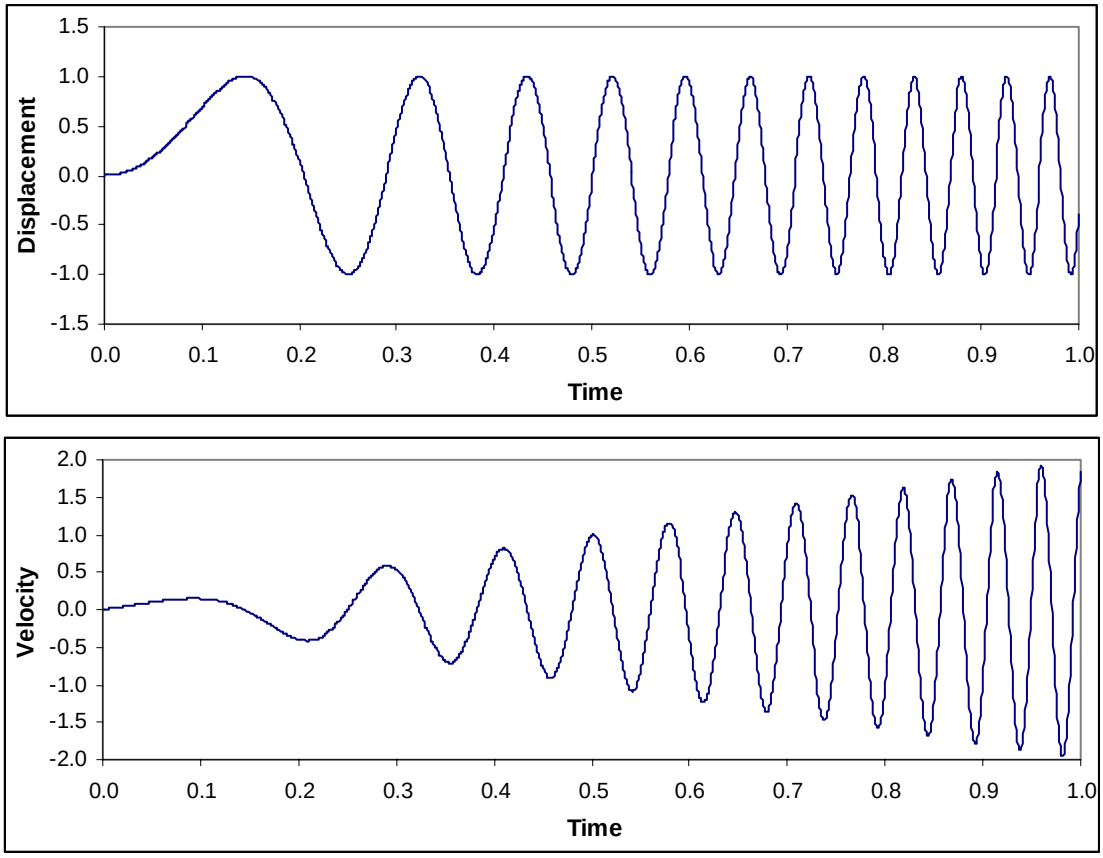

Figure 2.2: Chirp Excitation Signal

The major disadvantage of the chirp is its lack of power at the lower frequencies. While the amount of power over the lower range of frequencies is relatively constant, it is still insufficient. For the proper identification of the aircraft stability derivatives, more power must be applied in the low-frequency range. This is especially critical for the displacement terms that tend to dominate the lower frequencies, as well as the velocity terms that tend to dominate the higher frequencies.

2.2.5 DC-Chirp

The dc-chirp, seen in Figure 2.3, is very similar to the original chirp, and has many of the same benefits. However, the dc-chirp differs in the offset, providing more power in the displacement at lower frequencies. The defining equations for the dc-chirp are as follows.

$$D(t) = \frac{1}{2} \cdot \left[1 - \cos\left(\omega \cdot t^2\right)\right]$$

$$V(t) = \omega \cdot t \cdot \sin\left(\omega \cdot t^2\right)$$

$$A(t) = \omega \cdot \sin\left(\omega \cdot t^2\right) + 2 \cdot \omega^2 \cdot t^2 \cdot \cos\left(\omega \cdot t^2\right)$$

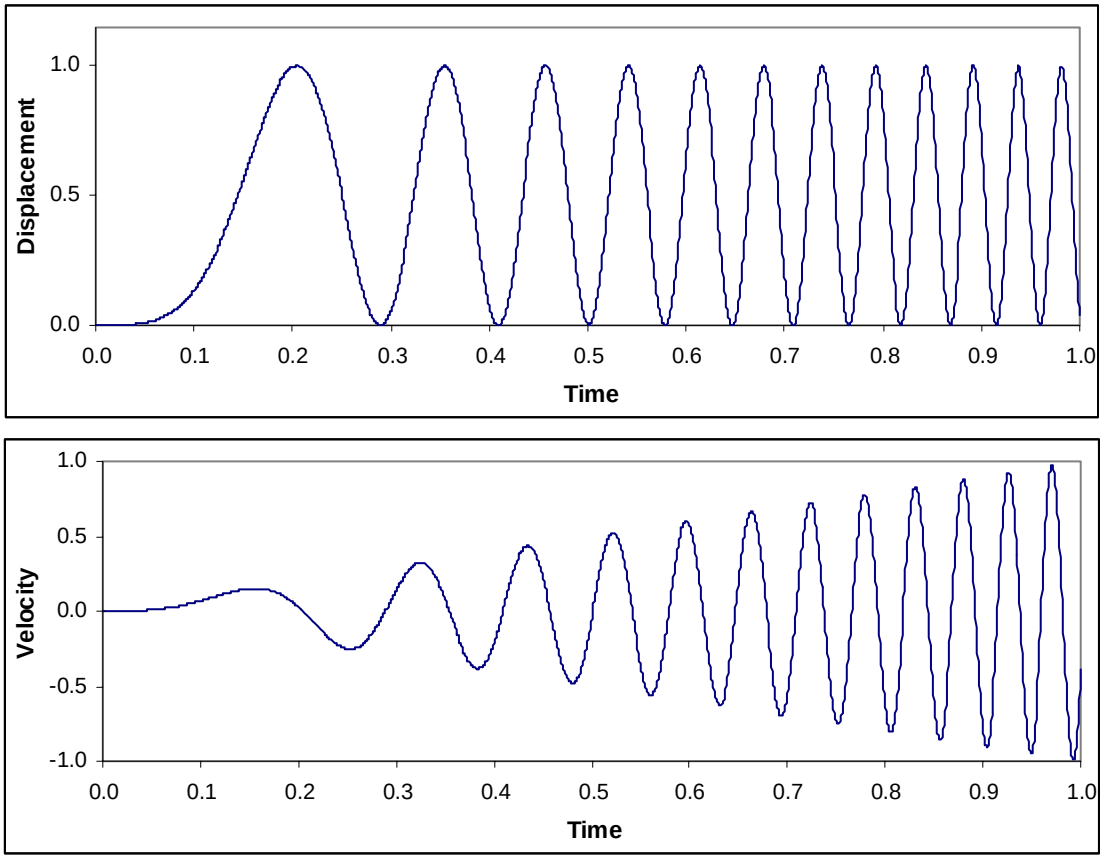

Figure 2.3: DC-Chirp Excitation Signal

As mentioned above, the offset of the dc-chirp improves the low frequency power content for displacement. However, the velocity's low frequency power content is unaffected. Since the lower frequencies are dominated by displacement terms, large power content in the velocity terms would increase the correlation between the displacement and velocity terms. The velocity terms become more important as the frequency increases, and the dc-chirp provides adequate power at these frequencies. The improved low frequency content comes at the expense of range. Since the offset moves the centerline of the dc-chirp, only positive displacements are produced. To attain the same amplitude as the original chirp, the dc-chirp would need twice the maximum value of the original chirp, pushing the small perturbation limitations.

2.2.6 Other Signals

The Fresnel and Schroeder signals were also examined but dismissed based on their failure to meet the minimum requirements. No closed form expression for the Fresnel chirp requires a numerical integration, which can lead to a noisy input signal. Any noise in the input can hinder the proper identification of the aircraft stability derivatives. The Schroeder sweep has no inherit from-rest starting condition. Since the stability derivatives are estimated about a reference condition, this signal must be adapted to accept a from-rest initial condition. O'Neill [2003] also found that the Schroeder signal was "excessively sensitive to excitation length."

2.3 Model Formulations

Once an accurate flow solver has generated the forces and moments resulting from an appropriate excitation signal, a model can be used to describe the data set. The parameters of this model reflect the trends and effects of the input on the output that are not readily apparent in the raw data. If the model cannot accurately represent the data, any stability derivatives extracted from the model will be inaccurate. Therefore, great care must be given to the proper selection of a model form.

Klein [1998] describes a good model as one that "sufficiently fits the data, facilitates the successful estimation of unknown parameters whose existence can be substantiated, and has good prediction capabilities." The model should therefore be capable of fitting a broad range of data, contain parameters that realistically relate to stability derivatives, and be accurate beyond the data used to fit the model.

2.3.1 Rigid Body Equations of Motion

The obvious equations for describing a vehicle's dynamics are the aircraft equations of motion presented in Figure 2.4 from Nelson [1998]. These equations are derived from small disturbance theory and rigid body dynamics. Typically, they are decoupled into longitudinal and lateral directions by making some general assumptions about the moments of inertia. Because this model does not work explicitly with the forced oscillation techniques previously mentioned, control surfaces or initial conditions could be used to perturb the aircraft for measurement of the response. The direct correlation of these equations to stability derivatives has made this method the standard for flight-testing and wind tunnel experiments.

$$\begin{bmatrix} \Delta\dot{u} \\ \Delta\dot{w} \\ \Delta\dot{q} \\ \Delta\dot{\theta} \end{bmatrix} = \begin{bmatrix} X_u & X_w & 0 & -g \\ Z_u & Z_w & u_0 & 0 \\ M_u + M_{\dot{w}} Z_u & M_w + M_{\dot{w}} Z_w & M_q + M_{\dot{w}} u_0 & 0 \\ 0 & 0 & 1 & 0 \end{bmatrix} \cdot \begin{bmatrix} \Delta u \\ \Delta w \\ \Delta q \\ \Delta\theta \end{bmatrix} + \begin{bmatrix} X_\delta \\ Z_\delta \\ M_\delta + M_{\dot{w}} Z_\delta \\ 0 \end{bmatrix} \cdot [\Delta\delta]$$

$$\begin{bmatrix} \Delta\dot{\beta} \\ \Delta\dot{p} \\ \Delta\dot{r} \\ \Delta\dot{\phi} \end{bmatrix} = \begin{bmatrix} \frac{Y_\beta}{u_0} & \frac{Y_p}{u_0} & \frac{Y_r}{u_0} - 1 & \frac{g \cdot \cos\theta_0}{u_0} \\ L_\beta & L_p & L_r & 0 \\ N_\beta & N_p & N_r & 0 \\ 0 & 1 & 0 & 0 \end{bmatrix} \cdot \begin{bmatrix} \Delta\beta \\ \Delta p \\ \Delta r \\ \Delta\phi \end{bmatrix} + \begin{bmatrix} 0 & \frac{Y_{\delta r}}{u_0} \\ L_{\delta a} & L_{\delta r} \\ N_{\delta a} & N_{\delta r} \\ 0 & 0 \end{bmatrix} \cdot \begin{bmatrix} \Delta\delta a \\ \Delta\delta r \end{bmatrix}$$

Figure 2.4: Longitudinal and Lateral Rigid Body Equations of Motion

The rigid body equations of motion are limited to steady or quasi-steady flows; they do not account for the unsteady terms in the aerodynamic forces that will inevitably occur due to the motion of the vehicle. The excitation required to accurately identify the rate-dependent stability derivatives also excites higher order terms. In addition, the difficulty of this model is increased when the simplifying assumptions no longer held. For example, if the aircraft has an external store beneath one wing but not the other, or if

the geometry is unconventional, the equations cannot be decoupled into longitudinal and lateral directions.

2.3.2 Indicial Functions

The indicial approach represents the forces or moments as a superposition of steps with varying amplitude. With smaller and smaller time steps, the indicial model approaches a continuous function. Klein [1997] demonstrated how the indicial function could be used to determine the stability derivatives through the integral term that models the unsteady wake effects. The following equation is the unsteady lift coefficient in indicial function form about a reference condition, as given by Klein.

$$C_L(t) = \int_0^t C_{L\alpha}(t-\tau)\cdot\frac{d}{d\tau}\alpha\cdot d\tau + \frac{l}{V}\cdot\int_0^t C_{Lq}(t-\tau)\cdot\frac{d}{d\tau}q\cdot d\tau + \ldots$$

The ellipsis was added to this equation in order to convey other terms that might be necessary for a different configuration. In the same paper, Klein also presented the following form for the time variant C_L term, while assuming pitch-acceleration was negligible.

$$C_{L\alpha}(t) = a\left(1-e^{b\cdot t}\right)+c$$

In the above equation, the change in lift coefficient with respect to angle of attack asymptotically approaches the quasi-steady value from some initial value. This formulation correlates with Wagner's unsteady lift problem, seen in Figure 2.5, with the lift initially at one-half the final steady state value.

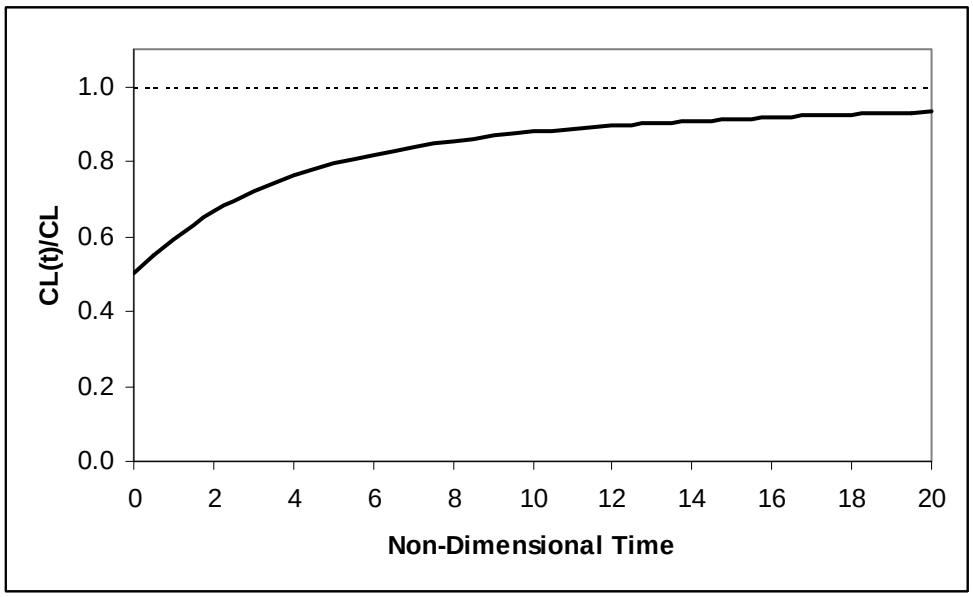

Figure 2.5: Wagner's Unsteady Lift

However, the indicial approach fails to correctly identify the stability derivatives when the assumed form is no longer valid. In some cases, the effects of the wake may not diminish exponentially. For example, the effect of the wake shed from the wing will have a decreasing influence on the aircraft forces until the wake begins to interact with the tail surfaces. The vehicle investigated in Klein's 1997 paper had a trapezoidal wing, with no surfaces aft of the wing's trailing edge. Another difficulty lies in the integro-differential form of the equations, leading to further problems identifying model parameters [Gupta 1985].

2.3.3 ARMA Model

Since the goal of this research is to develop a solution method for general geometries, the model must adequately represent a wide variety of configurations. For a model based on small disturbance theory, the following equation results for a simplified pitch case:

$$\Delta M = \frac{\Delta M}{\Delta \alpha} \cdot \Delta \alpha + \frac{\Delta M}{\Delta q} \cdot \Delta q$$

Using finite difference approximations and rearranging the equation leads to the following:

$$M(t) - M(0) = M_{\alpha} \cdot (\alpha(t) - \alpha(0)) + M_{q} \cdot \left(\frac{\alpha(t) - \cdot \alpha(t-1)}{\Delta t} - q(0) \right)$$

$$M(t) = \left[M_{\alpha} + \frac{M_{q}}{\Delta t} \right] \cdot \alpha(t) - \left[\frac{M_{q}}{\Delta t} \right] \cdot \alpha(t-1)$$

The above equation is very similar to the AutoRegressive Moving Average (ARMA) model. This model can be expanded to include all the forces and moments calculated by the CFD solver as a function of both past outputs and present and past inputs. The general form of the multi-input, multi-output (MIMO) ARMA is as follows, where y and x are column vectors and A and B are square matrices.

$$[y(t)] = \sum_{n=1}^{na} [A_n] \cdot [y(t-n)] + \sum_{m=0}^{nb-1} [B_m] \cdot [x(t-m)]$$

The challenge of the ARMA model now becomes selecting the best values for na and nb and determining the coefficients in the A and B matrices. The values for na and nb are found by generating models over a wide range, and comparing each model's output to the data. The order that most accurately matches the data produces the best

model. Several criteria can be used to determine the best match to the data, including the RMS of the error or cross correlation. If the model order does not converge, the range must be expanded. Once the best model has been found, the stability derivatives can be extracted from the coefficients in the model.

The ARMA model has been used successfully with the Euler flow solver in STARS to accurately model aeroservoelasticity over a broad range of configurations and flow regimes [Cowan 1995, Boeckman 2003, and O'Neill 2003]. The flexibility and accuracy of the ARMA model that is evident from the aeroservoelastic research could be very beneficial in stability derivative extraction. For stability derivative analysis, the inputs of the model would be rigid body rotations and displacements, instead of structural mode displacements as with the aeroelastic case.

Hollkamp [1991] and Hamel [1996] applied the ARMA model to flight-test data with limited success. Unfortunately, the noise inherent in measurement and signal generation for a physical system is a small disturbance, which the ARMA model will try to capture. In a strictly computational implementation, neither of these problems should occur, as long as the signal excites the appropriate terms, the model is valid, and the CFD solver calculates the forces properly.

2.3.4 Nonlinear Model: Stepwise Regression

Stepwise regression is very similar to the ARMA model of the previous section. Like ARMA, this model calculates forces and moments as linear sums of the state variables; however, stepwise regression does not incorporate any past inputs or outputs. Instead, the unsteady effects are modeled by nonlinear combinations of states, such as α^2 or $\alpha\beta$. The general identification process proceeds as follows: First, one must establish a

set of terms that might enter the model and fit the best linear model to the data. Next, the significance of each term is evaluated, retaining only the influential terms for the next step. Once a linear model with only the significant terms is achieved, then the nonlinear terms are added one at a time. The significance of each parameter is checked after each term is added with only dominant terms remaining.

While promising, this model has severe limitations, the primary one being that the nonlinear terms do not provide insight into the stability derivatives. Worse still, nonlinear terms could de-emphasize real linear terms in favor of unsubstantiated nonlinear terms. Even though only the significant terms are to remain in the model, Klein [1998] states, from experience, "the model can still include too many terms and have poor prediction capabilities." Another problem lies in the specification of which terms should enter the model. While the number of combinations can be reduced through engineering judgment, important terms can still be overlooked.

Nonlinear models may not be necessary. Klein [1998] found that linear models were acceptable at low angles of attack, those less than 40 degrees. At high angles of attack, separation occurs; therefore, an Euler flow solver could not properly calculate the forces in this flow regime. Klein's conclusion about nonlinear models agrees with Dowell's [1995] assessment that aerodynamic calculations using a linear model about a nonlinear condition, such as a shock wave, are sufficiently accurate. As such, nonlinear models, in general, may be ruled out as a possibility for stability derivative extraction.

2.4 Parameter Estimation Methods

Once the model form is selected, parameter estimation involves the process of determining the unknown parameters in that model from its input and output data.

Numerous, well-developed methods are available for fitting a curve to data; selecting the most appropriate one depends on the type of data and model. To this end, the following text briefly outlines the most common methods and the types of models for which they are best suited. The appropriate estimation method then results from the type of model and data, and is not a completely independent choice.

2.4.1 Maximum Likelihood Estimation

The most common parameter estimation method for fitting a model to flight-test data is a maximum likelihood estimator. This approach seeks to maximize the probability that the model will equal the measured data given a parameter value, requiring *a priori* estimates. Typically used with the rigid body equations of motion, the maximum likelihood method filters noise in both the input and output, including measurement noise. The unsteadiness is thus filtered by assuming the effects to be Gaussian white noise; however, unsteady terms are not random and "can be far from white" [Klein 1998]. Analysis of maneuvers containing unsteady transonic flow or inertial coupling of the longitudinal and lateral directions was more prone to failure [Iliff 1976].

2.4.2 Output Error Method

If no noise is present in the input, the above method simplifies to an output error method, or a Newton-Raphson method. The output error method is typically used in wind tunnel experiments where the inputs can be controlled more accurately than in flight tests. While this simplification eliminates the need for *a priori* values, output error methods still assume that the unsteady effects (the difference between the steady state

model and the unsteady data) are Gaussian white, and, as stated above, this is not always the case. If a model includes unsteady terms such that the difference in the model and the data is due only to measurement noise, then the output error approach is appropriate. However, in computational implementation, further simplifications can be made.

2.4.3 Equation Error Method

With the added assumption that the output is measured without noise, the output error method becomes the equation error method. Now that the states are measured exactly, the unsteady effects on the output are not filtered or minimized. The model must now account for the unsteady terms for the model's output to match the data in order to minimize the error. This method is so appealing it has been applied to data even when the assumptions are not valid in order to obtain initial values for the Maximum Likelihood estimator. Klein [1998] listed the main benefits of the equation error method as follows: It is a simple non-iterative method; it provides starting values for other methods; it can use partitioned data; and, it can aide in model structure determination.

The actual implementation of the equation error method to estimate the best parameters in a least squares sense can be done by Singular Value Decomposition (SVD). While SVD is more robust than other methods that typically fail due to data collinearity [Klein 1998] or very small pivot elements [Cowan 1998], less dominate terms are forced to zero in order to preserve stability. This can cause problems when trying to identify a small parameter, such as pitch damping, which has a small overall effect on force but is nonetheless an important damping term. SVD is a tool to be used in the process of identifying model parameters, therefore its development has been omitted in order to maintain focus on issues more relevant to the current work.

CHAPTER 3

METHODOLOGY

The following sections outline two methods for the estimation of stability derivatives: forced oscillation parameter identification and decoupled boundary condition specification. First, each step of the forced oscillation parameter identification – exciting the system, recording the response, identifying the model, and extracting the stability derivatives – is described in detail. Next, a discussion about decoupling the velocity and position boundary conditions is presented, as well as the derivation of a new boundary condition equation. In a similar manner, Theodorsen's equation will be reexamined in order to produce theoretical values for comparison to initial testing of the decoupled boundary condition method.

3.1 Forced Oscillation Parameter Identification

The objective for this section is to implement a computational forced oscillation technique in order to determine stability derivatives, and refine the process to take full advantage of the benefits of the CFD solver. To this end, the STARS flow solver, Euler3d, is used to calculate the forces and moments on the body resulting from the dc-chirp excitation signal. The data is then fit to an ARMA model with the stability derivatives extracted from coefficients of the model. The following sections describe the implementation of the stability derivative extraction technique.

3.1.1 CFD Solver

As stated previously, the CFD routine implemented in this research is Euler3d, which is an Euler flow solver capable of calculating compressible, inviscid flow over a broad range of Mach numbers from subsonic to supersonic in a non-inertial frame as well as through transpiration for smaller motions. For a more complete description of the implementation of STARS and Euler3d, the reader is referred to Gupta [2001] and Cowan [2003], respectively.

While the flow parameters, such as Mach number, time step, dissipation model, and solver order, are governed by the control file, the non-inertial motion of the system is controlled through the dynamic file. Since the zero order, steady state solver was developed assuming a physically consistent position and velocity relation, this solver cannot account for non-inertial motion. At the very least, a first-order, time-accurate solver must be specified in the control file when implementing the non-inertial motion specification. The first order solver requires more computational time at each time step, causing the non-inertial formulation to operate more slowly than a method based on a steady solver. When the use of non-inertial motion is specified in the control file, the dynamic output file contains the position, velocity, and acceleration of all six degrees of freedom at every time step.

Information relevant to the current work, contained in the dynamic file, includes the vector to the origin of rotation, the initial orientation and velocity, if any, and the type of excitation. The origin of rotation is also the location of the force and moment calculations in the non-inertial formulation; otherwise, the origin of the grid coordinate serves as the force and moment reference. For standard aircraft coordinates, a ψ angle of

180 degrees is specified because STARS assumes the flow travels in the positive x-direction. When a non-inertial file is implemented, the flow angles in the control file are not used by STARS and must be adjusted in the dynamic file. If stability derivative estimates are desired about an angle of attack or sideslip, then the base angles can be entered as an initial condition in the dynamic file and the dc-chirp signal can excite the system around that condition for a given excitation type. For the independent excitation type, either velocity or position can be held at the initial value while the other is excited. A different excitation type, the decoupled boundary condition specification, holds the initial position and velocity constant; even for a non-zero velocity, position is held constant. The decoupled excitation types require a modification to the acceleration equation as discussed in Section3.2.2 on page 45.

As previously discussed, transpiration simulates motion by altering the normal vector of a surface. Flow tangency is then applied to the surface defined by the new normal vector accurately modeling the actual flow for small changes in the normal vector. In order to apply transpiration to stability derivative analysis, a vector file defining the mode shapes in terms of the rigid body degrees of freedom must be generated about the origin of simulated rotation. The vector file contains the initial conditions, the excitation type, and the mode shape definition. Again, the excitation types include: dc-chirp excitation about the initial conditions, independent excitation of position and velocity, and an inconsistent hold of initial conditions. No modifications to the equations of the flow solver were required, because transpiration does not assume a physically consistent boundary condition. In addition, transpiration can be applied with the zero-order solver, increasing the speed of the stability derivative estimates. When the

use of transpiration is specified in the control file, the transpiration output file specifies the position and velocity of each mode shape at every time step.

3.1.2 Input Excitation

The dc-chirp was selected as the excitation signal based on the low frequency power content of the signal and the ability to excite high values of velocity and maintain small displacements. If the rate or velocity terms are not sufficiently excited, the parameter identification process cannot identify their effects. Should this be the case, the rate dependent derivatives will be pushed toward zero and the position derivatives altered to account for the small rate effects.

Since the dominant terms in the forces and moments are typically the angular displacement and not the angular rates, the damping effects of the rate terms can be obscured by the displacement terms in the model. In order to produce data that will facilitate the accurate estimation of the model parameters, the rate terms generally require greater excitation. The goal is not to make the rate terms dominant, but instead to increase the effect on the output due to the rate terms to such a degree that the rate influence is significant when compared to the angular terms. The displacement and velocity are not excited to the same degree; they are each excited to a degree that produces comparable output. For example, if an airfoil is pitching about a point *n*-chord lengths upstream of the leading edge and the maximum angle of attack to be excited is α, then pitch rate should be excited to a value that produces an equivalent angle of attack.

$$q = \alpha \cdot U / (n \cdot c)$$

In order to determine the stability derivatives, the signal must excite the terms in the derivative; namely, angle of attack (α), angle of sideslip (β), roll rate (p), pitch rate

(q), and yaw rate (r). However, since the angle of attack is excited with pitch rate, and sideslip with roll and yaw rates, forcing these terms would be redundant and separating their effects would difficult at best. If, instead of exciting α and β directly, the plunging velocity (w) and the side velocity (v) are excited, then α and β are excited through the plunge and side velocity respectively by the following equations.

$$\alpha = \sin^{-1}\left(\frac{w}{u}\right) \qquad \beta = \sin^{-1}\left(\frac{v}{U}\right)$$

This also allows the effects of q and $\dot{\alpha}$ to be separated from each other, as well as $\dot{\beta}$ from p and r.

As suggested by Iliff [1976] and Klein [1998], each of the five states, v, w, p, q, and r, can be excited independently. Independently exciting each of the states assists in the proper identification of the model parameters by allowing the influence of each term to be determined without the interfering effects of other states. Thus, the identified model coefficients reflect solely the intended terms and the stability derivatives extracted from the model parameters do not represent the effects of more than one state. If the states were excited simultaneously, then the correlations between the states would reduce the possibility of creating an accurate model and degrade the quality of the stability derivatives.

Parallel processing is employed in order to reduce the time required to independently generate the data for the parameter identification of each state. Instead of sequentially exciting each state, a cluster of computers is used in such a way that each computer simultaneously runs the flow solver with a different state excited. This completes the excitation of all the states in the time needed for the excitation of one state. Additionally, parallel processing eliminates the bias error that can occur in sequential

processing. This error can occur when the effects of the previous state's excitation have not dissipated before the next state begins its excitation. The reader is referred to Boeckman's [2003] work for further information on the use of either clusters or parallel processing.

With parallel processing, each state receives its own dc-chirp signal, and as such, each signal must be tailored to the state. In Euler3d, the chirp signal is defined by a non-dimensional maximum displacement (*displ*) and sweep frequency (ω). Since the chirp sweeps frequency, the maximum velocity is then determined by the length of time the signal is allowed to run. The displacement and velocity equations for the dc-chirp are repeated below.

$$D(t) = \frac{displ}{2} \cdot \left[1 - \cos\left(\omega \cdot t^2\right)\right]$$

$$V(t) = displ \cdot \omega \cdot t \cdot \sin\left(\omega \cdot t^2\right)$$

Selecting the appropriate values for *displ* and ω is relatively straightforward, but nonetheless dependent on the time step, the length of signal and the number of points required for generating the model. The first step is to decide the magnitude of the displacement, *displ*, which will provide ample excitation yet remain within the small disturbance assumptions of the stability derivatives. At higher angles of attack, a smaller displacement may be required to keep to a locally linear region. In turn, omega is found by specifying the maximum non-dimensional velocity the system is to achieve in the above velocity equation, resulting in the following equation for ω, where time is the number of points (*np*) multiplied by the non-dimensional time step (Δt).

$$\omega = \frac{V_{\max}}{displ \cdot np \cdot \Delta t}$$

The maximum value of the time step is the function of *displ*, V_{max}, and the minimum number of points needed at the highest frequency (*minpt*), as seen below. A smaller time step might be necessary for the flow solver and should be used in such cases. If one ARMA model is to be used to describe all five states simultaneously, the time step for each excitation signal must be the same; different time steps would result in a difference in the influence of previous terms. For example, with a very small time step a newly shed vortex will be very close to the trailing edge and have a high influence; whereas, with a larger time step, the vortex would be farther from the trailing edge and, therefore, have a smaller influence on the forces.

$$\Delta t = \frac{disp}{V_{\max} \cdot \min pt}$$

Typically, the value of *minpt* is selected based on the number of points required for a smooth plot of the data points; however, a large value for *minpt* with the same total number of points will reduce the frequency content of the excitation signal. The minimum number of points at the highest frequency must be well above the Nyquist frequency for the ARMA model to accurately include the effects of previous forces and motions at that frequency. Figure 3.1, below, demonstrates this with a coarse time step that is above the Nyquist frequency but is insufficient to represent a continuous function. The discrete change between two points is too large for the model to accurately represent the effects of the motion at each point. The model would incorrectly attempt to capture a non-physical step change in the flow instead of capturing the effects of the wake produced by the previous point.

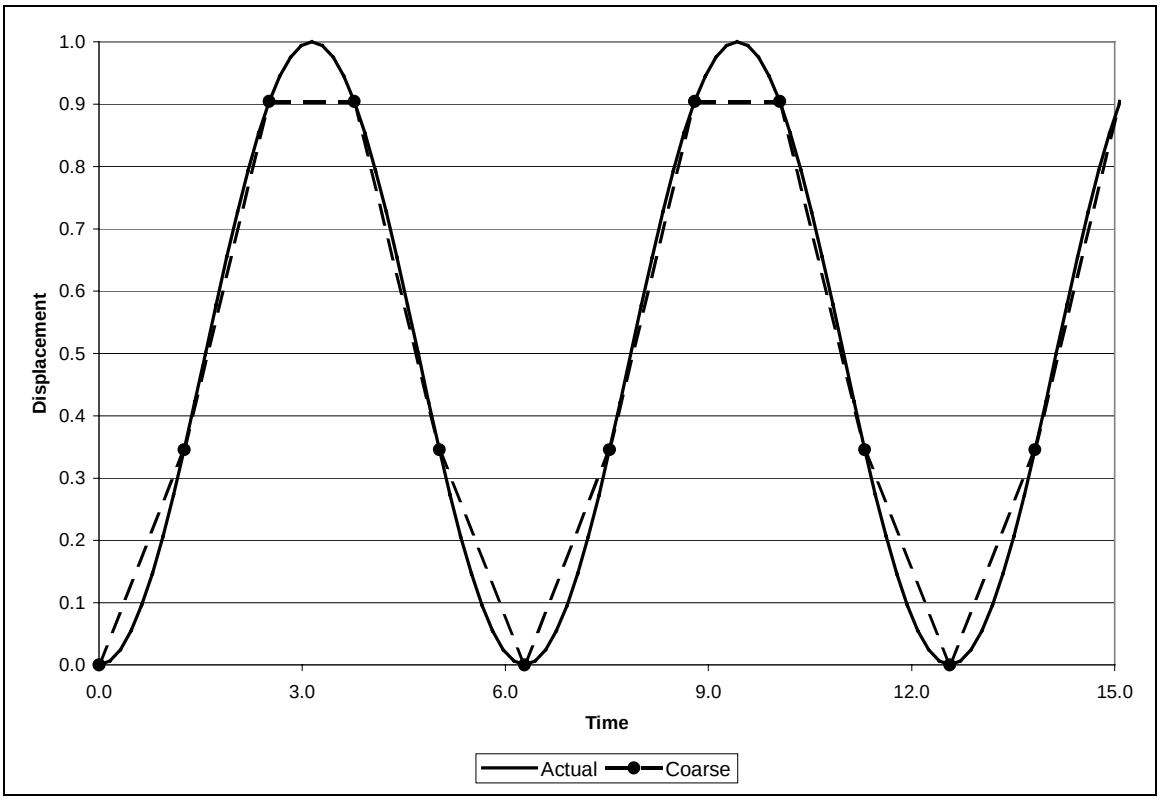

Figure 3.1: The Effects of a Large Time Step on Excitation Signal

The only remaining unknown in the calculation for ω is the number of points to be generated, np. The number of points required is solely a function of the model size and the degree of overdetermination (*over*). Because the best model size is initially unknown, np is set such that a large range of models can be examined in order to determine the best model order. The ARMA model is described by na past outputs, nb past inputs, and nr states as seen in the equation repeated below.

$$[y(t)] = \sum_{n=1}^{na} [A_n] \cdot [y(t-n)] + \sum_{m=0}^{nb-1} [B_m] \cdot [x(t-m)]$$

Since the previous inputs and outputs generated the current wake, the coefficients of these terms represent the influence of the wake on the current forces. Therefore, as a general guideline, the number of previous terms included in the model order

determination should extend to include the wake. For example, if the wake is assumed negligible n-chord lengths aft of the vehicle, then the number of previous terms (npt) can be found by the following equation, where distance is the free stream velocity multiplied by time.

$$npt = \frac{n \cdot c}{U \cdot \Delta t}$$

With a general knowledge of the size of the model, the number of data points needed for each state can be found by the following equation.

$$np = (nr \cdot nb + na) \cdot over$$

Since the model coefficients are determined in a least squared sense, better results are obtained with more data. However, the computational run time increases with an increase in the number of points to be generated. Typically, a value of 5 to 10 for the overdetermination factor is sufficient. If, in the process of determining the best model order, more data is needed to make larger models, SVD allows for the partitioning of data from different computational runs. Another signal, with only as many extra points as needed, can be generated and combined with the previous data in order to generate larger models.

3.1.3 Parameter Identification

Once the excitation data has been generated by the solver, the loads and motion terms are combined and formatted for the SVD routine for parameter identification. Cowan [1998] discusses the SVD routine and de-trending of the data to remove any offset, which cannot be represented in the ARMA model. The parameter identification process consists of gathering the generated data and formatting it for the SVD routine of

choice. Therefore, the remaining discussion will focus on determination of the number of modes to include in the model and selecting the best model size.

While the ARMA model can expand to as many degrees of freedom as are excited, the time scale of a lateral derivative may not be the same as the longitudinal term, resulting in a different optimal na-nb model for each direction. Forcing all modes to fit into a single model can result in a poor model for one mode and a better model for a more dominant mode. Instead, each degree of freedom should determine its own model size. This will, of course, increase the workload and complexity by tracking the model size for each mode, but the independent examination of each mode should provide better estimates and understanding, which could then be applied to an investigation into subsequent modes.

In order to conduct a model size sweep, each model in the range of na-nb is generated and then compared to the data. The best model can be determined based on the RMS of the error between the model and the data or the RMS of the correlation error; however, both measures can be misleading. Graphically plotting the data and the ARMA model predictions is the most reliable way to determine the best model. To plot and compare each model would be a laborious process, instead, the RMS of both means can narrow the field of candidate models and provide insight into model convergence. Some models may oscillate about the data giving a misleadingly small RMS value when in fact the model does a poor job of predicting the data. Optimally, a new data set would be generated for the RMS comparison, so that the data used to generate the models is not also used to determine the quality of the fit. However, the time involved in generating a new data set limits the application of this principle.

3.1.4 Extracting Stability Derivatives

Once the best ARMA model has been identified, extracting the steady and quasi-steady stability derivatives from the ARMA model consists of applying steady and quasi-steady conditions for the position and velocity terms and small perturbation theory for the previous force's terms. This process is best described through a demonstration on a small ARMA model with na equal to 2, nb equal to 3, and nr equal to 1. The ARMA model then has the following form:

$$Y(t) = A_1 \cdot Y(t-1) + A_2 \cdot Y(t-2) + B_0 \cdot X(t) + B_1 \cdot X(t-1) + B_2 \cdot X(t-2)$$

For the steady state terms, all the Y and X terms are constant and can be rearranged to form the following equation, where the derivative of Y with respect to X is the constant formed by the combination of model coefficients:

$$Y(t) = \frac{B_0 + B_1 + B_2}{1 - A_1 - A_2} \cdot X(t)$$

This equation can be generalized for any na-nb model size where nr is equal to one. Therefore, the steady state stability derivative for any model size can be determined by the equation below:

$$\frac{dY}{dX} = \sum_{i=0}^{nb-1} B_i \Bigg/ \left(1 - \sum_{i=1}^{na} A_i\right)$$

If the sum of A term equals unity, the resulting division by zero prevents this method from working. This condition implies a Markov sequence in which the present terms are independent of previous terms; however, in a causal relationship, present forces are dependent on previous states.

Quasi-steady stability derivates require further examination as the force and position terms are no longer constant. Position terms can be determined through a constant rate equation as follows:

$$X(t-i) = X(t) - i \cdot \Delta t \cdot \dot{X}$$

Using the above equation, the previous position terms can be found from the current position and the constant rate, essentially generating the time history of states required to achieve the current position at a constant rate.

Previous force terms in the ARMA model can be estimated through small disturbance theory, as demonstrated in the equation below:

$$Y(t-i) = Y(t) - \frac{dY}{dX} \cdot [X(t) - X(t-i)]$$

Combining the previous position equation and the previous force equation yields the following equation for the previous forces, where dY/dX is as given above:

$$Y(t-i) = Y(t) - i \cdot \Delta t \cdot \dot{X} \cdot \frac{dY}{dX}$$

By substituting the above expression and the position relation into the general ARMA model with nr equal to one and simplifying, the following equation is then produced:

$$Y(t) = X(t) \cdot \frac{\sum_{i=0}^{nb-1} B_i}{1 - \sum_{i=1}^{na} A_i} - \dot{X} \cdot \Delta t \cdot \left[\frac{\sum_{i=0}^{nb-1} B_i \cdot \sum_{i=1}^{na} A_i \cdot i}{\left[1 - \sum_{i=1}^{na} A_i \right]^2} + \frac{\sum_{i=0}^{nb-1} B_i \cdot i}{1 - \sum_{i=1}^{na} A_i} \right]$$

Therefore, the quasi-steady stability derivative for any na-nb model, where nr is equal to one, is expressed by the following:

$$\frac{dY}{d\dot{X}} = -\Delta t \cdot \left[\frac{\sum_{i=0}^{nb-1} B_i \cdot \sum_{i=1}^{na} A_i \cdot i}{\left[1 - \sum_{i=1}^{na} A_i\right]^2} + \frac{\sum_{i=0}^{nb-1} B_i \cdot i}{1 - \sum_{i=1}^{na} A_i} \right]$$

This equation may then be generalized for any order derivative of X as follows, where $X^{(0)}$ is X, and $X^{(j)}$ is the j^{th} time derivative of X:

$$\frac{dY}{dX^{(j)}} = \frac{-\Delta t^{j}}{j!} \cdot \left[\frac{\sum_{i=0}^{nb-1} B_i \cdot \sum_{i=1}^{na} A_i \cdot i^{j}}{\left[1 - \sum_{i=1}^{na} A_i\right]^2} + \frac{\sum_{i=0}^{nb-1} B_i \cdot i^{j}}{1 - \sum_{i=1}^{na} A_i} \right]$$

After identifying the parameters of the best-size ARMA model, stability derivative extraction becomes merely a process of summing coefficients, a process easily performed in a simple spreadsheet calculation.

3.2 Decoupled Boundary Conditions

The previous sections outlined the current experimental techniques implemented in a computational framework in which the ARMA model captures the unsteady effects as well as the effects of position, velocity, and higher order terms. The sole purpose of the ARMA model is to capture these effects so that each may be accurately separated from the others. Therefore, if position, velocity, and other terms were excited separately, the ARMA model would not be required, drastically simplifying the stability derivative estimation process. The goal, then, becomes to determine a process for decoupling the position and velocity boundary conditions. This can be accomplished by specifying a velocity boundary condition and enforcing a constant position or orientation boundary condition.

Figure 3.2, below, demonstrates the separation of the velocity and position boundary conditions for independent investigation of rate and position. In this case, the top image represents an airfoil pitching at an angle of attack. The bottom images are the decoupled components, the left one representing the angle of attack effects, while the right image represents the velocity profile on the airfoil due to the rotation. The top figure is equivalent to the sum of the two lower figures.

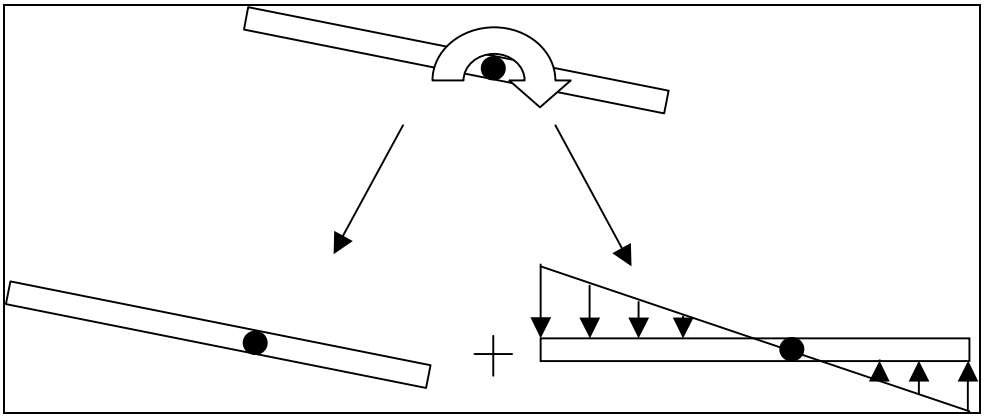

Figure 3.2: Decoupling Position and Velocity Boundary Conditions

Since the effects of position and velocity may now be calculated separately, the excitation is also simplified. The rate effects no longer need to be comparable to the position effects for accurate parameter identification. Furthermore, the frequency content of the excitation signal is only to ensure the same frequency content in the ARMA model. If the model is not needed, then neither is the frequency content of the signal. With displacement held constant for a given rate, the quasi-steady rate effects can be determined without the displacements reaching the nonlinear range, thereby eliminating this consideration from the excitation signal. An additional benefit to removing the need for a model is that the solver does not need to be time accurate. Thus, a faster steady-state solver can be implemented to determine the quasi-steady forces.

Understandably, Euler3d was not designed to implement a steady-state solver in a non-inertial reference frame; as such, the velocity boundary conditions are instead applied through transpiration for use with the steady-state solver. In order to remove the assumptions associated with transpiration to gain a more general solution, the first order time accurate solver of Euler3d can be used with the non-inertial velocity boundary condition specification. While slower than the steady-state solver, this is faster than the second order solver, and since the solution does not need to be time accurate, fewer iterations are required per time step. The number of time steps is then determined by the level of convergence of the solution, not the size of the ARMA model. By separating the excitation of position and velocity, the process of estimating stability derivatives is dramatically simplified.

3.2.1 Deriving Equations

Because the independent specification of velocity and position is not physically consistent, the derivation of the boundary condition equations must be revisited. Consistent boundary conditions are an inherit assumption in the derivation of both the non-inertial formulation of the boundary conditions in Euler3d and in Theodorsen's results for a pitching and plunging airfoil used later in a validation test case. Neither thin airfoil theory, which is also use in the validation test case, nor the transpiration boundary condition equation in Euler3d make the consistency assumption. Understanding the development of these equations is as important as knowing how to use them.

Since thin airfoil theory does not make the consistent boundary condition assumption, the development and presentation of the lift and moment equations are left to Appendix A. Likewise, the transpiration boundary condition equations do not require

any modification for a decoupled boundary condition specification, and as such, the equations are not redeveloped here. Instead, the focus is place on examining the effects the consistent boundary condition assumption has on both the non-inertial boundary condition equation in Euler3d and Theodorsen's equation.

3.2.2 Non-Inertial Boundary Condition Equation

The development of the non-inertial compressible Euler equations implemented in STARS is nicely presented in Cowan's dissertation [2003]; here the focus is place on the alterations of these equations to account for the decoupled boundary conditions. The decoupled boundary condition affects only one equation in Cowan's derivation; the acceleration expressed in the non-inertial frame. Neither the position equation nor the velocity equation relies on a physically consistent specification of position and velocity; the user specifies the non-inertial velocities. However, the acceleration equation does require that the time rate of change of position always equals the velocity. The non-inertial formulation of the velocity as presented by Cowan is expressed below, where B is the transformation matrix, Ω is the angular velocity matrix, and *r* is the radius vector:

$$V_t = V_0 + B\Omega r_{xyz}$$

In order to determine the non-inertial acceleration, the derivative of the above equation proceeds as follows:

$$a_t = a_0 + B\Omega^2 r_{xyz} + B\dot{\Omega} r_{xyz} + B\Omega \dot{r}_{xyz}$$

Normally, the $\dot{r}$ term is set equal to the relative velocity V_r; however, with the decoupled specification, the $\dot{r}$ term is zero. Therefore, by changing the transformed acceleration equation in Euler3d to reflect the non-physical conditions, the non-inertial capabilities of

STARS will now properly calculate the forces and moments due to a decoupled rate specification.

3.2.3 Theodorsen's Moment Equation

The following derivation is only used in comparing Theodorsen's quasi-steady results to the stability derivative estimates predicted by Euler3d for the airfoil test case. Theodorsen's moment equation is broken into two components: non-circulatory and circulatory, the first referring to the body's motion and the latter to the wake effects. Each component of the moment equation is examined separately and the results are combined in the final steps to produce Theodorsen's results for an decoupled boundary condition. The primary reason for the redevelopment of Theodorsen's function without the consistent boundary condition assumption is that the time rate of change of angle of attack, for instance, is no longer equal to the pitch rate, because α is held constant but the rate, $\dot{\alpha}$, is specified as non-zero. A review of the geometry of Theodorsen's pitching and plunging thin airfoil is presented in Figure 3.3 below, including the notation used in this work, which follows Falk's derivation [2003]. In this section, *b* represents the semi-chord length, *a* represents the faction of *b* to the center of rotation, and *h* is the vertical displacement with the free stream velocity in the positive X direction. The flow is assumed inviscid, irrotational, and incompressible.

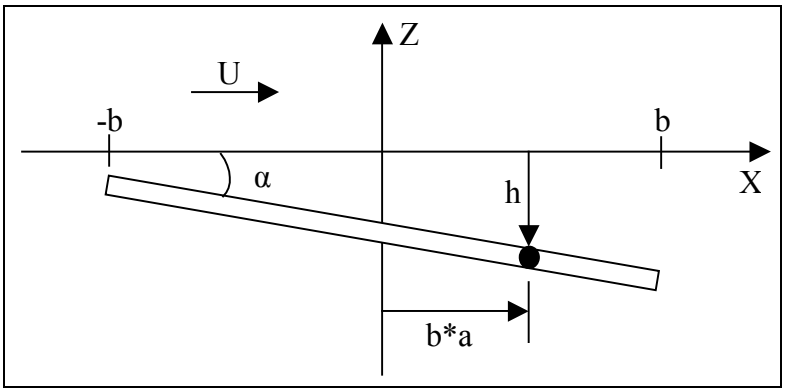

Figure 3.3: Geometry and Notation for Theodorsen's Problem

Following the derivation presented in Falk's notes, the potential field is given by the following equation, where *w* is the downwash on the thin airfoil and θ stems from the standard coordinate transformation:

$$\phi(\theta,t) - \frac{b}{\pi}\int_{\theta}^{\pi}\int_{0}^{\pi}\frac{w\sin\beta^{2}\,d\beta d\theta}{\cos\beta-\cos\theta}$$

The following equation then calculates the pressure difference across the airfoil:

$$\Delta p = -2\rho\cdot\left[\frac{\partial\phi}{\partial t}-\frac{U}{b\cdot\sin\theta}\frac{\partial\phi}{\partial\theta}\right]$$

Using these two equations, results in the following non-circulatory moment equation.

$$M_{ync} = 2Ub\rho\int_{0}^{\pi}\phi\sin\theta d\theta - 2b^{2}\rho\frac{\partial}{\partial t}\int_{0}^{\pi}\phi(\cos\theta-a)\sin\theta d\theta$$

The equation for the potential function then follows when the downwash is described by the following equations.

$$w(\beta,t) = -\dot{h}-U\alpha-\dot{\alpha}b(\cos\beta-a)$$

$$\phi(\theta,t) = b(\dot{h}+U\alpha)\sin\theta+b^{2}\dot{\alpha}\sin\theta\left(\frac{1}{2}\cos\theta-a\right)$$

All of the above are the standard equations in the development of Theodorsen's equations; however, with a decoupled boundary condition specification, the final potential equation is no longer a function of time. Since both position and rate terms are held constant in time, the derivative of the potential with respect to time is now equal to zero in the pressure and moment equations. This produces the following equation for the non-circulator moment:

$$M_{ync} = \pi U b^2 \rho\left[\left(\dot{h} + U\alpha\right) - \dot{\alpha} b a\right]$$

With a consistent boundary condition specification, the derivative of potential with respect to time yields acceleration terms and the α term becomes an $\dot{\alpha}$ term in the second integral of the moment equation. The $\dot{\alpha}$ term in the first integral cancels with the $\dot{\alpha}$ generated by the derivative of potential in the second integral, hence Theodorsen's original equation for the non-circulator moment did not contain the $\dot{\alpha}$ term.

For the circulatory portion of the moment equation, the derivation never assumes that the derivative of α is equal to $\dot{\alpha}$; instead, the potential function is related to the vorticity distribution in the wake, which is a function of the downwash on the airfoil. Therefore, the decoupled boundary condition does not affect the circulatory component of the moment equation. Setting the reduced frequency, *k*, equal to zero in the Theodorsen function is the only requirement to determining the circulatory component of the quasi-steady moment. With a reduced frequency of zero, Theodorsen's function becomes unity, yielding the following equation for the circulatory quasi-steady moment:

$$M_{yc} = 2\pi\rho U b^2 a \cdot \left[\dot{h} + U\alpha + b\dot{\alpha} \cdot \left(\frac{1}{2} - a\right)\right]$$

Combining the circulatory and non-circulatory components of the pitch moment equations yields the following equation, after some algebraic simplification:

$$M_y = \pi U b^2 \rho \cdot \left[\left(\dot{h} + U\alpha \right) \cdot \left(1 + 2a \right) - 2a^2 b\dot{\alpha} \right]$$

Note that the moment about the quarter-chord, a = -0.5, does not change with α, in other words, the aerodynamic center is at the quarter-chord. Also, note that the moment is zero about the mid-chord, a = 0, if only a pitch rate is applied. This corresponds to data presented in *Theory of Wing Sections* for a symmetrically cambered airfoil, which is equivalent to an airfoil pitched about its mid-chord. For the current work, the stability derivative, C_{mq}, is more relevant than the total moment, so the above equation is reformulated into the following equation, using l/c as the non-dimensional pitch location, positive aft of the leading edge and negative fore of the leading edge:

$$C_{mq} = -4\pi \cdot \left(\frac{l}{c} - \frac{1}{2} \right)^2$$

The above expression from Theodorsen's equation, with velocity and position decoupled, can now be correctly compared to the results obtained by the modified Euler3d flow solver for a simple airfoil test case. After this, the modified CFD routine will be used to calculate the stability derivatives of more complex geometries that Theodorsen's cannot predict.

CHAPTER 4

RESULTS AND DISCUSSION

4.1 Forced Oscillation Parameter Identification

The following sections apply the forced oscillation technique in the computational framework of STARS to two cases and present the results in comparison to theoretical values. The first test case is presented in conjunction with discussions of grid refinement, excitation signal parameter selection, model order determination, and interpretation of results. The following cases will present less on the process and focus instead on the results of the process. Once the results of the forcing method have been presented, the decoupled boundary condition specification method will be initially validated with Theodorsen's results. Upon validation of the decoupled method, the first two cases will be re-evaluated with this new method in order to investigate the relative accuracies of both processes. Finally, stability derivative estimates for more complex test cases obtained by the decoupled boundary condition analysis will be presented to demonstrate the effectiveness of this method.

4.1.1 Horizontal Tail

This single degree of freedom test case is based on an example from Nelson's text [1998], with some modifications. Instead of a flat plate pivoting 10.998 inches fore of the leading edge, a NACA 0012 cross-section with a span of 12in and a chord of 2.004in is used. The airfoil shape removes some of the sharp corners and allows for a smoother

airflow around the surface. In addition, the free stream velocity is increased to Ma .5 at sea level conditions. The results from STARS will be compared with the theoretical results from Nelson's method, corrected for compressibility. Figure 4.1 shows the geometry for this case with the axis located at the pivot point. The far-field boundary has been omitted, but is a sphere centered at the leading edge of the wing with a radius of 25in.

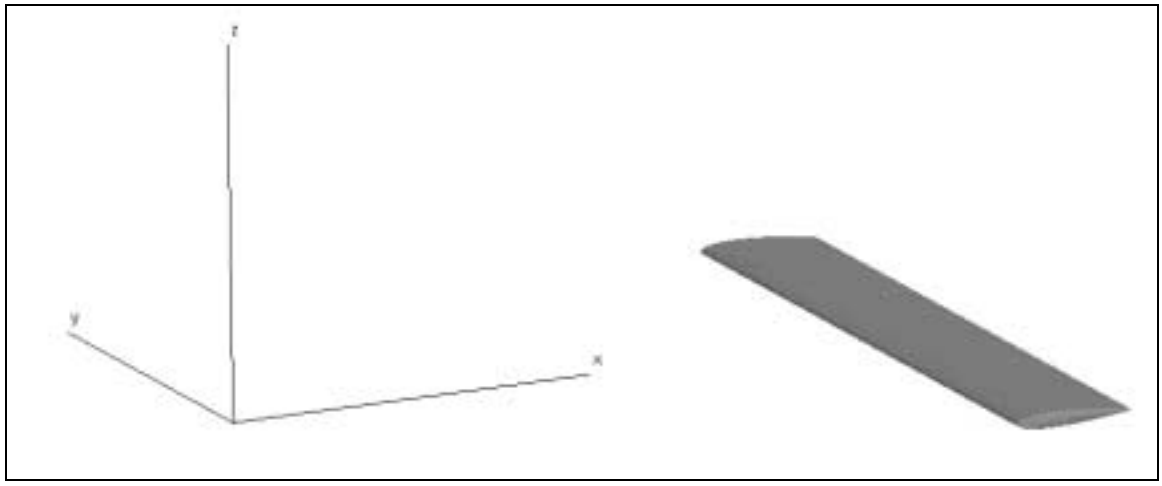

Figure 4.1: Geometry and Axis of Rotation for Horizontal Tail

The grid for this case was refined in two iterations using a routine called Remesh3d. This program calculates the second derivative of a flow property, such as Ma or pressure, at each node, then scales the spacing at every node according to the ratio of the second derivative to the maximum second derivative and the minimum desired grid spacing. Refining the grid in this manner is preferable to a general grid refinement at every location. By adding elements only where they are needed, such as in areas of high gradients, the grid is improved without increasing the computational cost with superfluous nodes. Since theoretical results for $C_{m\alpha}$ was available, the grid was deemed converged when the pitch moment coefficient determined by STARS aligned with theory. Similarly, if theoretical values were unavailable, another iteration would indicate a

sufficient level of convergence. The final steady state grid iteration, 2-STARS, matches the analytical results within 1.60% for $C_{m\alpha}$. This convergence can be seen in Figure 4.2, below.

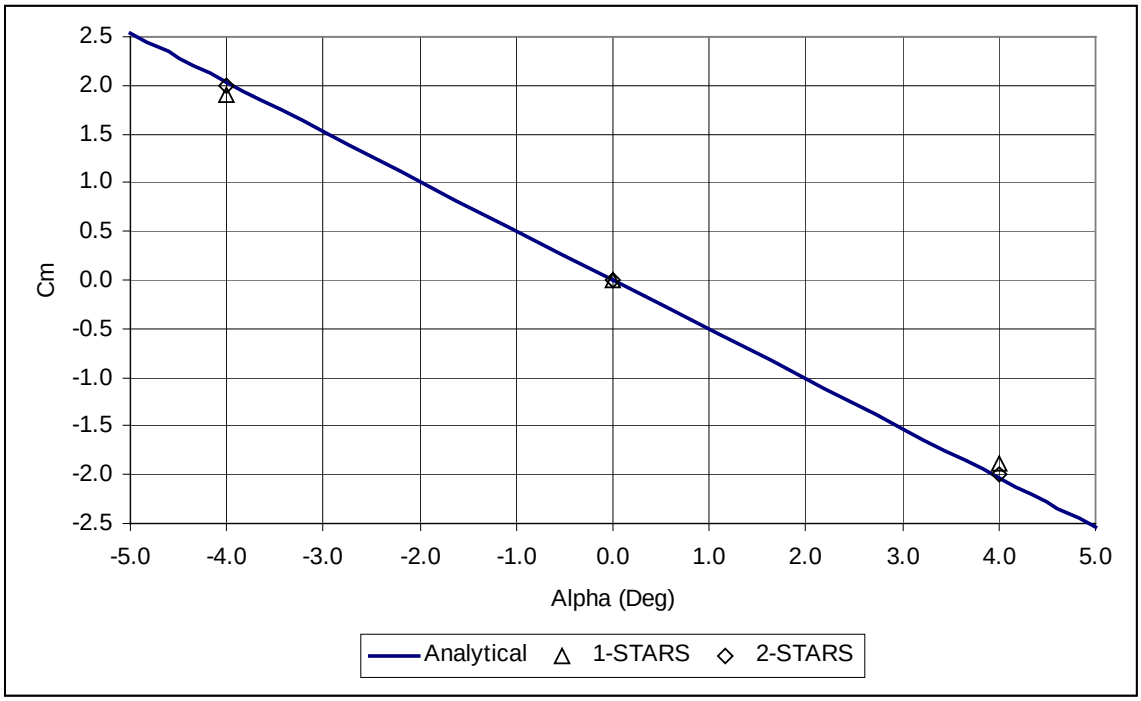

Figure 4.2: Grid Convergence Based on Moment Coefficient

Unfortunately, this grid provides no information on the wake element spacing. Since the moment is at steady state, the Remesh3d routine increases the spacing in the wake region to the detriment of a time-accurate solution. To correct this situation, wake elements were added from the trailing edged to the far field after running Remesh3d. Additional elements were also added in the wing tip and the leading edge regions. The final grid contained 455,000 elements in the computational domain, but only the surface elements can be seen in Figure 4.3. With the surface and grid generated, the process of estimating stability derivatives begins.

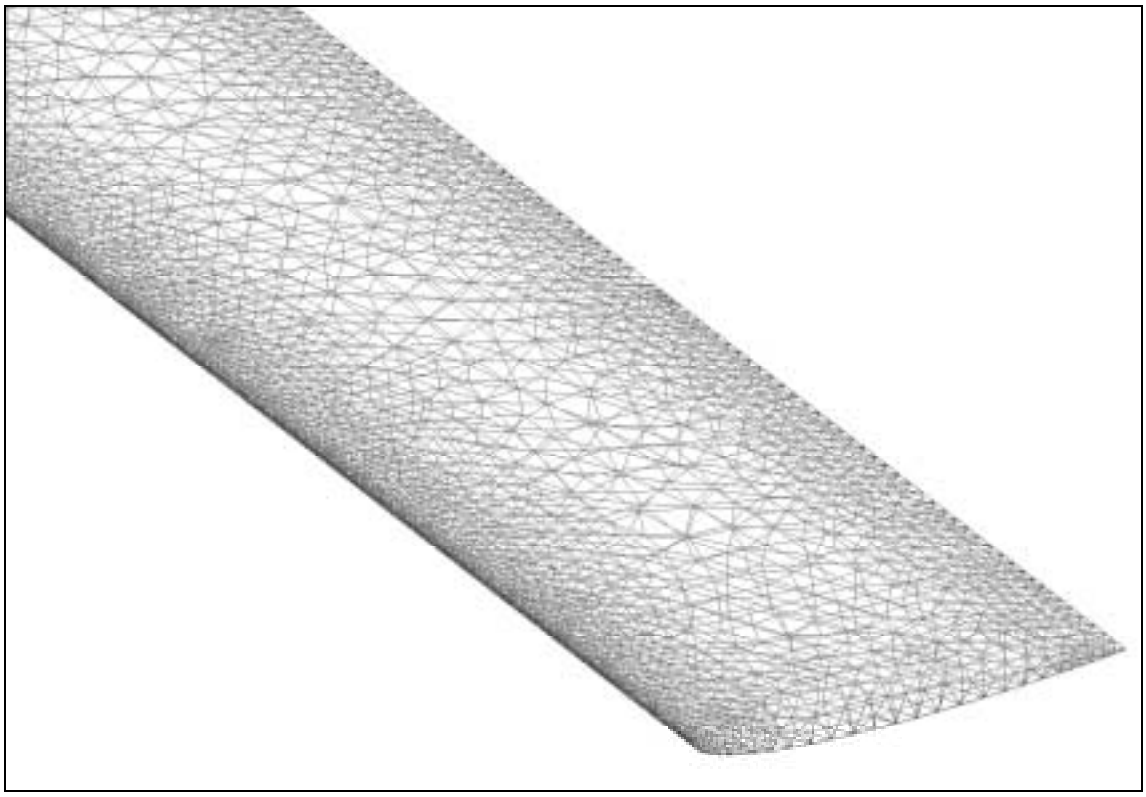

Figure 4.3: Close-up of Surface Grid for Horizontal Tail

Following the procedure outlined in the Methodology Section, the first step in estimating stability derivatives is to determine the parameters of the excitation signal. For this test case, the motion is constrained to pitch only about the y-axis in Figure 4.1; as such, the excitation signal excites pitch angle and pitch rate. In order to stay within the linear lift region and avoid stall, the maximum angle of attack is set to 4deg. The pitch rate required to yield a comparable effect in the pitch moment is given by the following equation for small angles and large *l*, the distance from quarter-chord to center of rotation.

$$\alpha = \frac{q \cdot l}{U}$$

Given the geometry and free stream velocity for this case, the maximum pitch rate should be 2232deg/sec. After plotting the dc-chirp signal with these parameters and the

time step as a function of the minimum number of points at the highest frequency, the best value of *minpt* was determined to be 35. Higher numbers reduced the frequency content without adding significant definition to the signal, while lower numbers produced a sampling rate that was too small at the highest frequency.

The maximum time step can now be calculated as 5.12e-5sec, which is rounded down to 5.0e-5sec. With the time step now determined, the number of data points required for parameter identification can be found. If the wake's effect becomes negligible 8-chords aft of the trailing edge, then 50 time steps are required to reach this point. The overdetermination of the mathematical model depends on the size of the model; however, if *over* is specified to be 8, then the largest model has an overdetermination factor of 8 and the smaller models will have a larger overdetermination factor. This yields a requirement of 800 points for the parameter identification. With this, all the terms of the excitation signal can be calculated in their dimensionless form. The *displ* term is the maximum angle of attack in radians, while V_{max} in the ω equation is given by the following equation, where q is the maximum pitch rate in rad/sec and *refdim* is specified in the control file, typically as 1:

$$V_{\max} = \frac{q \cdot ref\ \dim}{U}$$

This combination of parameters results in the excitation of the angle of attack and the pitch rate seen in Figure 4.4, below. While the pitch rate, *q*, may seem too large, this value is necessary in order for the parameter identification routine to properly identify the effects of both position and velocity. Smaller values of *q* will corrupt the estimation of its effects on the moment, essentially drowning the effect of pitch rate in the effect of pitch angle. However, an extremely large pitch rate could excite terms that would not

appear under normal operating conditions, and could produce effects that could not be correctly eliminated through the ARMA model, such a shock waves due to motion not flight condition.

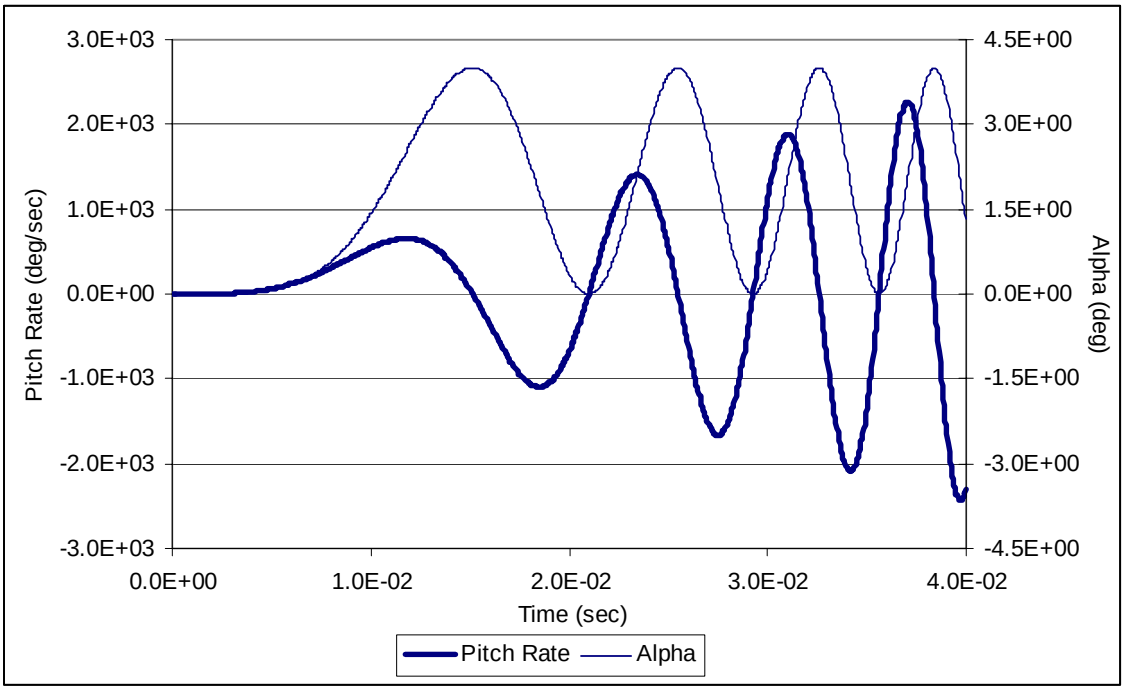

Figure 4.4: Pitch Rate and Angle of Attack (Alpha) for DC-Chirp

Figure 4.5 presents the control file implemented with the horizontal tail test case. STARS ran for 24.56 hours to generate the 800 data points, with 50 iterations per time step to insure convergence at each time step. By combining the load and dynamics files, as discussed in the Methodology Section, the data can be compiled into the proper form for the SVD routine.

```
&control
    dt       = 0.3348d0,          mach     = 0.50d0,
    gamma    = 1.40d0,            alpha    = 0.0d0,
    diss     = 1.00d0,            beta     = 0.0d0,
    cfl      = 0.5d0,             refdim   = 1.0d0,

    nstp     = 800,               istrt    = .true.,
    nout     = 800,               iaero    = .true.,
    ncyc     = 50,                idynm    = .true.,
    isol     = 2,                 ielast   = .false.,
    idiss    = 1,                 ifree    = .true.,
    ipnt     = 1,                 iforce   = .false.,

    omega    = 3.5057d-4,         nr       = 1,
    ratio    = 700                ainf     = 1.3392d4,
    displ    = 6.981317d-2,       rhoinf   = 1.146d-7,
```

Figure 4.5: Control File Parameters for Horizontal Tail

After generating a range of models for na, 1 to 50, and nb, 3 to 50, each model was given inputs from the excitation signal; and, the error between the model and the STARS data was tabulated. The best na-nb model according to the RMS error between the signal and data was a 29-49, whereas the 35-14 model had the lowest RMS of the cross correlation. Since the ARMA model can oscillate about the actual STARS output and produce a small RMS, the only true way to determine the quality of the model is to plot the model's output with the STARS data. The pitch moment coefficient time histories of the two ARMA models are extremely similar; both models match the STARS output quite well, as seen in Figure 4.6. Although the ARMA line is based on the 35-14 model, the graph can represent both the 29-49 model and the 35-14 model, since the differences are essentially imperceptible.

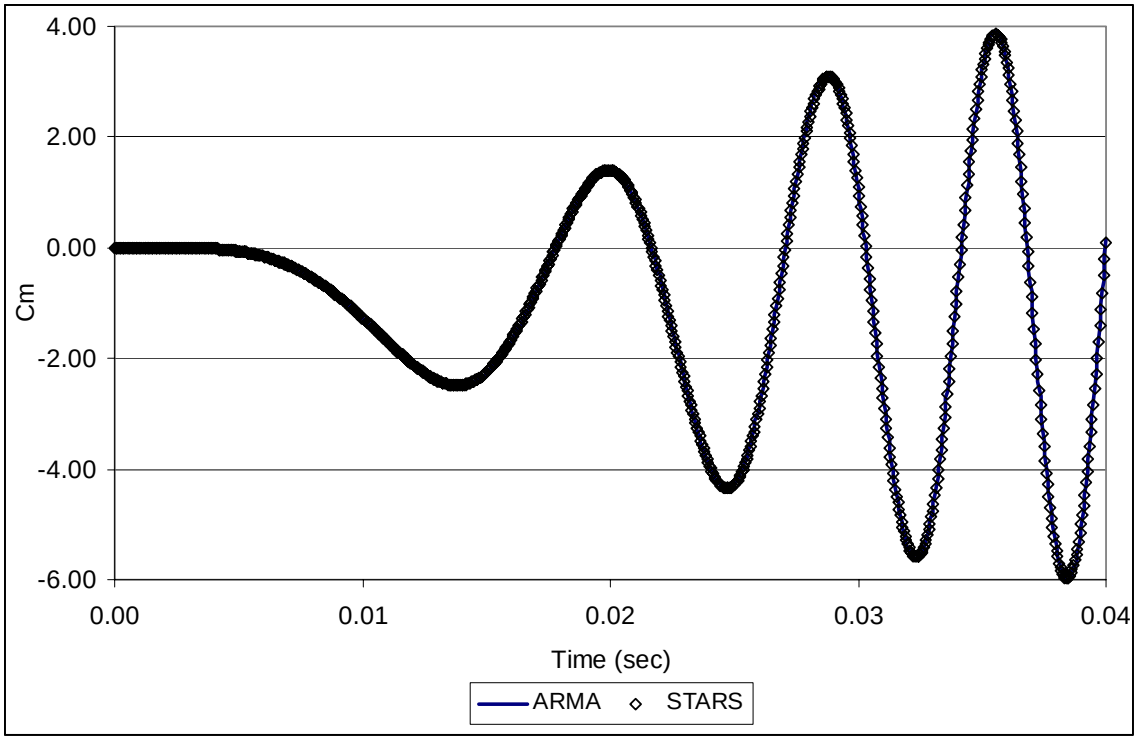

Figure 4.6: Comparison of C_m for ARMA Model and STARS

Through the process outlined in the Methodology Section, the stability derivative can be extracted from the ARMA model coefficients. Figure 4.7 below contains the spreadsheet data used to extract the stability derivatives for the 35-14 ARMA model. The A's are the previous force coefficients, the B's are the current and previous position coefficients, and the inputs are the dimensionless time step and the theoretical values for percent difference calculations.

Input	
dt*	0.3348
Cmalpha	-2.9100E+01
Cmq	-3.4850E+02

Output	
Cmalpha	Cmq
-2.852E+01	-3.484E+02
-1.9780%	-0.0162%

Sum(B's)	Sum(A*j)	Sum(B*(j-1))	1-Sum(A's)	(1-Sum(A's))^2
-3.92085E-01	5.32995E-03	2.16612E+01	2.85229E-04	8.13555E-08

A's	B's	j	A*j	B*(j-1)
3.9158582E+00	2.1270306E+04	1	3.9158582E+00	0.0000000E+00
-6.0783746E+00	-4.3510418E+04	2	-1.2156749E+01	-4.3510418E+04
4.5180339E+00	1.4716748E+04	3	1.3554102E+01	2.9433496E+04
-1.2235178E+00	-1.2182433E+03	4	-4.8940712E+00	-3.6547300E+03
-4.4795634E-01	-8.2015002E+03	5	-2.2397817E+00	-3.2806001E+04
2.5505407E-01	3.9455524E+04	6	1.5303244E+00	1.9727762E+05
3.1928360E-01	-5.0838306E+03	7	2.2349852E+00	-3.0502984E+04
-3.5412394E-01	2.1656047E+04	8	-2.8329915E+00	1.5159233E+05
-1.0718900E-01	-5.0834416E+04	9	-9.6470102E-01	-4.0667533E+05
4.3597790E-01	-1.7815644E+04	10	4.3597790E+00	-1.6034079E+05
-1.2707976E-01	1.9454999E+04	11	-1.3978774E+00	1.9454999E+05
-5.5909591E-01	-1.3731269E+04	12	-6.7091509E+00	-1.5104396E+05
8.9276947E-01	5.4234526E+04	13	1.1606003E+01	6.5081431E+05
-6.2806095E-01	-3.0393220E+04	14	-8.7928534E+00	-3.9511186E+05
2.7803843E-01		15	4.1705765E+00	0.0000000E+00
-1.9799604E-01		16	-3.1679367E+00	0.0000000E+00
1.2045208E-01		17	2.0476853E+00	0.0000000E+00
-3.1384154E-02		18	-5.6491478E-01	0.0000000E+00
1.8937286E-01		19	3.5980844E+00	0.0000000E+00
-2.2424657E-01		20	-4.4849314E+00	0.0000000E+00
-3.0910703E-01		21	-6.4912476E+00	0.0000000E+00
8.0676274E-01		22	1.7748780E+01	0.0000000E+00
-5.3162020E-01		23	-1.2227265E+01	0.0000000E+00
1.1126588E-01		24	2.6703811E+00	0.0000000E+00
-2.2569922E-01		25	-5.6424805E+00	0.0000000E+00
4.1113520E-01		26	1.0689515E+01	0.0000000E+00
-4.2391787E-01		27	-1.1445782E+01	0.0000000E+00
2.0448730E-01		28	5.7256443E+00	0.0000000E+00
4.0537209E-01		29	1.1755791E+01	0.0000000E+00
-7.0657333E-01		30	-2.1197200E+01	0.0000000E+00
3.8411769E-01		31	1.1907648E+01	0.0000000E+00
1.3207324E-02		32	4.2263436E-01	0.0000000E+00
-3.1828114E-01		33	-1.0503278E+01	0.0000000E+00
3.6549423E-01		34	1.2426804E+01	0.0000000E+00
-1.3274440E-01		35	-4.6460542E+00	0.0000000E+00

Figure 4.7: Extraction of Stability Derivatives from the 35-14 ARMA Model

The extracted stability derivatives are very close to the theoretical values for the 35-14 ARMA model. The stability derivative extracted from the 29-49 model should be

accurate as well, due to the similarities in the output of the two models. The percent difference and the extracted stability derivatives are listed in Figure 4.8, below.

Output	
Cmalpha	Cmq
-2.869E+01	-3.174E+02
-1.4076%	-8.9222%

Figure 4.8: Stability Derivatives Extracted from the 29-49 ARMA Model

While the percent difference in $C_{m\alpha}$ stayed relatively the same, the pitch damping percent difference increase noticeably, but remained below 10%. If, when no theoretical value is available, two different ARMA models match the STARS data equally well and the estimated coefficients are similar, an averaged value of the coefficients from each model may better approximate the real value of the stability derivative, as seen in Figure 4.9. The different values can also provide an estimation of the uncertainty in the extracted values. Alternatively, as previously discussed, the models can be generated with one excitation signal and the best model is then determined by its ability to predict the response due to a different signal with the same time step. Although this can be a time consuming step, in the absence of theoretical results, generating data with a new signal is the best way to confirm the prediction capabilities of the ARMA model and increase confidence in the estimated derivatives.

Output	
Cmalpha	Cmq
-2.861E+01	-3.329E+02
-1.6928%	-4.4692%

Figure 4.9: Average Values of Stability Derivatives from Both Models

Given that the theoretical values are available, the analytical quasi-steady pitch moment time history can be created and compared with the quasi-steady values predicted by the ARMA model. Figure 4.10 reveals how accurately the 35-14 ARMA model matches the analytical response. This may initially appear to be a redundant figure in that the ARMA model agrees with the STARS data; however, the data used to generate the model is much different than the quasi-steady response predicted by the analytical results.

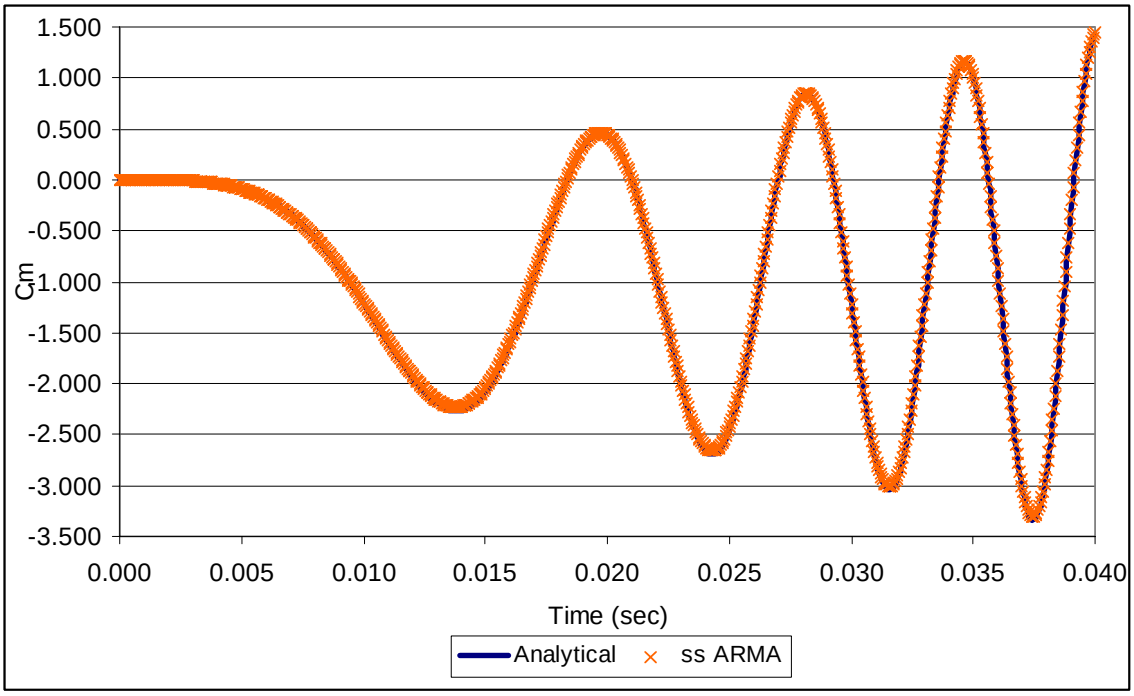

Figure 4.10: Comparison of C_m for Analytical and Quasi-Steady ARMA

Since large excitations violate the assumptions of stability derivative analysis, the ARMA model is used to transition from the unsteady data to the quasi-steady stability derivatives. After the ARMA model is fit to the fully unsteady data produced by STARS, the ARMA model is given quasi-steady conditions to remove the unsteady terms and extract the quasi-steady stability derivatives. The purpose of the ARMA model is to correctly account for the unsteadiness produced during excitation in order to properly eliminate it from the stability derivative calculations. Figure 4.11 demonstrates the

unsteady "filtering" that the ARMA model provides. The difference, both in phase and amplitude, between the analytical and the STARS data results from unsteady and higher order terms not included in the analytical model; however, the ARMA model can be used to translate the unsteady STARS data into the quasi-steady analytical results. The unsteady terms are neither Gaussian nor white as is assumed during the filtering of experimental data. Also, the large magnitude of the unsteady effects is due to the extremely large rate excitation required for the proper identification of the rate effects. Essentially, in order to accurately estimate the quasi-steady rate term, the unsteady terms must also be excited. The 'Analytical' line is covered by the 'ss ARMA' points; similarly, the 'STARS' points obscure the 'ARMA' line.

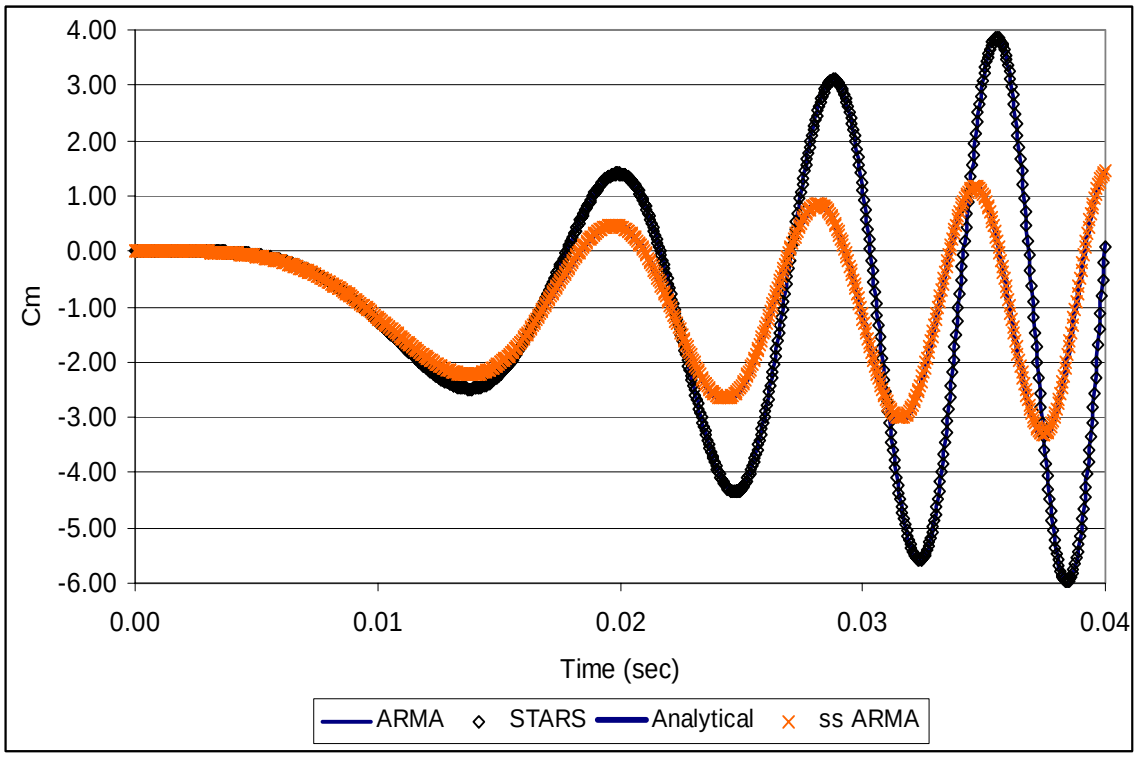

Figure 4.11: Comparison of Unsteady STARS to Quasi-Steady Analytical Results

4.1.2 Dihedral Wing

The next case to be examined is a dihedral wing, allowing for both longitudinal and lateral stability derivative analysis. Figure 4.12 presents the geometry of this test case with a chord of 2 inches, a span of 8 inches, a NACA 0009 cross-section, and 5 degrees of dihedral. The axis is on the origin of rotation, which is located at the centerline leading edge, 0.5 inches above the plane of the root chord. Flight conditions are specified as standard sea level at Mach 0.4. Wake elements are included in the ellipsoidal computational domain in order to capture the transients in the flow field that result from the excitation of the wing.

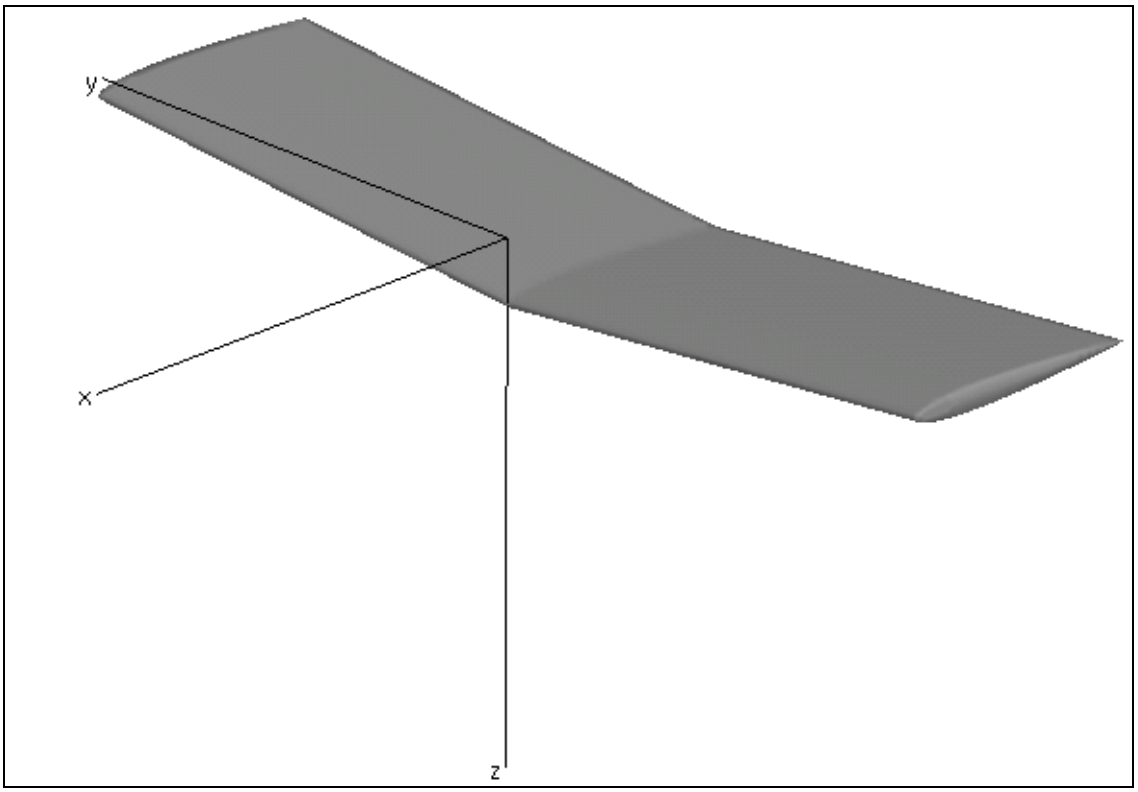

Figure 4.12: Geometry of Dihedral Wing

A grid resolution study was conducted, as before, implementing the Remesh3d procedure; however, with this case, the effects of sideslip angle, β, had to be examined as well. For angle of attack, the steady state solution was determined at -5, 0, and 5 degrees α for each grid refinement iteration. The results of this grid convergence can be seen in Figure 4.13, below. From this figure, the initial grid would have been sufficient to capture longitudinal effects, but grid refinement for the lateral direction can affect the longitudinal results, although it does not in this case. Therefore, the pitch moment plot was created to ensure that the lateral refinement did not adversely affect the longitudinal results. Roll angle was not investigated since, at zero α, all roll angles are equivalent.

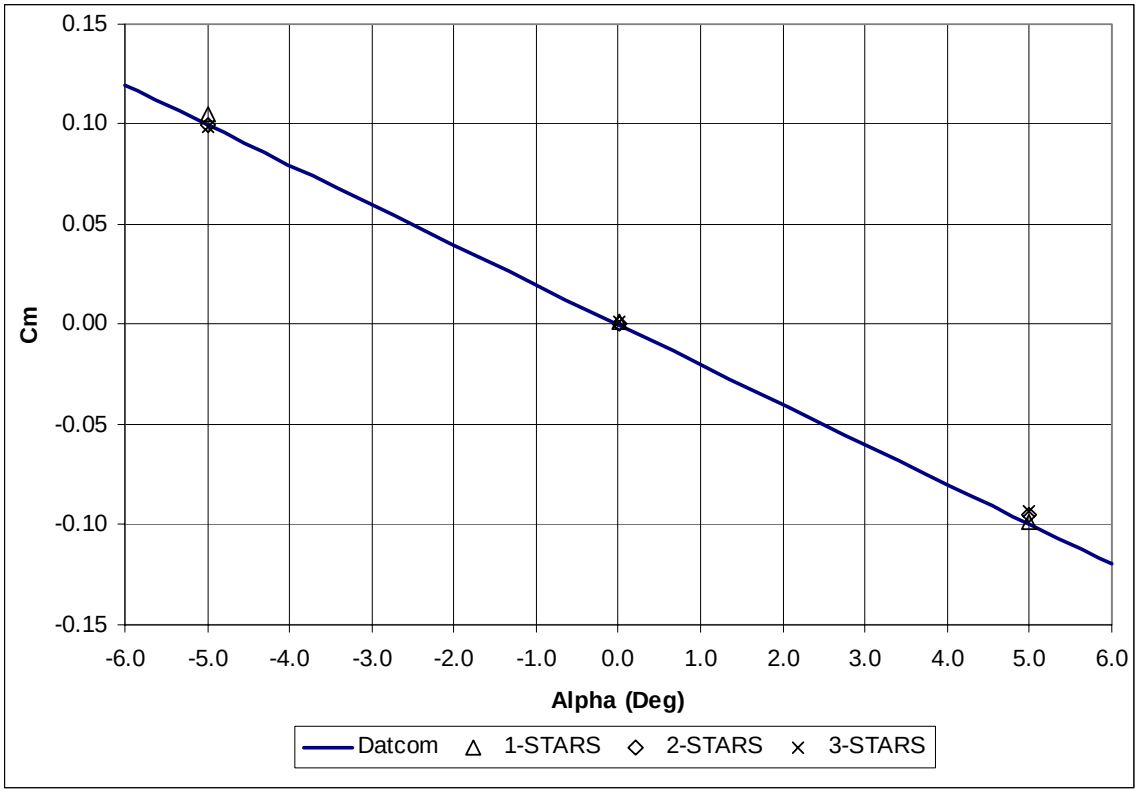

Figure 4.13: Longitudinal Grid Convergence

As stated above, grid convergence based on lateral effects was also investigated. At zero degrees angle of attack, the system was given -5, 0, and 5 degrees β in order to determine the capability of the grid to accurately capture sideslip. Using the Remesh3d program to again generate more elements in areas of high gradients, the grid was converged as seen in Figure 4.14 below according to the roll moment induced by the sideslip angle. While the values do not lie directly on the analytical line obtained from the Datcom equations, the grid was refined until the results were independent. The Datcom method is somewhat empirical, and the effect of roll moment due to sideslip is small. For this geometry, both of these factors contribute to the less than perfect alignment between the converged grid and the analytical line. In the absence of analytical results, Figure 4.14 indicates a converged grid, which should be sufficient for a method independent of previous estimates.

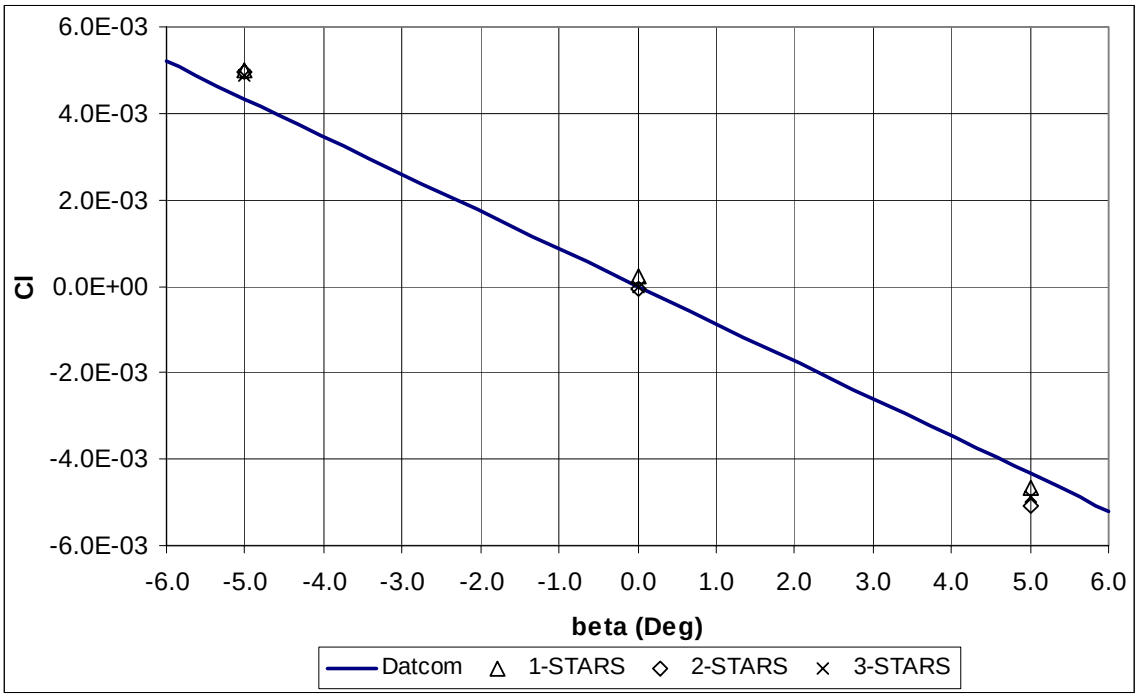

Figure 4.14: Lateral Grid Convergence

By following the same procedure as before, the control parameters for pitch excitation seen in Figure 4.15 are produced. The excitation parameters translate to a maximum angle of attack of 6 degrees and a maximum pitch rate of 32,250 degrees per second. This is an extremely large value of q; however, it is the amount of q needed for the proper identification of pitch damping. This value for q generates an equivalent angle of attack of 3 degrees at the quarter-chord and 6 degrees at the half-chord. With a comparable angle, the large rate has a comparable effect, which can be identified by the ARMA model. Such a large value also indicates that the effect of C_{mq} will be small; however, it is still the dominant pitch damping term [Datcom 1978] and, therefore, requires accurate estimation.

```
&control
dt     = 8.0352d-2,        mach   = 0.40d,
gamma  = 1.40d0,           alpha  = 0.0d0,
diss   = 1.00d0,           beta   = 0.0d0,
cfl    = 0.5d0,            refdim = 1.0d0,

nstp   = 4000,             istrt  = .true.,
nout   = 4000,             iaero  = .false.,
ncyc   = 75,               idynm  = .true.,
isol   = 2,                ielast = .false.,
idiss  = 1,                ifree  = .true.,
ipnt   = 1,                iforce = .false.,

ratio  = 800d0             nr     = 1,
omega  = 3.2019d-3         ainf   = 1.3392d4,
displ  = 1.0472d-1         rhoinf = 1.146d-7,
```

Figure 4.15: Control File for Pitch Excitation

With such a small time step, the ARMA model would need about 250 terms in order to account for wake effects 10 chord lengths downstream. Determining the model parameters for a model of this size would be a rather large and time consuming undertaking; instead, the data was re-sampled. By taking every fifth point, the time step for the ARMA model, not the flow solver, increases by a factor of five and the number of

terms in the ARMA model reduces by a factor of five. An ARMA model of 50 terms is much easier to identify. While the flow solver requires a smaller time step in order to ensure convergence at each step, the ARMA model time step can be larger, so long as it stays sufficiently above the Nyquist frequency.

The same process was repeated for sideslip and for roll rate effects, but not for roll angle. Likewise, a plunging velocity and a side velocity were also excited in order to separate the effects of $\dot{\alpha}$ from pitch rate and $\dot{\beta}$ effects from yaw rate as discussed in the Methodology Section. However, the failure of this method to accurately predict the longitudinal effects precludes any discussion of the lateral direction and velocity excitations.

Exciting the pitching motion according to the parameters listed in Figure 4.15 and re-sampling the data, as discussed above, produces the pitch moment coefficient time history response seen in Figure 4.16. This figure is very different from the plot presented for the horizontal tail because the unsteady effects are magnified tenfold for this case. Since the excitation is a factor of ten larger, the unsteady effects are equivalent in magnitude as the steady and quasi-steady stability derivatives, causing a great deal of both constructive and destructive effects. Also included in the figure is a line representing the ARMA model which best fit the data according to the RMS of the correlation error. While this model does an extremely poor job of matching the STARS data, the 7-5 model did better than any of the other models examined in the na 1 to 40, nb 2-50 sweep. Due to the poor performance of the 7-5 ARMA model to predict the data used to train the model, there is little hope of achieving accurate stability derivatives.

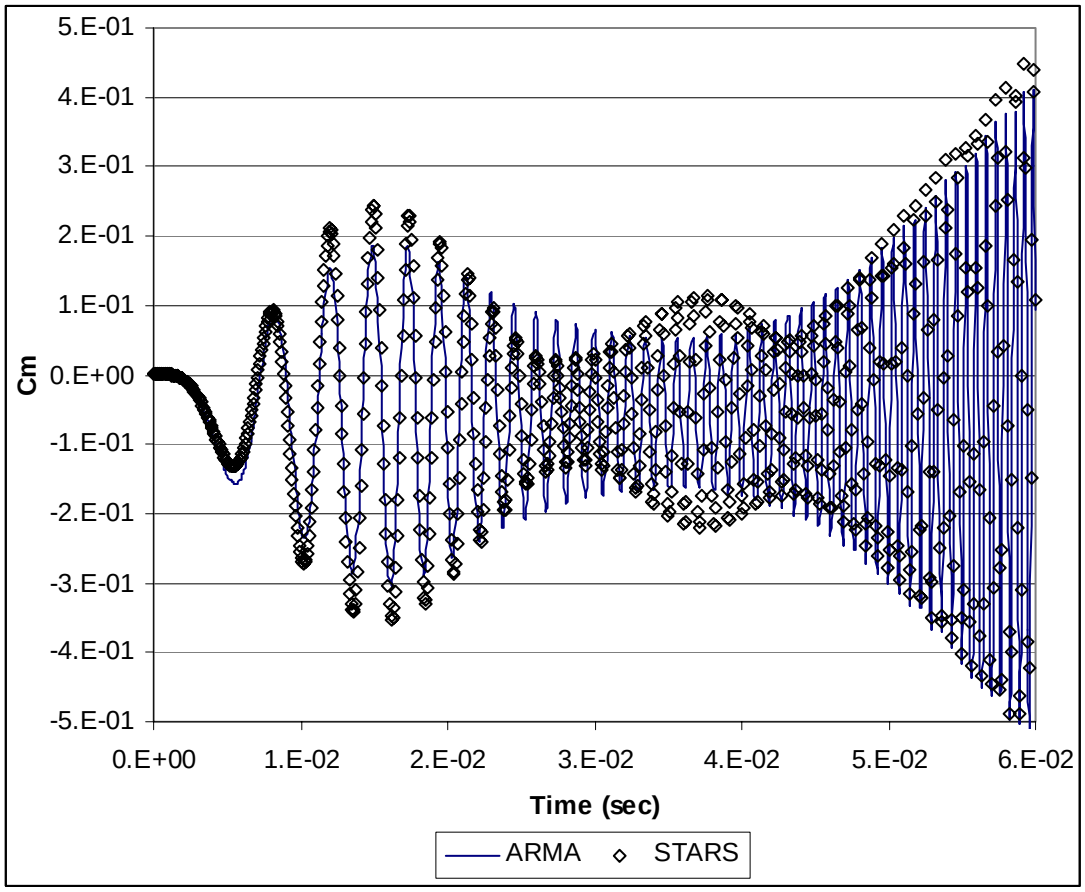

Figure 4.16: Resampled Pitch Moment Coefficient Time History with ARMA Model

As expected, the error in the stability derivatives is high. For $C_{m\alpha}$, the percent difference between the thin airfoil theory estimate, corrected for compressibility and aspect ratio, and the STARS prediction is almost 40%; the percent difference of C_{mq} is a staggering 140%. Figure 4.17 attempts to compare the analytical response predicted by thin airfoil theory and small disturbance theory to the response obtained through the ARMA model coefficients. The large error in C_{mq} can be seen by the large difference on the right side of the figure where q is largest and the response predicted by the stability derivatives extracted from the ARMA model extend off the chart.

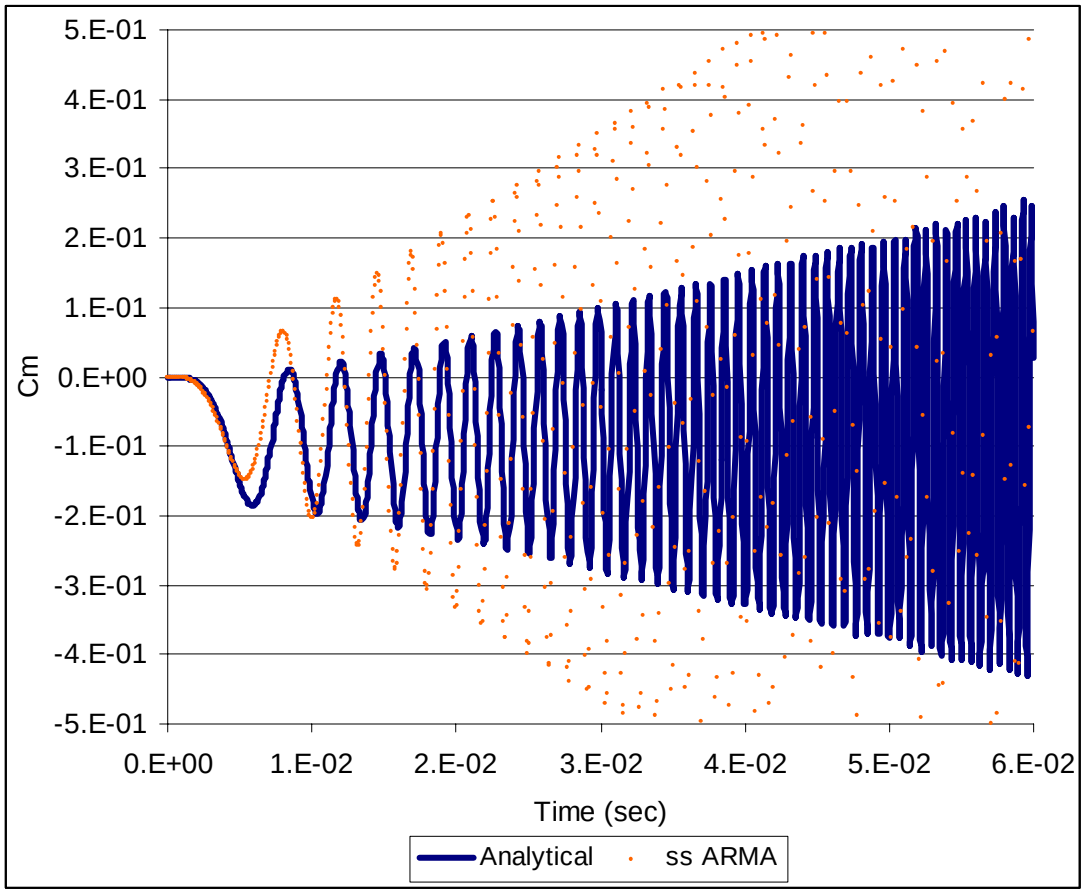

Figure 4.17: Comparison of C_m for Analytical and Quasi-Steady ARMA

Although the forced oscillation parameter identification method failed for this case, it was highly accurate in predicting the stability derivatives for the horizontal tail. This method cannot identify small magnitude terms well without extreme excitation, which leads to a very small time step and increased unsteadiness. For the identification of dominant terms, this parameter identification routine works quite well. Another drawback to this method is the large amount of time required to generate a time accurate solution over enough time steps to generate identification data. The process of selecting the best model is also an issue of concern. Without theoretical values or estimates, the surest way to determine the best model is to run yet another time accurate solution so that the models can predict data not used in the training process. This method could be

helpful in analyzing existing data or in determining the dominant terms affecting the forces on a system. In this implementation, less dominate terms would not be intentionally over excited in order to produce forces comparable to the dominate terms. To achieve the objectives of this work, a more robust and accurate technique was sought to estimate stability derivatives in a timelier manner.

4.2 Decoupled Boundary Condition Specification

The following sections present the estimates of stability derivatives by applying the velocity boundary condition separately from the position boundary condition in STARS. This is accomplished through both modified non-inertial rate specification and transpiration. While transpiration adds some limiting assumptions, the time saved for the more complicated test cases is worth the slight loss of accuracy and amplitude limitations. Unlike the previous method, no extreme excitation signal is required to identify the individual effects; they are excited independently. Since the decoupled boundary condition method is based on quasi-steady forces and moments, no model is required to make the results fit the stability derivative assumptions. As this method greatly simplifies the process of estimating stability derivatives, the results of the following sections focus on comparison with the previous method, as well as with analytical, empirical, and flight-test data for a variety of geometries over a broad range of Mach numbers.

4.2.1 Airfoil

In order to investigate the accuracy of estimating stability derivatives by the separate excitation of velocity and position, a simple, well-developed test case was examined. For this initial case, an NACA 0012 airfoil with a unit chord is first pitched about the leading edge, then about various points fore and aft of the leading edge to estimate C_{mq}. Grid convergence for this test case is not investigated, as this grid has shown itself to be sufficient and well converged in previous works [O'Neill 2003]. The infinite span airfoil is simulated by a symmetry plane on one side of the 0.2inch wide computational domain and a wall boundary on the other side. Inviscid, Euler solvers treat a wall boundary the same as a symmetry plane, since there is not a no-slip condition on the wall boundary. Figure 4.18 presents the geometry for this airfoil test case.

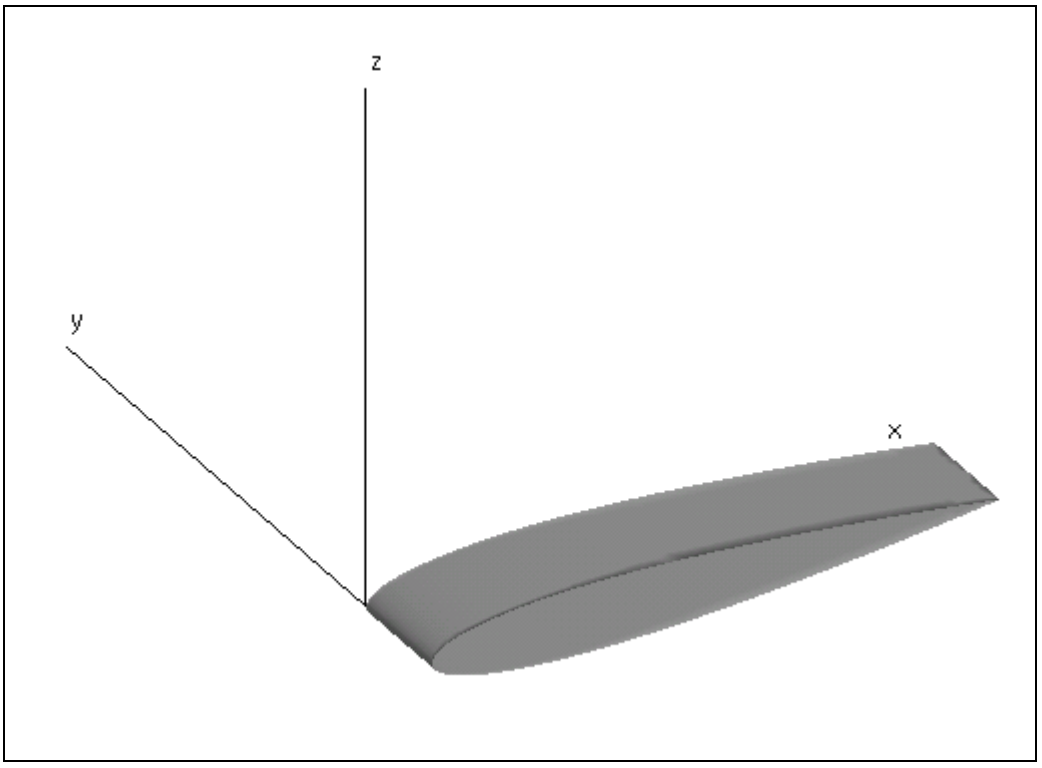

Figure 4.18: Geometry for Airfoil Test Case

The flight condition for this case is standard sea-level conditions at Ma 0.3. The Mach number is intentionally set to a low value for a better comparison of pitch moment results with incompressible theory. If the non-inertial formulation is used with the modifications discussed in the Methodology Section, then the dynamic file is given the origin of the non-inertial frame and the constant pitch rate while holding α constant at zero. If transpiration is used to simulate the motion, then the vector file is generated to model the rigid body pitch motion about the center of rotation. Again, a constant pitch rate is specified in the vector file while holding α at zero. In order to estimate the derivative with respect to pitch rate through finite difference approximation, at least two data points are required, each one at a different value of q; more points are necessary to demonstrate that the stability derivative lies in the linear range.

Initially, C_{mq} about the leading edge is estimated by both the non-inertial and transpiration methods and compared to the analytical results predicted by thin airfoil theory, corrected for compressibility by the Prandtl-Glauert correction. A broad range of instantaneous pitch rates is applied to the airfoil through both means in order to determine the quasi-steady moment due to each rate. Stability derivatives are then estimated by finite difference equations between points. The results are presented in Figure 4.19, below, with both the theoretical line of C_m versus q and the non-inertial data points, as well as the transpiration data points. Although the STARS predictions are slightly higher than the theoretical values, the linear trend throughout the range of pitch rates is demonstrated for both the non-inertial and transpiration data points. The non-inertial data set is closer to the thin airfoil theory in both value and slope than the transpiration data set.

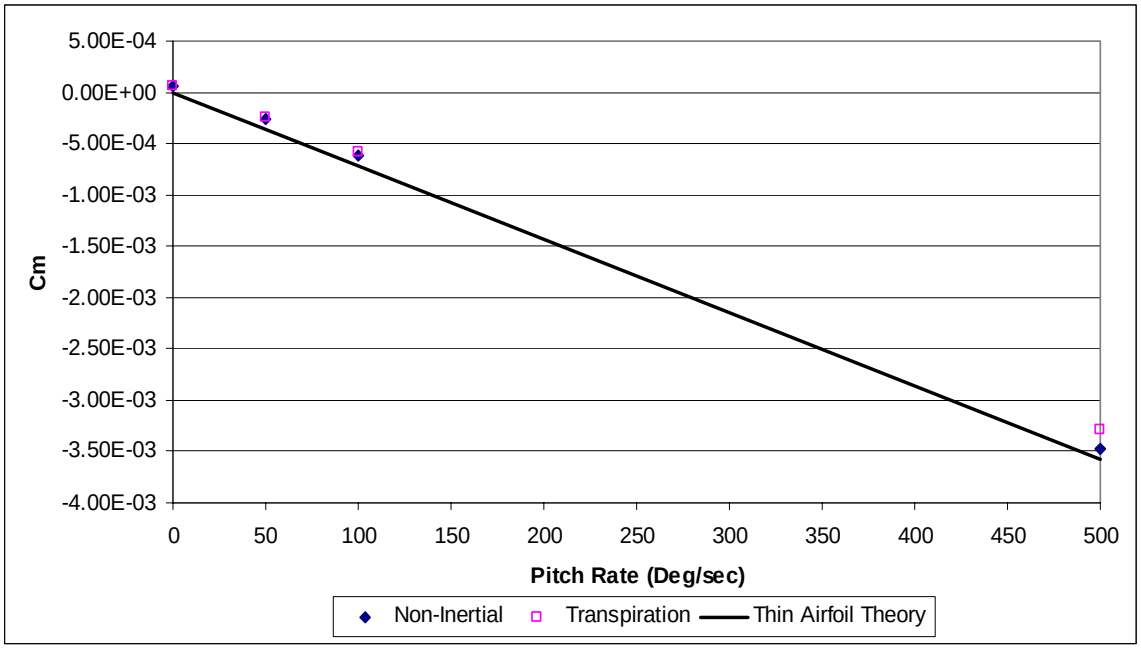

Figure 4.19: Pitch Moment Coefficient Due to Pitch Rate Only

From the above figure, the analytical and STARS predicted values for C_{mq} can be determined. The values for C_{mq} for all cases along with their percent difference from the analytical value obtained from thin airfoil theory are presented in Figure 4.20. From the figure, the percent difference more than doubles when using transpiration as opposed to the non-inertial rate specification; however, the percent difference is still sufficient for preliminary estimates.

	Analytical	Non-Inertial	Transpiration
Cmq	-3.293	-3.174	-3.005
% Diff	-	-3.635%	-8.759%

Figure 4.20: Comparison of Pitch Damping Results for Airfoil Test Case

To further explore this test case, C_{mq} was estimated for varying pitch locations. At each location, C_{mq} is determined through the finite difference approximation between a pitch rate of 0 and 20 deg/sec. These computational experiments were conducted using both the non-inertial and transpiration formulations. Because the forces do not change with pitch location for the zero pitch rate case, the same data can be use at each location

if the forces are properly shifted in order to determine the pitch moment for each pitching location at zero *q*. At each location, the dynamic file is given the appropriate non-inertial origin or a new vector file is generated with the origin of rotation properly indicated. Figure 4.21 presents the results of this examination for various *l*/c locations, where *l* is the distance from the center of rotation to the leading edge, positive for rotating aft of the leading edge. The values predicted by Theodorsen lie directly on top of those predicted by thin airfoil theory. The Datcom method and the method presented in Nelson's text are very similar, differing only slightly as the origin of rotation is moved further from the airfoil. The STARS non-inertial and transpiration data also seem very similar to each other and accurate to the analytical values.

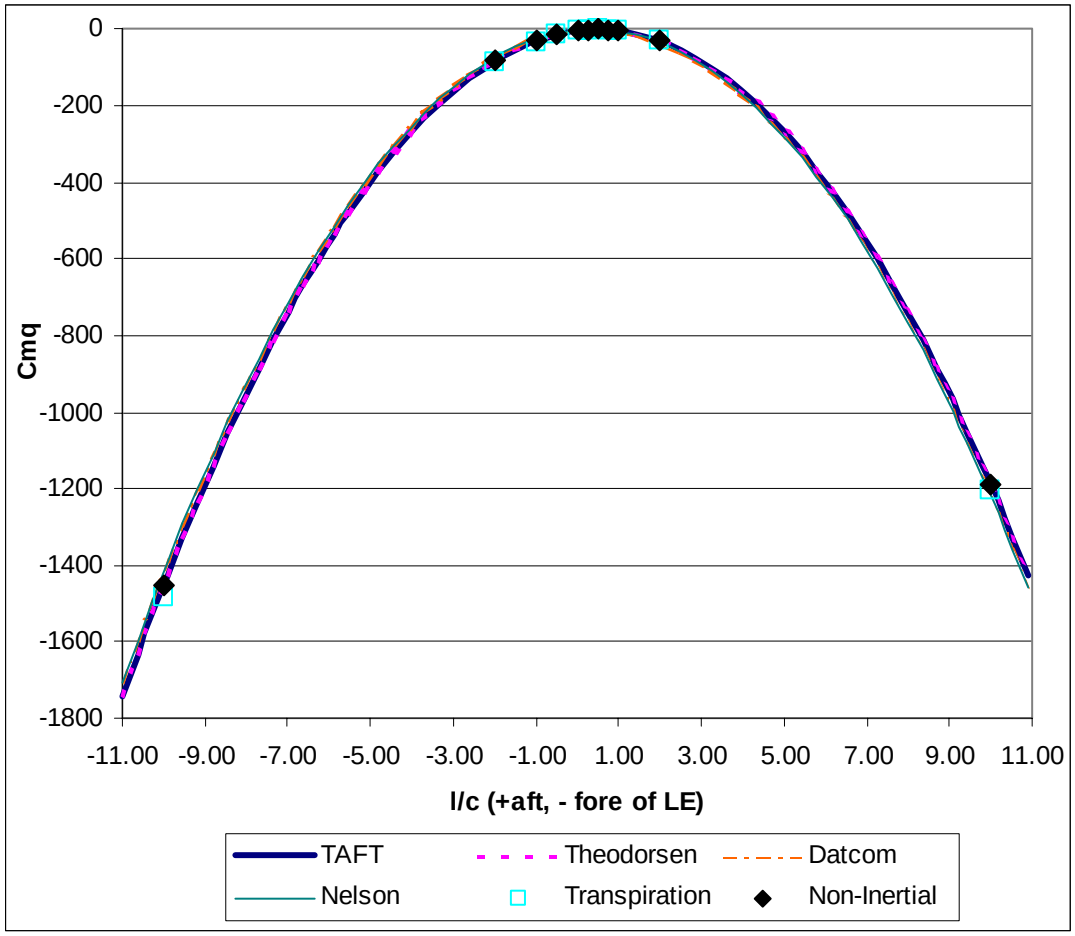

Figure 4.21: Pitch Damping Coefficient Versus Pitch Location

Figure 4.22, below is the same graph as in Figure 4.21, but focused on a smaller range with the addition of 10% error bars to examine the results more closely. The non-inertial and transpiration data still match the thin airfoil theory and Theodorsen lines, but the differences between these and the Datcom and Nelson's method are highlighted. Both the Datcom method and Nelson's method are based on the assumption that the lift produced acts at the quarter chord, which is correct when pitching about a point away from the airfoil. However, when pitching about a point near or on the airfoil the center of pressure is no longer at the quarter chord, making the assumptions of the two methods invalid. STARS transpiration and non-inertial rate specifications are accurate even in this region, with the non-inertial data more closely approximating the theoretical values.

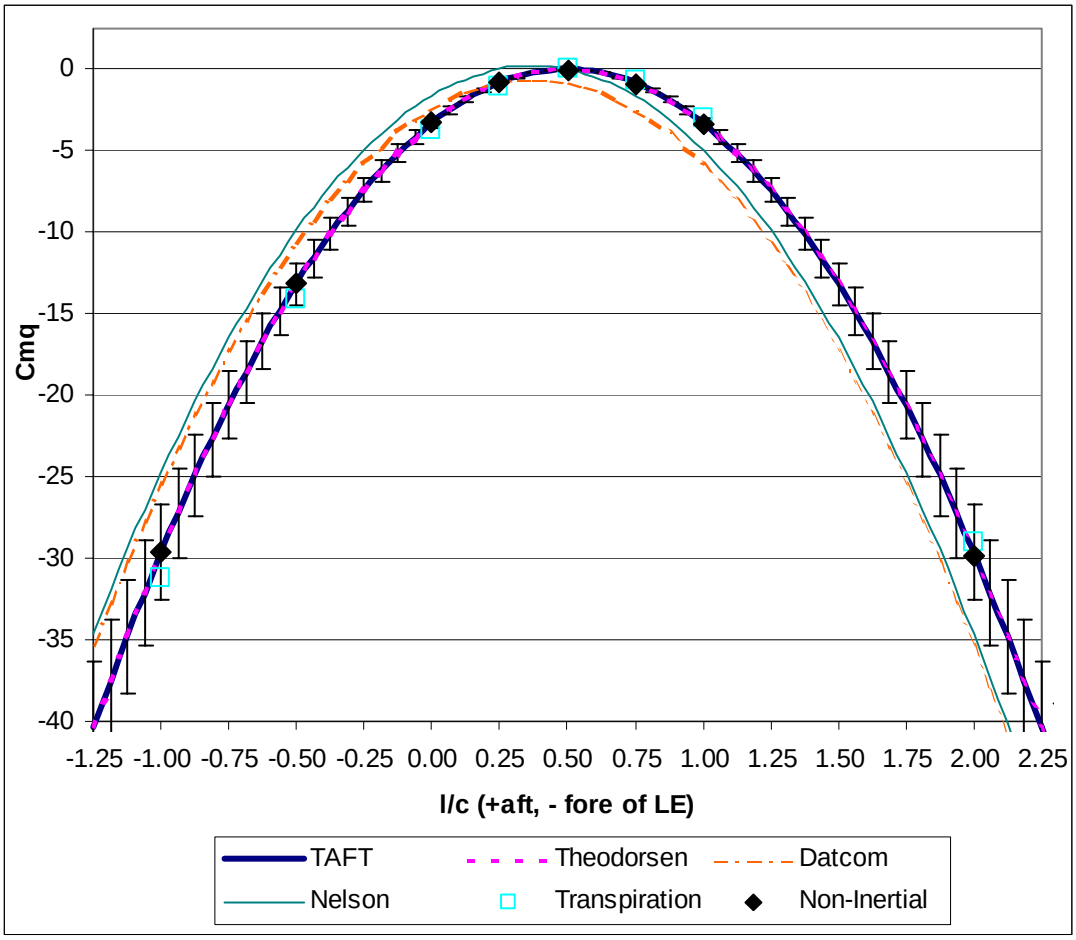

Figure 4.22: A Closer Look at Pitch Damping Coefficient Versus Pitch Location

This simple test case demonstrates the viability of separating the effects of velocity from position. Due to this separation, the conning or oscillatory motion implemented in other methods [Park 1999] is not required to ensure that the angles remain in the linear range. In addition, the method is completely general, in that a model is not needed and a model form does not have to be assumed; no geometry or flow restrictions are required due to model form or assumptions. Even coupling between the longitudinal and lateral directions is permissible, which would severely hinder the accurate estimate of stability derivatives by any method employing the decoupled equations of motion, such as the maximum likelihood estimator. Iliff [1976] states that flight experiments that failed to be properly identified by the maximum likelihood estimator contained coupling of the longitudinal and lateral directions or locally transonic flows, neither of which should cause failure of the decoupled boundary condition method.

In the following sections, the first two cases presented will be reexamined with this new method and compared to both previous results and analytical predictions. Following that presentation, a slightly more complicated three-dimensional case will be examined and compared to the Datcom methods. Then finally, a full aircraft, the F-18A, will be evaluated with this new method and compared to flight test data in the transonic regime.

4.2.2 Horizontal Tail

Since the separation of velocity from position has shown itself to be a viable method for determining stability derivatives, this process will be applied to the forced oscillation test cases. Although not required, this case will use an excitation signal and the ARMA model as before, but only in order to better compare with the results of the previous method. The first case examined was the horizontal tail pitching about a point 10.998 inches fore of the leading edge. Figure 4.1 depicted the geometry of this test case, and is repeated below. For this test case, the stability derivatives will be estimated by the same process as before with the exception that the pitch rate will be excited independently of the pitch angle. This is accomplished through the modified boundary condition equation discussed in the Methodology Section.

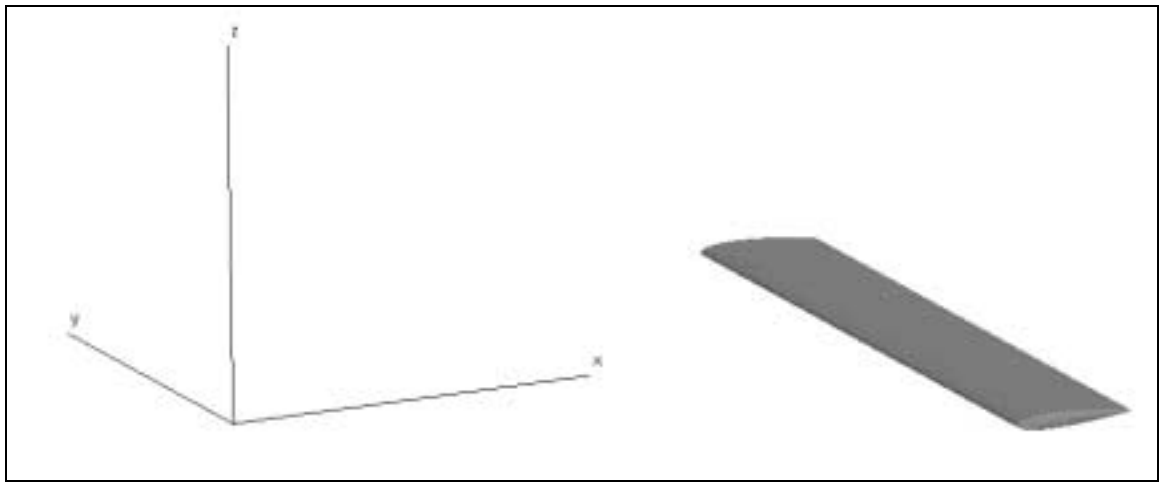

Figure 4.1: Geometry and Axis of Rotation for Horizontal Tail

For an accurate comparison with the previous results of this test case, the exact same excitation signal is used; the velocity excitation signal is applied during one computational run and the position excitation during a separate run. The moments produced by the separate excitations are then summed to generate the total moment due to position and velocity at any given instant of the excitation signal. Figure 4.23 below

shows the angle and rate components of the pitch moment coefficient as well as the summed coefficient. The phase and amplitude effects of each component are reflected in the line representing the combination of the two component signals.

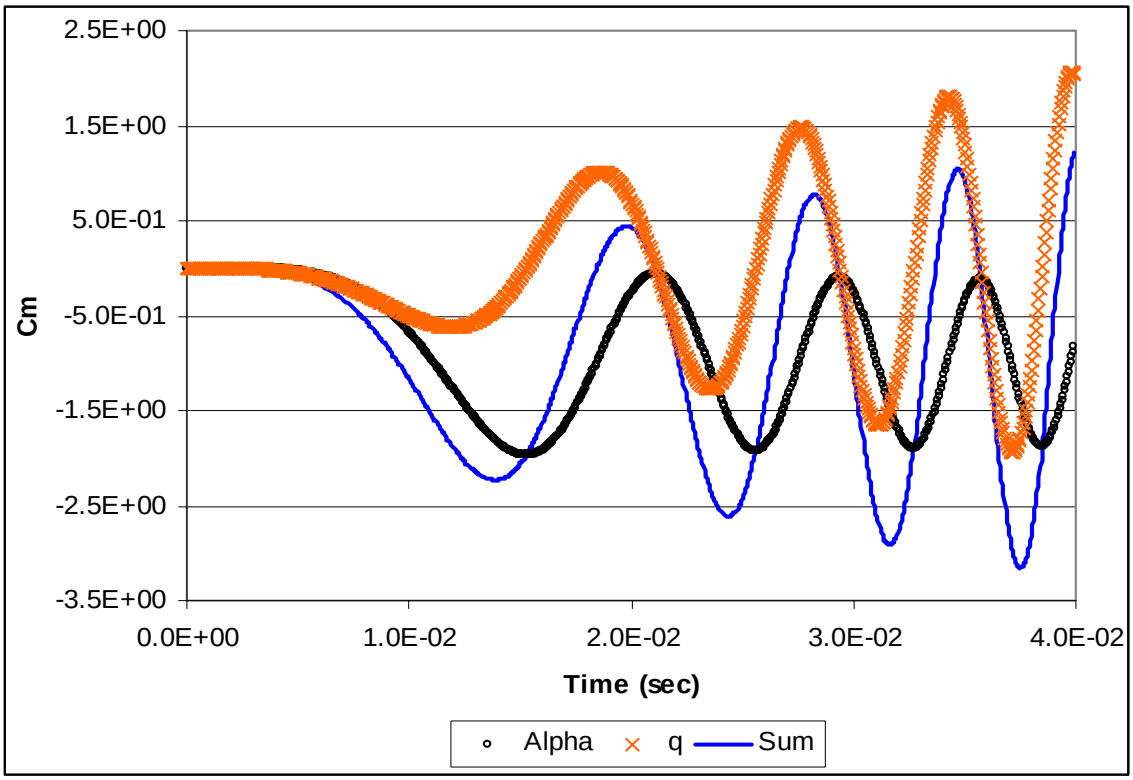

Figure 4.23: Pitch Moment Coefficient from Separate Excitation

Using the summed pitch moment coefficient time history for the parameter identification as before, the ARMA model that best represents the data is the 23-21 model. This ARMA model had the minimum RMS of the cross-correlation. Model order was determined by the same model sweep as before, na 1 to 50 and nb 3 to 50. A comparison of the ARMA model and the STARS data can be seen in Figure 4.24. The 23-21 model does an excellent job of fitting the data over the entire range, indicating that the stability derivative extracted from the ARMA model will be accurate as well.

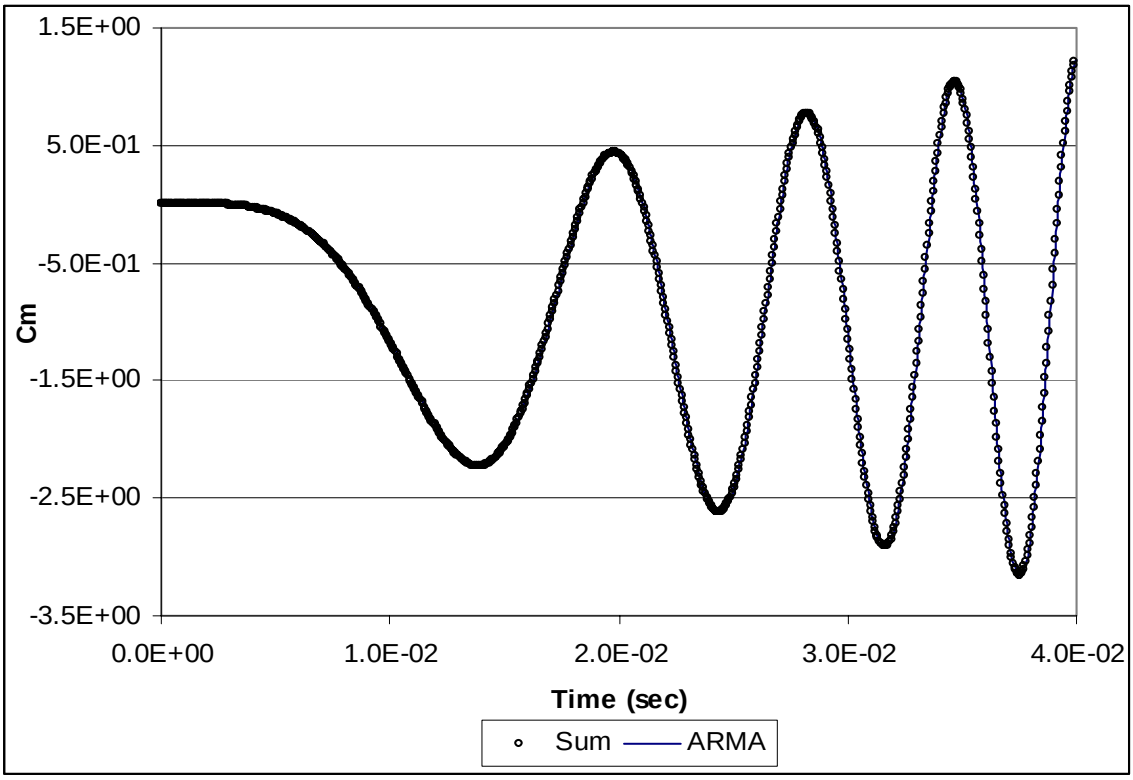

Figure 4.24: Comparison of STARS Data and ARMA Model

From the model coefficients and the previously discussed spreadsheet, Figure 4.7, values for the stability derivatives were determined and presented in Figure 4.25. The 3-10 model had the minimum RMS of the error, but was noticeably different from the 23-21 model and did not match the data as well in regions of large pitch rate; however, the error in the stability derivative's estimate from that model was only slightly higher than the 23-21 model. The percent difference of the stability derivative obtained through the separate excitation of angle and rate is comparable to the averaged values obtained by the simultaneous excitation.

Cmalpha	Cmq
-28.70179	-334.478
-1.3669%	-4.0228%

Figure 4.25: Stability Derivatives Extracted from 23-21 ARMA Model

While the best model for the simultaneous excitation was a 35-14 model, the 23-21 model was best for the independent excitation; yet, both models produced comparable results. Figure 4.26 demonstrates the reason for the difference in the models. This figure contains the forced oscillation data as well as the summed data from the separate excitation. The required models are different because the data sets contain differing amounts of unsteadiness. For the simultaneous case, more unsteady terms are excited resulting in a higher order model to remove the unsteady effects in order to determine the quasi-steady stability derivatives. By exciting the terms independently, the summed data contains less unsteadiness; however, the ARMA model still properly models the terms that are present, demonstrating the flexibility of the ARMA model in capturing the relevant flow physics.

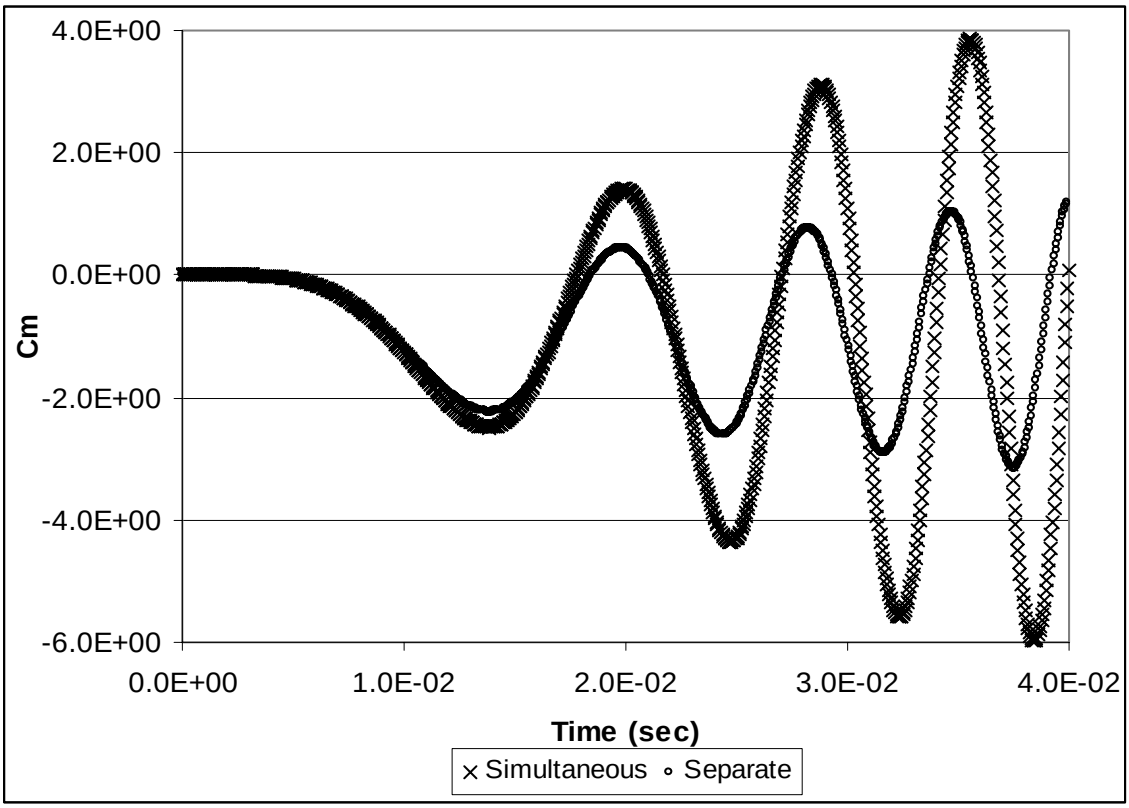

Figure 4.26: Pitch Moment Comparison of Simultaneous and Separate Excitation

Another interesting comparison is found in Figure 4.27, below, this figure plots the total pitch moment coefficient from the separate excitation to the analytical response for the same excitation. The small percent difference in the rate stability derivative becomes perceptible only at the largest values for pitch rate. For all reasonable values of pitch rate, the difference is unnoticeable. Since the separate excitation can accurately match the analytical response with out extracting the stability derivatives from the ARMA model, the excitation signal and ARMA model may not even be needed.

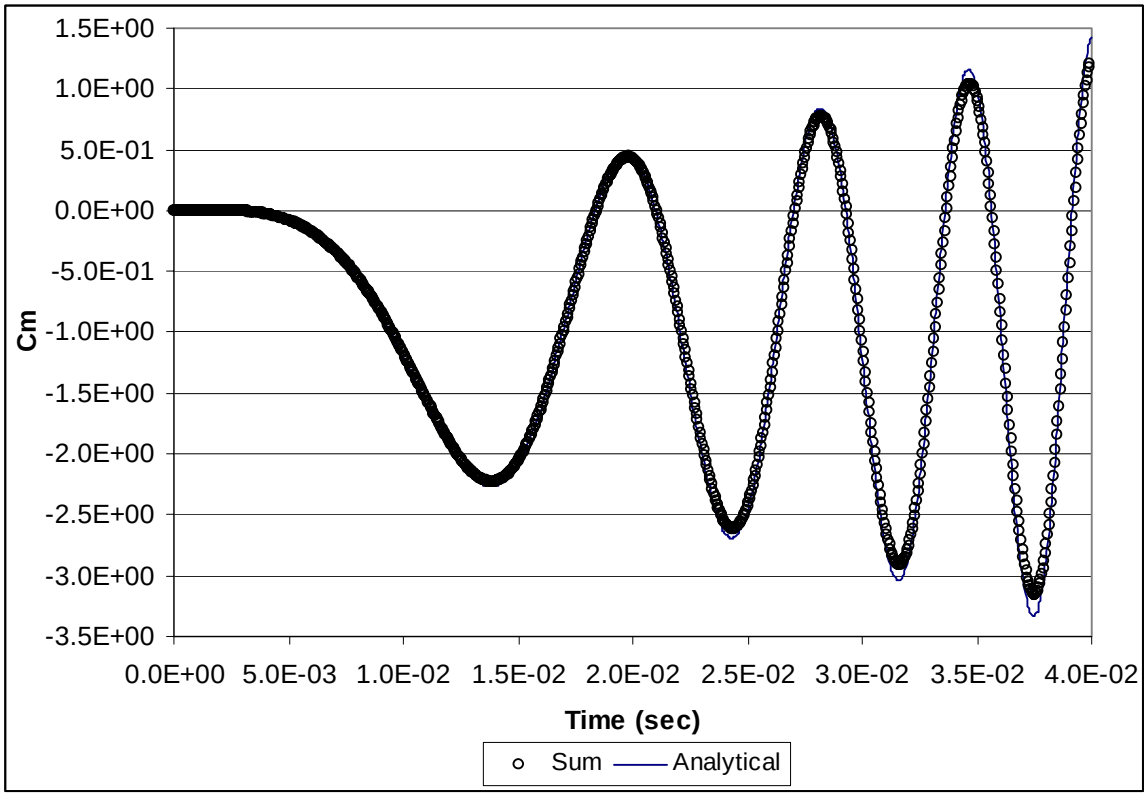

Figure 4.27: Pitch Moment Comparison of Separate Excitation and Analytical

As with the airfoil test case, the pitch-damping coefficient for the horizontal tail can be estimated by the finite difference approximation between the moments produced by two different quasi-steady rates. For the horizontal tail, a zero pitch rate case was run, as well as a 50 deg/sec case, and applied in three different methods: non-inertial, large scale transpiration, and small scale transpiration. The first mode shape file generated for

the transpiration case used a large scaling factor of 180/π in order to input rates as radian per second. However, scaling this large can distort the results in a way similar to the large displacements at which the accuracy of transpiration begins to falter. Generating a new mode shape file with a scaling of 1 produces better results, thereby eliminating the errors produced in violating the small angle limitations of transpiration.

Once the loads converge for all cases, C_{mq} can be estimated for each case. The estimates of the stability derivatives including the percent difference from analytical are presented in Figure 4.28. Here, the effects of a large scaling factor in the vector file can be seen as the predicted value is further from the analytical. While the non-inertial formulated generated the best estimate, the time required was also larger. Although the solution does not need to be time accurate, the non-inertial rate specification requires at least a first-order time accurate solver; however, at each time step only a few local iterations are required, thereby reducing the time compared to a converged solution at every time step. The transpiration method generated acceptable predictions in a time efficient manner, and was, therefore utilized for the more complex test cases. If greater accuracy is needed for rate based stability derivatives, the converged transpiration results can be used as initial conditions for the higher order solver in order to reduce the time required for convergence.

	Analytical	Non-Inertial	Small Scale	Large Scale
Cmq	-348.5	-356.3	-371.0	-312.2
% Diff	-	2.241%	6.450%	-10.42%

Figure 4.28: Rate Dependent Stability Derivative Estimates with Percent Differences

For the angle-based stability derivates, a steady state solver can be implemented and specify flow conditions that simulate the steady state angles for the derivative estimation. The grid convergence study for the horizontal tail provides all the

information required to estimate $C_{m\alpha}$. Using the slope of the pitch moment coefficient versus angle of attack plot, the results are within 2% of the analytical results without any further effort.

4.2.3 Dihedral Wing

Although the forced oscillation technique failed to produce accurate estimates of the stability derivatives due to the unsteady interaction of the position and velocity effects, the derivatives can be easily estimated by the same procedure as above: a decoupled boundary condition for the quasi-steady rate derivatives and the results of the grid convergence study for the angular derivatives. The geometry for this test case is presented in Figure 4.12, which is repeated below for clarification of discussion. The flight conditions are standard sea level at Mach 0.4 with a chord of 2 inches and a span of 8 inches with an NACA 0009 cross-section.

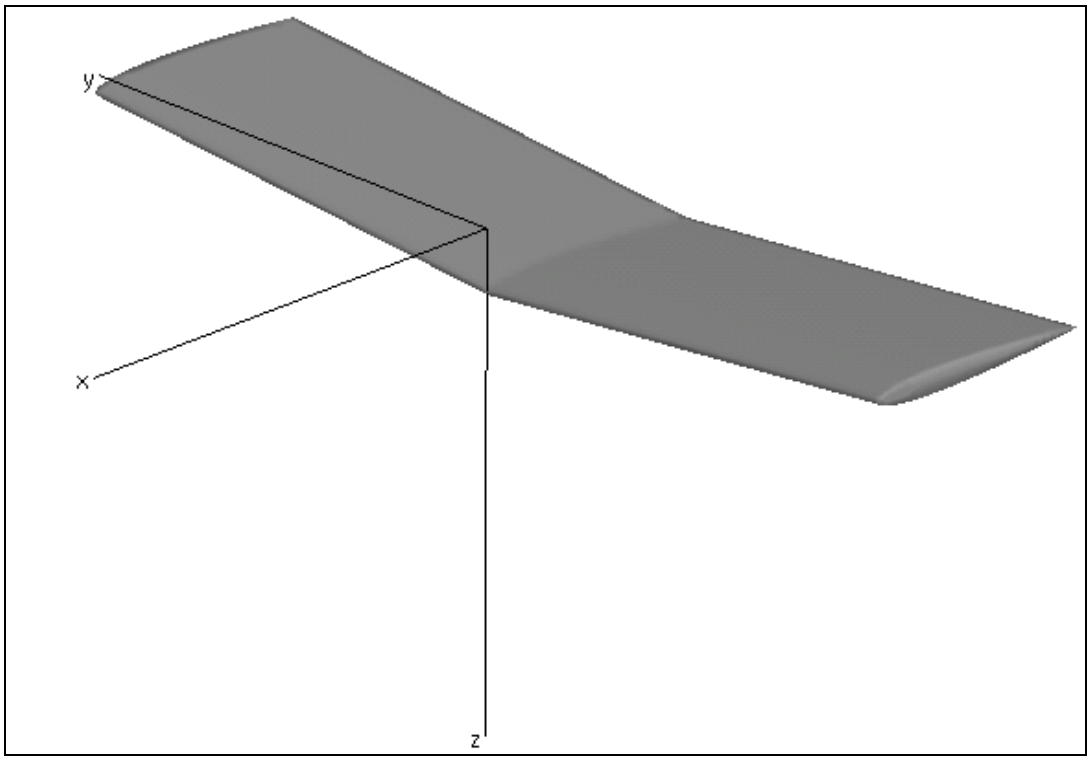

Figure 4.12: Geometry of Dihedral Wing

The stability derivatives for the dihedral wing are estimated by both the non-inertial formulation and the small-scale transpiration rate specification. Pitch rates of 0, 50, 100, and 500 deg/sec are specified in separate cases while holding angle of attack, α, constant at zero. All pitch rates for both cases fall in the linear range, as evidenced in Figure 4.29 by the accurate representation of each data set by a linear regression that fits each data set in a least squared sense. This line serves a dual purpose: not only does it demonstrate the linearity of the data sets, but the slope of the line also yields the stability derivative, C_{mq}.

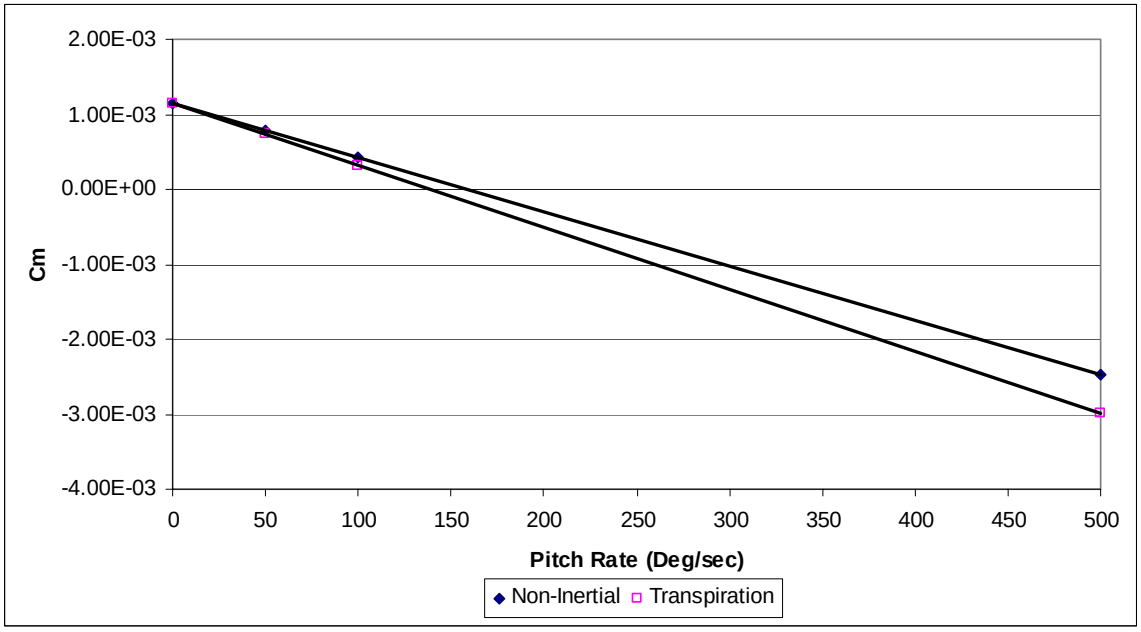

Figure 4.29: Pitch Moment Coefficient Versus Pitch Rate

Using the slopes of the lines in Figure 4.29, the stability derivative estimates of Figure 4.30 are produced. The analytical results stem from thin airfoil theory corrected for aspect ratio as described in the Datcom. Again the results show that the non-inertial specification generates the most accurate estimates but with greater computational and time costs. The transpiration method produces less accurate but still viable estimates for

the stability derivative when considering the previous method's failure to reasonably estimate the derivatives with a great deal more effort.

	Analytical	Non-Inertial	Transpiration
Cmq	-2.285	-2.228	-2.534
% Diff	-	-2.506%	10.90%

Figure 4.30: Rate Dependent Stability Derivative Estimates with Percent Difference

Likewise, the $C_{m\alpha}$ stability derivative can be estimated from the slope of the pitch moment versus angle of attack curve in Figure 4.13 used in the longitudinal grid convergence study. Here the analytical results stems from the method presented in Nelson's text. This method works for the $C_{m\alpha}$ term because the moment is independent of the pitch location unlike the C_{mq} term, which is highly dependent on the origin of rotation. Again as seen in Figure 4.31, STARS is capable of accurately predicting the stability derivatives without an excitation signal or ARMA model, greatly simplifying the process and reducing the workload.

	Analytical	STARS
Cmalpha	-1.138	-1.165
% Diff	-	2.400%

Figure 4.31: Stability Derivative Estimate with Percent Difference

Instead of investigating the lateral stability derivatives of the dihedral wing, a more complex test case involving the dihedral wing will be examined. This test case is a simplified aircraft with a main wing, a horizontal tail, and a vertical tail. The main wing for the next case will be the dihedral wing of this case. In this way, the lateral motion of the dihedral wing will be investigated while simultaneously increasing the complexity to an even more complex test case, the full F-18A.

4.2.4 Simple Aircraft

As mentioned above, the geometry of this simple aircraft test case consists of a main wing from the dihedral test case, a horizontal tail, and a vertical tail. Figure 4.32 displays the geometry for this case pictorially, while Figure 4.33 contains the numerical sizing of each of the surfaces. The lengths, lw, lv, and lh, are the distances in the x-direction from the leading edge of that surface to the origin of rotation. Unlike the main wing that is set below the origin, the root chord of both the horizontal and vertical tails lies in the x-y plane of the origin. The flight conditions are as before, Mach 0.4 and standard sea level.

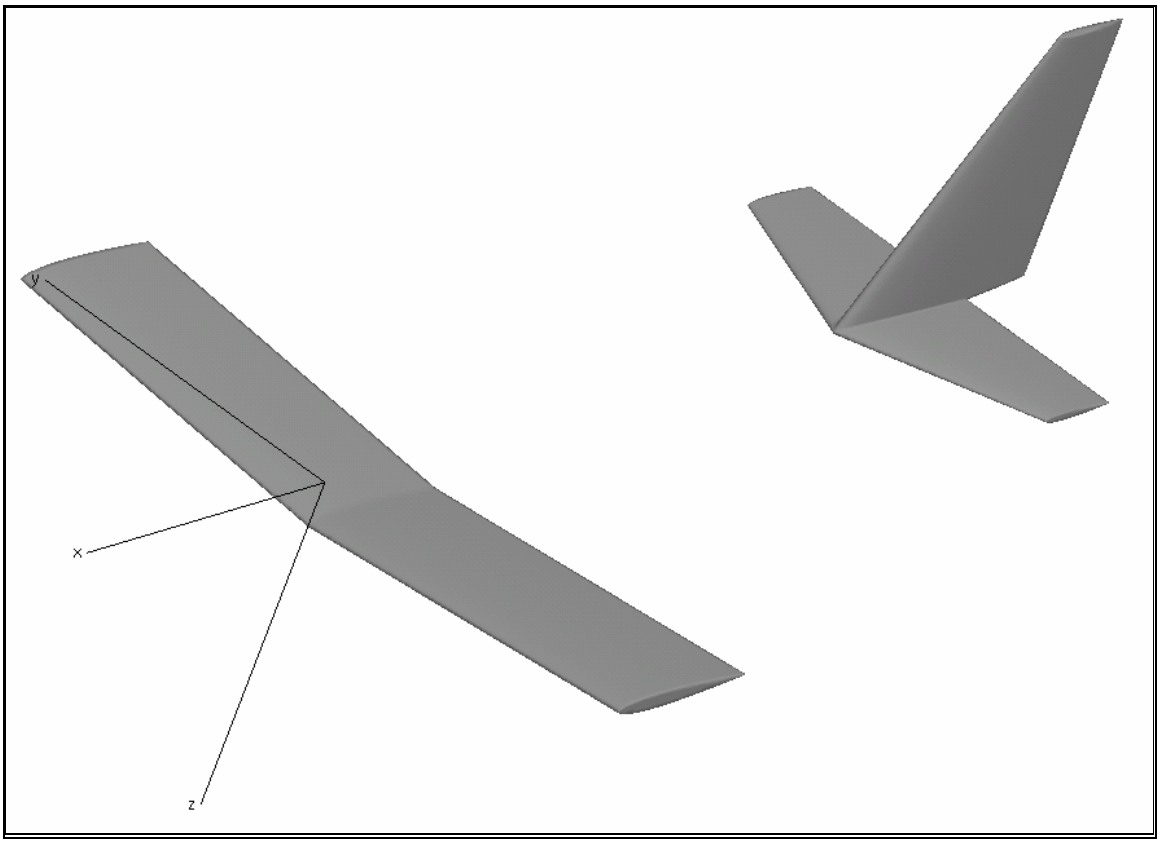

Figure 4.32: Geometry for Simplified Aircraft

wing				
S	b	c	lw	dihedral
16.00	8.00	2.00	0.00	5.00
horizontal tail				
S	b	cbar	lh	c/4 sweep
6.00	4.00	1.50	8.00	20.56
vertical tail				
S	b	cbar	lv	c/4 sweep
6.00	3.00	2.00	8.00	26.57

Figure 4.33: Dimensions of Simplified Aircraft

The grid for the dihedral wing remains the same as the results had sufficiently converged. Similarly, the grids for the horizontal and vertical tails were both converged independently in the same manner as the dihedral wing. As the surfaces were generated and the grid refined separately, the sizing of the vertical tail is proportionally larger than intended; however, this will be helpful in demonstrating interference effects often not included in analysis. In order to more accurately compare with the predictions of the Datcom, initially the aircraft will be treated as isolated surfaces. This is achieved by applying the steady angle or quasi-steady rate about the origin of rotation with only one surface present in the computational domain. The effects of each will be combined and compared with the Datcom results for isolated surfaces. Then, the system as a whole is examined with a slightly modified wake grid, and the results compared to the Datcom methods including the available interference approximations.

Transpiration is used to simulate all the rates while holding angles at zero and the angles are applied on separate runs through transpiration with zero rates. For angle derivatives, α was set to 0 and 5 degrees while β went from 0 to -5 degrees. The rate derivatives were evaluated between 0, 10, and 20 deg/sec; the latter only to ensure the linear range is maintained in the derivative estimation. The wing and vertical tail were given sideslip angles and yaw rates, while the wing and horizontal tail received the angle

of attack and pitch rates. Appendix B contains the calculations of the Datcom methods for the isolated surfaces, and Appendix C demonstrates the calculations involving interference effects. The results of the isolated stability derivative estimates are displayed in Figure 4.34. With the exception of $C_{l\beta}$, most of the stability derivatives are in good agreement with the Datcom prediction, and the main source of error is the wing. STARS predicts a more stable contribution from the wing than Datcom, but the contribution from the vertical tail is quite accurate. The remaining derivatives are sufficiently comparable to the Datcom approximations.

	Clbeta		
	Vtail	wing	total
STARS	-1.420E-01	-2.929E-05	-1.421E-01
Datcom	-1.480E-01	-4.900E-02	-1.970E-01
% Diff	4.035%	99.94%	27.89%

	Clr		
	vtail	wing	total
STARS	3.750E-01	1.961E-02	3.946E-01
Datcom	3.510E-01	0.000E+00	3.510E-01
% Diff	-6.83%	-	-12.42%

	Cmalpha		
	htail	Wing	Total
STARS	-4.842E+00	-9.318E-01	-5.774E+00
Datcom	-5.375E+00	-1.014E+00	-6.389E+00
% Diff	9.92%	8.10%	9.63%

	Cmq		
	htail	wing	total
STARS	-4.657E+01	-1.958E+00	-4.853E+01
Datcom	-4.770E+01	-1.391E+00	-4.909E+01
% Diff	-2.38%	-40.73%	1.15%

	Cnbeta		
	Vtail	wing	total
STARS	9.403E-01	-3.088E-06	9.403E-01
Datcom	9.360E-01	0.000E+00	9.360E-01
% Diff	-0.46%	-	-0.46%

	Cnr		
	vtail	wing	total
STARS	-2.506E+00	2.067E-03	-2.504E+00
Datcom	-2.223E+00	0.000E+00	-2.223E+00
% Diff	-12.74%	-	-12.64%

Figure 4.34: Stability Derivatives Estimated for Isolated Surfaces

The Datcom values are recalculated in Appendix C to account for the interference effects in order to compare with the STARS predictions for the whole system. As before, transpiration is used to separately excite the angles and rates to the same extent. Now, the whole system is given sideslip, angle of attack, pitch rate, and yaw rate separately and allowed to converge on the steady or quasi-steady loads. Figure 4.35 that follows contains the results of the stability derivative estimates with the new Datcom predictions

including the available interference estimates as well. Again, the results are in general comparable to the Datcom predictions; however, $C_{m\alpha}$ and C_{nr} have unexpectedly high percent differences. The difference in $C_{m\alpha}$ could stem from an under-prediction of the downwash effects on the horizontal tail in the Datcom leading to more pitch stability. C_{nr} is dominated by the vertical tail which is a motion similar to C_{mq} for a horizontal tail, therefore the error stems either from the wake of the wing or the presence of the horizontal tail. As the wing is producing little lift at zero angle of attack, the wake influence should also be minimal. The presence of the horizontal tail is accounted for in the Datcom method by altering the aspect ratio of the vertical tail. These calculations are highly empirical and could therefore be the cause of the large difference. Some of the error is undoubtedly due to the transpiration assumptions and the CFD routine itself, but these errors have shown themselves to be minimal in previous cases.

	Clbeta	Clr	Cmalpha	Cmq	Cnbeta	Cnr
STARS	-1.905E-01	4.399E-01	-3.710E+00	-5.252E+01	1.240E+00	-3.571E+00
datcom	-2.310E-01	4.330E-01	-4.304E+00	-4.909E+01	1.156E+00	-2.745E+00
% diff	17.52%	-1.594%	13.79%	6.969%	-7.271%	-30.10%

Figure 4.35: Stability Derivatives Estimated for Simple Aircraft

4.2.5 F-18A

NASA's Dryden Flight Research Center has used the F-18 platform to test a variety of technologies from thrust vectoring with the High Alpha Research Vehicle (HARV), to aeroelastic control with the Active Aeroelastic Wing (AAW) program, and numerous other experiments with the Systems Research Aircraft (SRA). As a result of this testing, a great deal of literature and experimental data is available for the F-18.

The computational model obtained from NASA Dryden is an F-18A single seat configuration; however, the available transonic flight-estimated stability derivatives were

generated with F-18B two-seat configuration. While the canopy is distinctly different, Moes, Noffz, and Iliff consider the F-18B an acceptable aircraft to estimate the stability derivatives for the baseline F-18 configuration in their work [Moes 2000]. They state this because their work is focused on generating improved estimates of the stability derivatives in their aerodynamic model. As such, the increment between the flight-test values and the aerodynamic model for the F-18B can be applied to the aerodynamic models for the other variations of the F-18. The effects of the different configurations are accounted for in the baseline aerodynamic model, so the increments in the stability derivatives are assumed applicable to all variants of the F-18. However, the baseline aerodynamic model for the F-18A was not available for comparison, so the stability derivatives estimated by STARS for the F-18A are cautiously compared with the F-18B stability derivatives presented in their paper. Figure 4.36 below is a picture of the F-18sra from the NASA Dryden website.

Figure 4.36: Picture of the F-18sra Used in Flight Testing

Considering the above discussion, the following seeks to outline some of the differences between the computer surface model of the F-18A and the actual F-18B as well as the expected consequences of these differences. The main difference, as previously mentioned, is the canopy. With a smaller canopy, the F-18A is expected to be more weathercock stable, which means $C_{n\beta}$ should be more positive. The computer model is also simplified by removing the wingtip pods, the effect of which is unknown but for this analysis assumed small. Other simplifications with negligible effects include the removal of small fins, instrument probes, tail hook, and similar surfaces.

A far field boundary condition is applied to the engine inlet and exhaust nozzle to simulate the flow in these regions. The effects of this specification were examined by

comparing the results with those of walled inlets and exhaust nozzles. For such a drastic change in the surface definition of these surfaces, the maximum percent difference in the rotary stability derivatives was 7.8% for C_{np} while the remaining differences were less than 3%. Therefore, applying a far field boundary on the engine inlet and exhaust nozzle is sufficient for this analysis. The computer model of the F-18A can be seen in Figure 4.37 and compared to Figure 4.36 of the actual test aircraft.

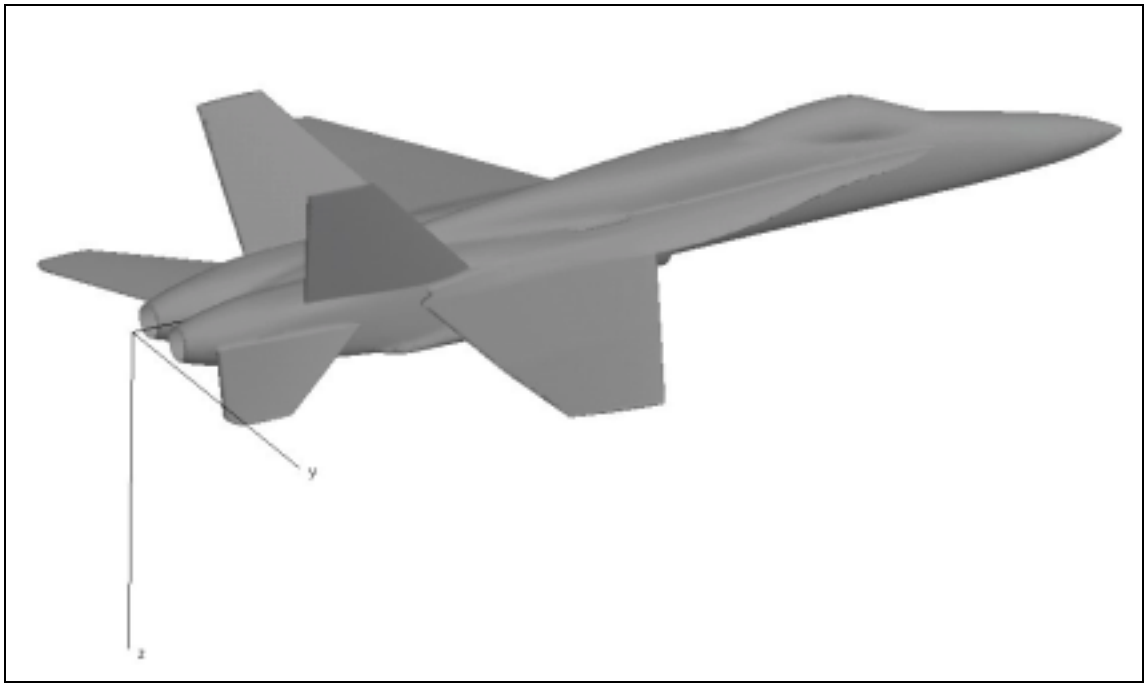

Figure 4.37: Picture of the F-18A Model Used in STARS

Another consideration is the size and complexity of this test case; as such, the grid refinement process was very limited and only examined the effects of the addition of wake elements for the subsonic case. Further grid refinement is necessary before the grid can be deemed fully converged; however, for this case, experimental data was available for comparison and adequate results were obtained with the initial grid. In light of the size of the computational domain, approximately 2.2 million elements, transpiration was

implemented to simulate all angles and rates for this investigation so that the faster steady solver could be used.

For comparison with the available data, the flight conditions were specified as standard day at an altitude of 15,000 feet with Mach numbers of 0.9, 1.1, and 1.3. Except for Mach number, the flow parameters in the control file were identical for every case. A representative control file is presented in Figure 4.38. Three modes are used so that one vector file can simulate each of the three rotary modes, instead of three single mode vector files.

```
&control
dt      = 1.0d-1              mach   = 0.9d,
gamma   = 1.40d0,             alpha  = 0.0d0,
diss    = 1.00d0,             beta   = 0.0d0,
cfl     = 0.5d0,              refdim = 1.0d0,

ncyc    = 5,                  istrt  = .true.,
isol    = 0,                  iaero  = .true.,
idiss   = 0,                  idynm  = .false.,
ipnt    = 1,                  ielast = .true.,
                              ifree  = .true.,
nr      = 3,                  iforce = .false.,
ainf    = 1.268814d4,
rhoinf  = 7.21852d-8,
```

Figure 4.38: Representative Control File for All F-18 Test Cases

The amplitudes of the angles and rates were likewise similar to the values achieved during the flight tests. Figure 4.39 contains the conditions for the eleven cases: one zero case, which is all states equal to zero, and two other cases for each of the five state. At each condition specified in the vector file, all the other values were zero; for example when a yaw rate of 8deg/sec was applied α, β, p, and q were all held at zero. Three data points were generated for each state in order to ensure the derivative estimates remained in the linear range.

Alpha (deg)	Beta (deg)	p (deg/sec)	q (deg/sec)	r (deg/sec)
0	0	0	0	0
3	-3	20	6	4
5	-5	40	12	8

Figure 4.39: Conditions Applied for the Estimation of Stability Derivatives

The solution for each case was allowed to converge until the loads no longer changed. Once converged, the forces and moment were converted into coefficients and the stability derivatives were estimated through finite difference approximation. The estimated rotary stability derivatives were added to the following figures taken from Moes [2000]. He includes qualitative error bars based on the Cramer-Rao confidence levels from a maximum likelihood output-error estimator program. The confidence index is multiplied by a factor of five to visually improve the plot. While no quantitative correlation was made to actual uncertainty, large Cramer-Rao values indicate a poor prediction and small values indicate a good prediction. The solid lines are preflight predicted values based on the linearization of a nonlinear aerodynamic simulator model for the F-18B. No discussion was given as to the origin of the simulator model. Estimates of the stability derivatives with STARS at 15,000 feet altitude are represented by an x inside of a circle.

The first graph presented is $C_{m\alpha}$ for the three Mach numbers seen in Figure 4.40. In the subsonic range, STARS more closely approximates the predicted values while at higher Mach numbers is equally close to the flight determined values. The increased stability predicted at Mach 0.9 would seem to indicate that the grid does not properly capture the downwash effects of the wing on the tail, which is a destabilizing effect. However, this effect does not appear in the sonic cases, implying that the error may not stem from the flow of information downstream but the upstream flow of information. In order to investigate this discrepancy, the number of wake elements was increased

dramatically from the trailing edge of the wing to 50 feet, approximately four mean aerodynamic chord lengths, aft of the tail's trailing edge, bringing the total number of element to almost 3 million. Although this decreased the difference between the flight test data and the prediction by STARS, the change was less than 2% of the refined wake estimate. Another possible explanation is that the grid may not be suitable for the subsonic case where information can travel upstream. If the grid is insufficient, this explanation does not then account for the accuracy of STARS to predict the other subsonic stability derivatives. Also, the estimated values are very close to the predicted values and follow a similar but less dramatic trend.

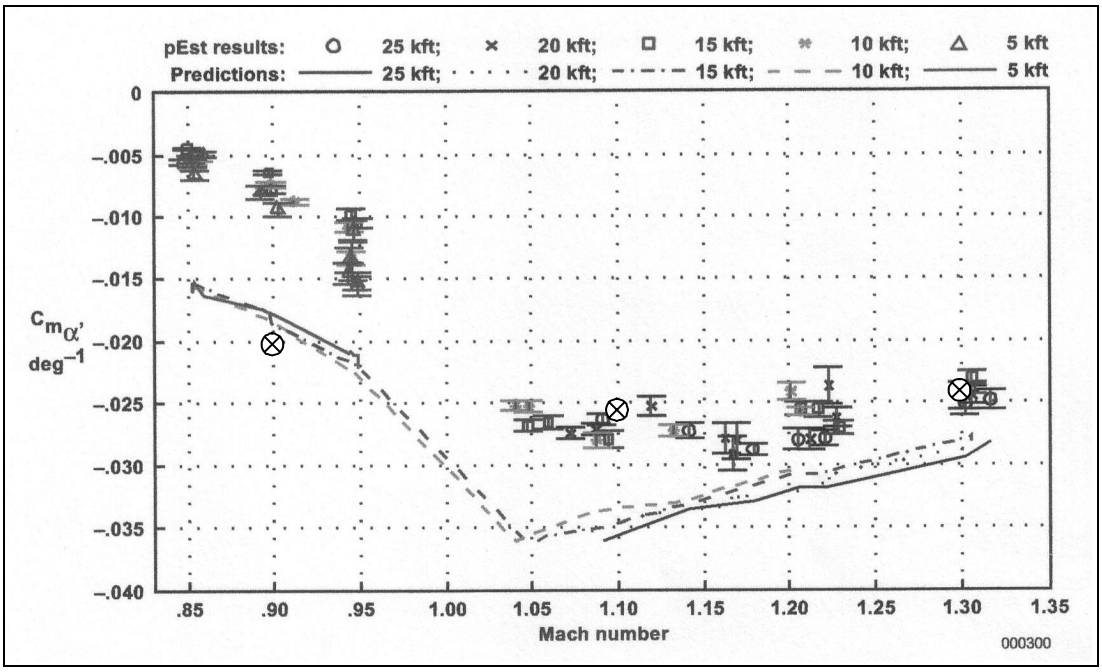

Figure 4.40: Comparison of Flight Test Data to STARS Estimates for $C_{m\alpha}$

The rate dependent longitudinal stability derivative, C_{mq}, is presented in Figure 4.41. The estimates from STARS follow the general trend of the preflight predictions with the high and low Mach numbers corresponding well to the flight estimated values. However, at Mach 1.1, the flight data departs from the trend of the other methods and predicts a smaller magnitude pitch-damping coefficient. The discrepancies in the subsonic case have vanished as flight, STARS, and predicted values correspond nicely as do the values at Mach 1.3.

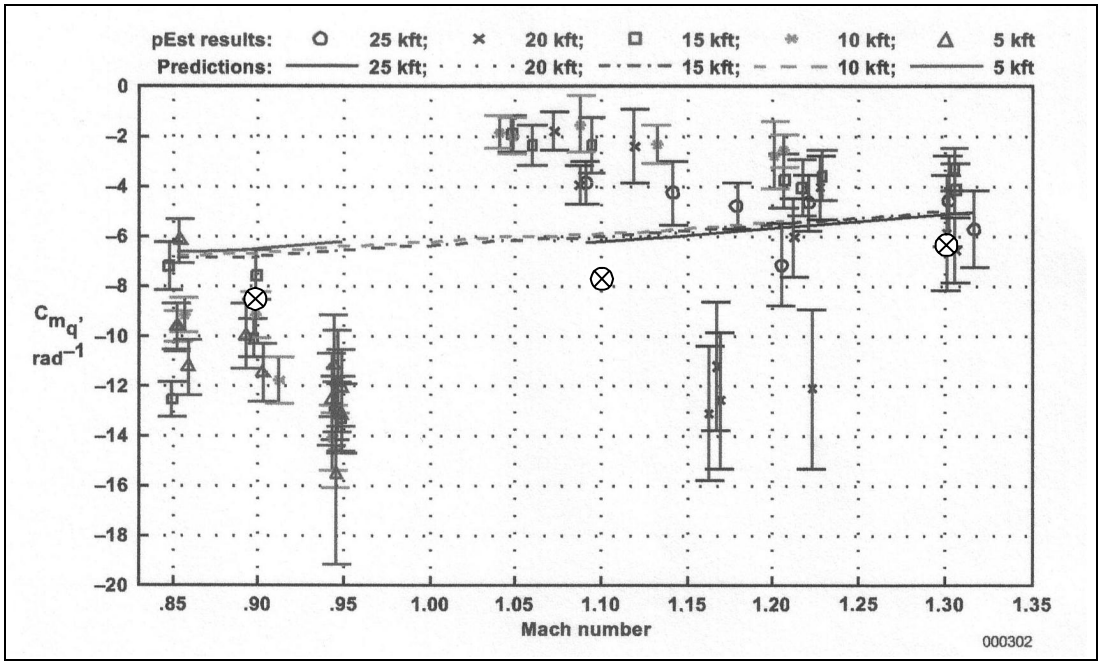

Figure 4.41: Comparison of Flight Test Data to STARS Estimates for C_{mq}

Little discussion is needed for Figure 4.42, as the predictions by STARS of $C_{l\beta}$ match the flight-determined values very well, and nicely follow the same trend as the predicted values. The altitude effects predicted but not seen in the flight-data could be investigated with STARS by simply changing the acoustic speed and density of the free stream; however, the current focus is on the prediction of stability derivatives at 15,000ft.

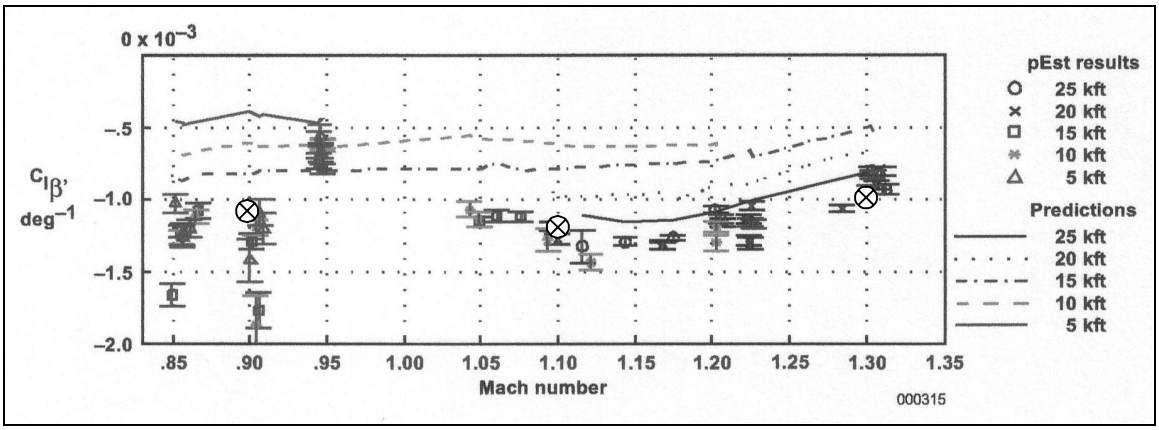

Figure 4.42: Comparison of Flight Test Data to STARS Estimates for $C_{l\beta}$

In the comparison of $C_{n\beta}$ found in Figure 4.43, the canopy effects must be considered. As less canopy area exists for the STARS model, STARS should and does predict a more stable, more positive, derivative at all Mach numbers. The trend in all the data is again quite similar, but the magnitude of the difference changes from the 0.9 and 1.3 case to the 1.1 case indicating that some other effect is taking place.

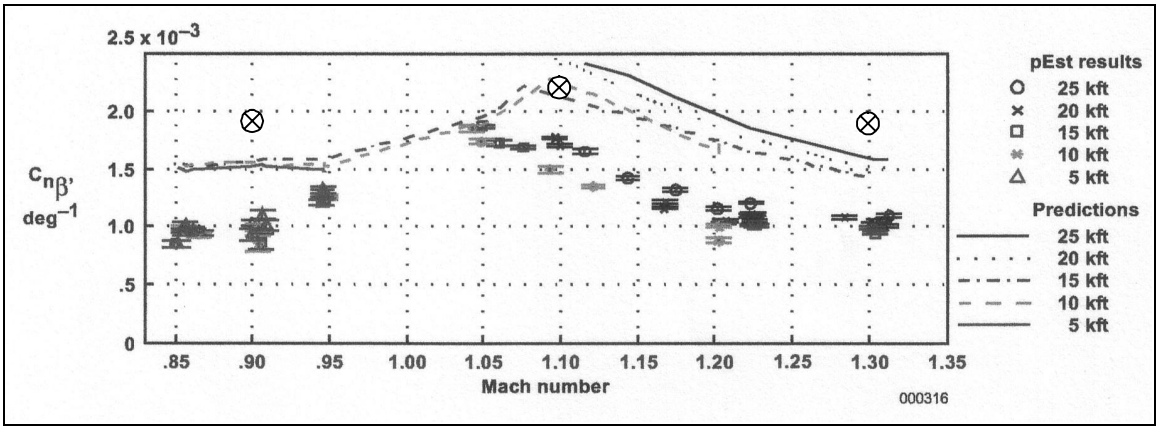

Figure 4.43: Comparison of Flight Test Data to STARS Estimates for $C_{n\beta}$

Figure 4.44 and Figure 4.45 contain the roll rate stability derivatives for roll moment and yaw moment, respectively. For all but two data points, C_{lp} at Mach 0.9 and C_{np} at Mach 1.3, the STARS estimations satisfactorily match the flight determined stability derivatives and the predicted trends. While the cause is unknown, these discrepancies can again be attributed to grid refinement or differences in geometry.

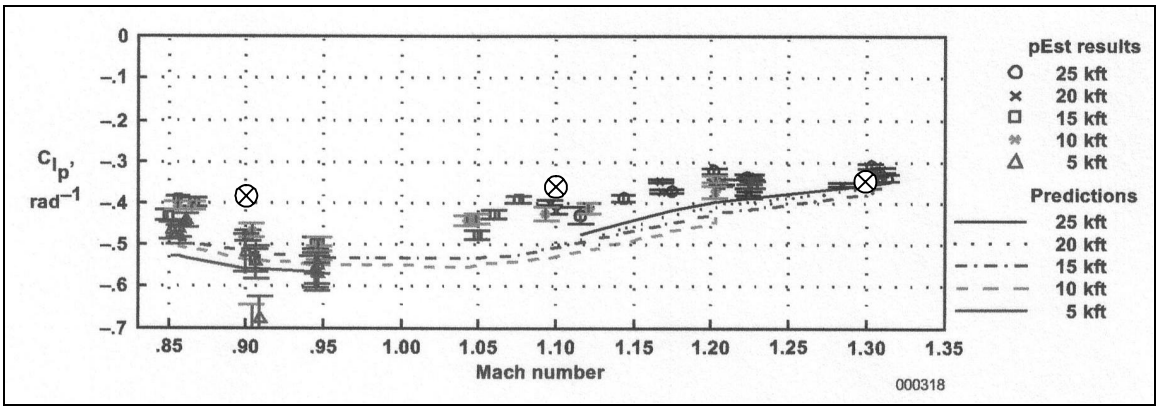

Figure 4.44: Comparison of Flight Test Data to STARS Estimates for C_{lp}

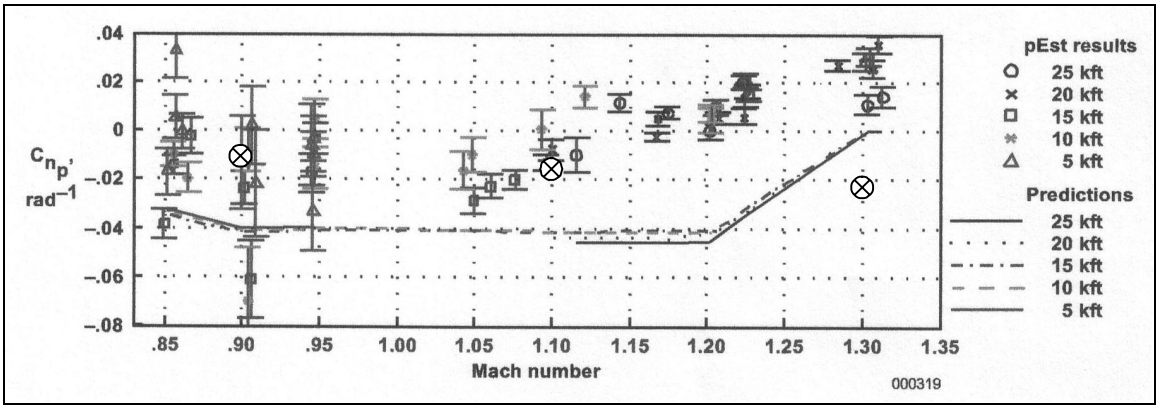

Figure 4.45: Comparison of Flight Test Data to STARS Estimates for C_{np}

The yaw rate stability derivatives for roll moment and yaw moment can be seen in Figure 4.46 and Figure 4.47, respectively. In all cases, the stability derivatives estimated by STARS match the flight estimated values and the predicted trends. The only data point of concern is the C_{nr} estimate at Mach 1.3 which lies within 7% of the predicted values but is further from the cluster of flight generated data.

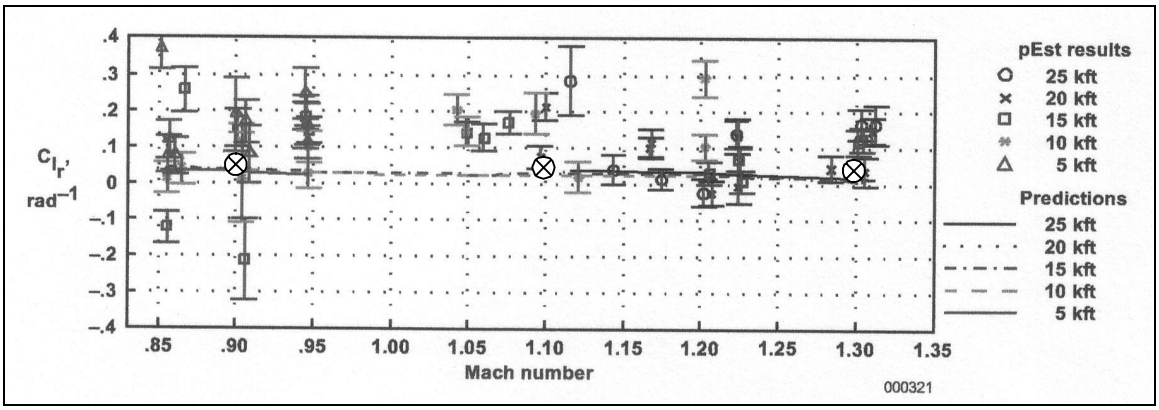

Figure 4.46: Comparison of Flight Test Data to STARS Estimates for C_{lr}

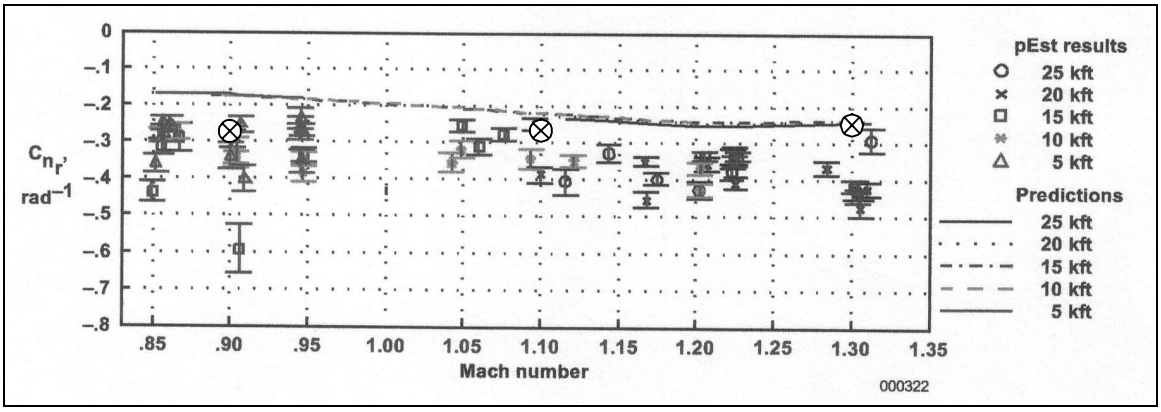

Figure 4.47: Comparison of Flight Test Data to STARS Estimates for C_{nr}

Except for the few points discussed, the decoupled boundary condition specification method accurately predicted the small rate effects. These important damping terms are sometime neglected in analysis simply due to the difficulty in predicting them. With further grid refinements and the non-inertial rate specification, even more accurate results can be expected at a moderate increase in the time investment.

Since the transpiration steady and quasi-steady values are available, the time required to converge the non-inertial solver will be reduced significantly.

The real power of this method is the ability to estimate the rate dependent stability derivatives without any prior values, excitation signals, or models. While some methods require initial values for the stability derivatives in order to produce an estimate, this method generates accurate estimates without prior knowledge. Crafting an excitation signal to properly excite the system is no longer required. And, the model type, level of convergence, and parameter identification are not potential sources of error. The level of accuracy demonstrated in the above figures and the capability to estimate, in a simple process, the stability derivatives of a full aircraft in the transonic regime in a timely and cost efficient manner is quite excellent. Theoretical methods, such as Theodorsen's are limited to simple geometries and flow regimes. Datcom methods cannot predict the stability derivatives is the transonic range for a comparison with the STARS data, as such experimental data, with its inherent uncertainty, is the only viable means of comparison. While flight-testing cannot be eliminated, given better initial estimates, the experiments can be conducted more safely and efficiently.

CHAPTER 5

CONCLUSIONS AND RECOMMENDATIONS

5.1 Conclusions

In this thesis, two computational methods for estimating the quasi-steady aircraft stability derivatives from finite element analysis were developed and examined. The first method relied heavily on experimental techniques and consisted of the following steps using the non-inertial Euler3d flow solver: excite each degree of freedom of the system with the dc-chirp, fit an ARMA model to the data, and extract the stability derivatives from the ARMA model coefficients. While this method can accurately estimate the dominate stability derivatives, the excitation required to properly identify smaller, yet still important, damping terms leads to extremely small time steps, tremendous amounts of unsteadiness, and under extreme excitation failure of the ARMA model to fit the data. This method can still be used if the unsteady model desired instead of the quasi-steady stability derivatives. As the objectives of this research were to develop a robust and efficient means for estimating stability derivatives over a broad range of Mach numbers without prior estimates, another method was sought to better capitalize on the benefits of the computational implementation.

The second method eliminated the problems of the first method by decoupling the velocity and position boundary conditions. Although it cannot be done physically, computationally, velocity and position can be excited separately. Now, the rate effects do

not have to compete with the position effect in order to be captured. The method was further refined and simplified by removing the dc-chirp and ARMA model. Instead, the steady or quasi-steady loads were determined due to a constant input angle or rate while holding the other terms constant. The derivatives are then estimated by the finite difference approximation between two converged runs at different conditions. Decoupling the boundary conditions removes the higher order terms not contained in the stability derivative analysis, and allows the effects of position and rate to be determined independently. This method accurately predicted the stability derivatives of geometries with varying levels of complexity over a broad range of Mach numbers including the transonic regime. By agreeing with fundamental theory, Datcom methods, simple predictions, and flight test data, the method of decoupled boundary condition specification has shown itself to be an accurate an efficient means of predicting stability derivatives, especially rate dependent stability derivative, which are difficult to predict.

5.2 Recommendations

For complex geometries such as the F-18, generating the computer model can require more time than the actual stability derivative analysis. In order to reduce the time, costs, and repetitiveness of this portion of the process, it is recommended that a program be written that can convert the geometry of an aircraft from a CAD program, such as CATIA or ProE, to the files necessary for generating the STARS model. Also, the time to converge a solution for a complex aircraft with a refined grid could prevent any useful investigation. As such, the benefits of domain decomposition should be investigated. If multiple computers are working the same problem simultaneously, results could be obtained in a more timely fashion.

The next logical step beyond decreasing the time required for a stability derivative analysis is the inclusion of control derivatives. This process could be very similar to the stability derivative estimation process in that the position and rate effects of the control surface could be excited independently of each other and separate from the vehicle's position and velocity. Control surface motion could be simulated through transpiration while the vehicle's motion described by the non-inertial formulation. Better estimates of the stability and control derivative will help in the design of better control laws for various configurations at various flight conditions, and discovering stability and control issues early in the design phase can save a great deal of time and resources.

BIBLIOGRAPHY

Abbott, I. H. and Von Doenhoff, A. E., *Theory of Wing Sections: Including a Summary of Airfoil Data*, Dover Publications, New York, 1959.

Berry, H. M., Batina, J. T., and Yang, T. Y., "Viscous Effects on Transonic Airfoil Stability and Response," *Journal of Aircraft*, Vol. 23, No. 5, 1986, pp. 361-369.

Boeckman, A. A., "Accelerating CFD-Based Aeroelastic Analysis Using Distributed Processing," *Master's Thesis*, Department of Mechanical and Aerospace Engineering, Oklahoma State University, 2003.

Cowan, T. J., "Efficient Aeroelastic CFD Predictions Using System Identification," *Master's Thesis*, Department of Mechanical and Aerospace Engineering, Oklahoma State University, 1998.

Cowan, T. J., "Finite Element CFD Analysis of Super-Maneuvering and Spinning Structures," *Ph.D. Dissertation*, Department of Mechanical and Aerospace Engineering, Oklahoma State University, 2003.

Dowell, E. H. (ed.), et al., *A Modern Course in Aeroelasticity*, Kluwer Academic Publishers, Dordrecht, 1995.

Falk, E. A. , *Unsteady Aerodynamics Class Notes*, Oklahoma State University, 2003.

Gupta, K. K., "STARS - An Integrated, Multidisciplinary, Finite-Element, Structural, Fluids, Aeroelastic, and Aeroservoelastic Analysis Computer Program," *NASA TM-4795*, April 2001.

Gupta, N. K. and Iliff, K. W., "Identification of Unsteady Aerodynamics and Aeroelastic Integro-Differential Systems," *NASA TM 86749*, 1985.

Hamel, P. G. and Jategaonkar, R. V., "Evolution of Flight Vehicle System Identification," *Journal of Aircraft*, Vol. 33, No. 1, 1996, pp. 9-28.

Hollkamp, J. J. and Batill, S. M., "Automated Parameter Identification and Order Reduction for Discrete Time Series Models," *AIAA Journal*, Vol. 29, No. 1, 1991, pp. 96-103.

Hunter, J. P. and Arena, A. S., "An Efficient Method for Time-Marching Supersonic Flutter Prediction Using CFD," *AIAA-97-0733*, AIAA 35th Aerospace Sciences Meeting and Exhibit, January 6-10, 1997, Reno, NV.

Iliff, K. W. and Maine R. E., "Practical Aspects of Using a Maximum Likelihood Estimation Method to Extract Stability and Control Derivatives from Flight Data," *NASA TN D-8209*, April 1976.

Kandil, O. A., and Chuang, H. A., "Computation of Vortex-Dominated Flow for a Delta Wing Undergoing Pitching Oscillations," *AIAA Journal*, Vol. 28, No. 9, September 1990, pp. 1589-1595.

Katz, J. and Plotkin, A., *Low-Speed Aerodynamics*, 2nd Ed. Cambridge University Press, 2001.

Klein, V., Murphy P. C., Curry, T. J., and Brandon, J. M., "Analysis of Wind Tunnel Longitudinal Static and Oscillatory Data of the F-16XL Aircraft," *NASA TM-97-206276*, December 1997.

Klein, V. and Murphy P. C., "Aerodynamic Parameters of High Performance Aircraft Estimated from Wind Tunnel and Flight Test Data," *AGARD Symposium on*

System Identification for Integrated Aircraft Development and Flight Testing, May 5-8, 1998, Madrid, Spain.

Moes, T. R., Noffz, G. K., and Iliff K. W., "Results From F-18B Stability and Control Parameter Estimation Flight Tests at High Dynamic Pressures," *NASA TP-2000-209033*, November 2000.

Nelson, R. C., *Flight Stability and Automatic Control*, 2nd Ed. McGraw-Hill, Boston, 1998.

O'Neill, C. R., "Improved System Identification for Aeroservoelastic Predictions," *Master's Thesis*, Department of Mechanical and Aerospace Engineering, Oklahoma State University, 2003.

Park, M. A., Green, L. L., Montgomer, R. C., and Raney, D. L., "Determination of Stability and Control Derivatives Using Computational Fluid Dynamics and Automatic Differentiation," *AIAA 99-3136*, June 1999.

Pesonen, U. J., Agarwal, R. K., and Laine, S., "Fast and Robust Viscous/Inviscid Interaction Code for Wing Flowfield Calculations," *Journal of Aircraft*, Vol. 37, No. 4, 2000, pp. 730-733.

Prabhu, R. K., "An Inviscid Computational Study of the X-33 Configuration at Hypersonic Speeds," *NASA CR 209366*, July 1999.

Stephens, C. H. and Arena, A. S., "Application of the Transpiration Method for Aeroservoelastic Prediction Using CFD," *AIAA Paper 98-2071*, 39th AIAA/ASME/ASCE/AHS/ASC Structures, Structural dynamics, and Materials Conference, April, 1998 Long Beach, CA.

USAF Stability and Control DATCOM, Flight Control Division, Air Force Flight Dynamics Laboratory, Wright-Patterson Air Force Base, Fairborn, OH.

White, F. M., *Viscous Fluid Flow*, 2nd Ed. McGraw-Hill, Boston, 1991.

APPENDIX A:

THIN AIRFOIL THEORY FOR CONSTANT PITCH RATE

The notation for thin airfoil theory equations is represented in the following figure of a thin flat plate with the origin at the leading edge. The origin of rotation is shown with the positive orientation for pitch rate q. The distance from the leading edge to the origin of rotation is positive l for rotation aft of the leading edge and negative fore of the leading edge. The chord length is represented by c.

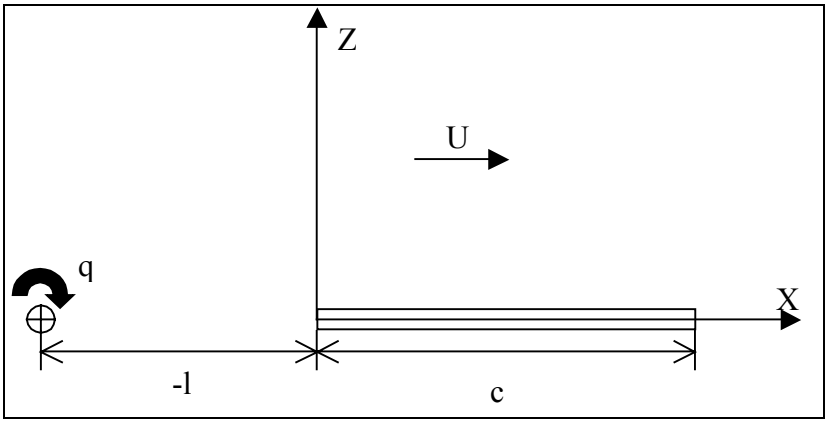

Following the standard process for thin airfoil theory, the equivalent camber can be described by the equation below assuming small angle approximation for angle of attack, alpha.

$$\frac{dz}{dx} = \tan\frac{v}{U} \approx \frac{v}{U} = \frac{q \cdot (l - x)}{}$$

Using the standard coordinate transformation x = c / 2 * (1 - cos(θ)), the above expression becomes the following.

$$\frac{dz}{dx} = \frac{q \cdot (l)}{U} - \frac{qc}{2U} \cdot (1 - \cos\theta)$$

This equation is evaluated in the standard thin airfoil theory equations for A_0, A_1, and A_2, the results of which are used in the C_{mLE} and C_l equations, all of which are repeated below with a general C_m equation for the moment about the rotation point.

$$A_0 = \alpha - \frac{1}{\pi}\int_0^{\pi} \frac{dz}{dx} \cdot d\theta, \quad A_1 = \frac{2}{\pi}\int_0^{\pi} \frac{dz}{dx} \cdot \cos\theta \cdot d\theta, \quad \text{and} \quad A_2 = \frac{2}{\pi}\int_0^{\pi} \frac{dz}{dx} \cdot \cos 2\theta \cdot d\theta$$

$$C_{mLE} = -\frac{\pi}{2}\left[A_0 + A_1 - \frac{A_2}{2}\right], \quad C_l = 2\pi\left[A_0 + \frac{A_1}{2}\right], \quad \text{and} \quad C_m = C_{mLE} + C_l \cdot \frac{l}{c}$$

With the equivalent camber definition at zero angle of attack, the above equation evaluate to the following.

$$A_0 = \frac{qc}{2U} - \frac{ql}{U}, \qquad A_1 = \frac{qc}{2U}, \qquad \text{and} \qquad A_{21} = 0$$

$$C_m = \frac{-2\pi c}{U}\left[\left(\frac{l}{c}\right) - \frac{1}{2}\right]^2$$

Finally, the stability derivative C_{mq} is as follows.

$$C_{mq} = \frac{dC_m}{dq} \cdot \frac{2U}{c} = -4\pi\left[\left(\frac{l}{c}\right) - \frac{1}{2}\right]^2$$

APPENDIX B:

DATCOM CALCULATIONS FOR ISOLATED SURFACES

The following is the MathCAD workspace used to calculate the Datcom estimates for the stability derivatives of the isolated surfaces. The page numbers for the equations obtained from the Datcom are presented next to the equation. The subscript w refers to the wing, v refers to the vertical tail, and h refers to the horizontal tail.

Input parameters and initial calculations:

$Ma := .4$ $\quad U_0 := 13392 \cdot Ma$ $\quad roe := 1.146 \times 10^{-7}$

$S_w := 16$ $\quad S_v := 6$ $\quad S_h := 6$ $\quad cbar_w := 2$ $\quad Q := .5 \cdot roe \cdot U_0^{\,2}$ $\quad B := \left(1 - Ma^2\right)^{.5}$

$b_w := 8$ $\quad b_h := 4$ $\quad b_v := 3$ $\quad z_v := \frac{3}{2}$ $\quad l_v := 9.5$ $\quad l_h := 8.875$ $\quad l_w := .5$

$AR_w := \frac{b_w^{\,2}}{S_w}$ $\quad AR_h := \frac{b_h^{\,2}}{S_h}$ $\quad AR_v := \frac{b_v^{\,2}}{S_v}$ $\quad gama := 5 \cdot \frac{\pi}{180}$ $\quad z_w := .5 - \frac{b_w}{2} \cdot \frac{\sin(gama)}{2}$

$C_{lalpha} := .109 \cdot \frac{180}{\pi}$ $\quad C_{lalpha.Ma} := \frac{C_{lalpha}}{B}$ 4.1.1.2-1

$k := \frac{C_{lalpha.Ma} \cdot B}{2 \cdot \pi}$ 4.1.3.2-3

$qsweep_w := 0$ $\quad halfsweep_w := 0$ $\quad halfsweep_h := atan\left(\frac{1}{8}\right)$ $\quad halfsweep_v := atan\left(\frac{1}{3}\right)$

$$C_{Lalpha.w} := \frac{AR_w \cdot 2 \cdot \pi}{2 + \sqrt{\left(AR_w \cdot \frac{B}{k}\right)^2 \cdot \left[1 + \frac{\left(\tan\left(halfsweep_w\right)\right)^2}{B^2}\right] + 4}}$$

4.1.3.2-49

$C_{Lalpha.w} = 4.056$

$$C_{Lalpha.v} := \frac{AR_v \cdot 2 \cdot \pi}{2 + \sqrt{\left(AR_v \cdot \frac{B}{k}\right)^2 \cdot \left[1 + \frac{\left(\tan\left(halfsweep_v\right)\right)^2}{B^2}\right] + 4}}$$

$C_{Lalpha.v} = 2.102$

$$C_{Lalpha.h} := \frac{AR_h \cdot 2 \cdot \pi}{2 + \sqrt{\left(AR_h \cdot \frac{B}{k}\right)^2 \cdot \left[1 + \frac{\left(\tan\left(halfsweep_h\right)\right)^2}{B^2}\right] + 4}}$$

$C_{Lalpha.h} = 3.23$

Longitudinal Stability Derivative Calculations:

$$C_{malpha.w} := \frac{-l_w \cdot C_{Lalpha.w}}{cbar_w} \qquad 4.1.4.2\text{-}1$$

$$C_{malpha.w} = -1.014$$

$$C_{malpha.h} := \frac{-l_h \cdot C_{Lalpha.h}}{cbar_w} \cdot \frac{S_h}{S_w} \qquad 4.5.2.1\text{-}2$$

$$C_{malpha.h} = -5.375$$

$$C_{malpha} := C_{malpha.w} + C_{malpha.h}$$

$$C_{malpha} = -6.389$$

$$C_{mq.w} := -.7 \cdot C_{lalpha} \cdot \cos\left(qsweep_w\right) \cdot \left[AR_w \cdot \frac{\left[.5 \cdot \frac{l_w}{cbar_w} + 2 \cdot \left(\frac{l_w}{cbar_w} \right)^2 \right]}{AR_w + 2 \cdot \cos\left(qsweep_w\right)} + 0 + \frac{1}{8} \right] \cdot \frac{1}{B} \qquad 7.1.1.2\text{-}2$$

$$C_{mq.w} = -1.391$$

$$C_{mq.h} := -2 \cdot \left(\frac{l_h}{cbar_w} \right)^2 \cdot \frac{S_h}{S_w} \cdot C_{Lalpha.h} \qquad 7.4.1.2\text{-}1$$

$$C_{mq.h} = -47.703$$

$$C_{mq} := C_{mq.w} + C_{mq.h}$$

$$C_{mq} = -49.095$$

Yaw Moment Stability Derivative Calculations:

$C_{nbeta.w} := 0$ at zero lift 5.1.3.1-1

$$C_{ybeta.v} := -C_{Lalpha.v} \cdot \frac{S_v}{S_w} \qquad 5.3.1.1\text{-}3$$

$$C_{nbeta.v} := -C_{ybeta.v} \cdot \frac{l_v}{b_w} \qquad 5.6.3.1\text{-}1$$

$$C_{nbeta.v} = 0.936$$

$$C_{nbeta} := C_{nbeta.w} + C_{nbeta.v}$$

$$C_{nbeta} = 0.936$$

$C_{nr.w} := 0$ at zero lift 7.1.3.3-2

$$C_{nr.v} := 2 \cdot \left(\frac{l_v}{b_w} \right)^2 \cdot C_{ybeta.v} \qquad 7.4.3.3\text{-}1$$

$$C_{nr.v} = -2.223$$

$$C_{nr} := C_{nr.w} + C_{nr.v}$$

$$C_{nr} = -2.223$$

Roll Moment Stability Derivative Calculations:

$$dihedeff := -.00015 - \frac{.00005}{3} \qquad 5.1.2.1-29$$

$$compcor := 1 + \frac{.1}{4} \qquad 5.1.2.1-30a$$

$$C_{lbeta.w} := gama \cdot dihedeff \cdot \frac{180^2}{\pi^2} \cdot compcor \qquad \text{at zero aoa} \quad 5.1.2.1-2$$

$$C_{lbeta.w} = -0.049$$

$$C_{lbeta.v} := C_{ybeta.v} \cdot \frac{z_v}{b_w} \qquad \text{at zero aoa} \qquad 5.3.2.1-2$$

$$C_{lbeta.v} = -0.148$$

$$C_{lbeta} := C_{lbeta.w} + C_{lbeta.v}$$

$$C_{lbeta} = -0.197$$

$$C_{lr.w} := 0 \qquad \text{negligible at zero aoa} \qquad 7.1.3.2-1$$

$$C_{lr.v} := -2 \cdot l_v \cdot z_v \cdot \frac{C_{ybeta.v}}{b_w^2} \qquad 7.4.3.2-1$$

$$C_{lr.v} = 0.351$$

$$C_{lr} := C_{lr.w} + C_{lr.v}$$

$$C_{lr} = 0.351$$

APPENDIX C:

DATCOM CALCULATIONS INCLUDING INTERFERENCE

The following is the MathCAD workspace used to calculate the Datcom estimates for the stability derivatives including the available interference approximations. The page numbers for the equations obtained from the Datcom are presented next to the equation. The subscript w refers to the wing, v refers to the vertical tail, and h refers to the horizontal tail.

Input parameters and initial calculations:

$Ma := .4$ $\quad U_0 := 13392 Ma$ $\quad roe := 1.146 \times 10^{-7}$

$S_w := 16$ $\quad S_v := 6$ $\quad S_h := 6$ $\quad cbar_w := 2$ $\quad Q := .5 \cdot roe \cdot U_0^{\,2}$ $\quad B := \left(1 - Ma^2\right)^{.5}$

$b_w := 8$ $\quad b_h := 4$ $\quad b_v := 3$ $\quad z_v := \frac{3}{2}$

$l_v := 9.5$ $\quad l_h := 8.875$ $\quad l_w := .5$

$gama := 5 \cdot \frac{\pi}{180}$ $\quad z_w := .5 - \frac{b_w}{2} \cdot \frac{\sin(gama)}{2}$

$AR_w := \frac{b_w^{\,2}}{S_w}$ $\quad AR_h := \frac{b_h^{\,2}}{S_h}$ $\quad AR_v := \frac{b_v^{\,2}}{S_v}$

$C_{lalpha} := .109 \frac{180}{\pi}$ $\quad C_{lalpha.Ma} := \frac{C_{lalpha}}{B}$ 4.1.1.2-1 $\quad k := \frac{C_{lalpha.Ma} \cdot B}{2 \cdot \pi}$ 4.1.3.2-3

$qsweep_w := 0$ $\quad halfsweep_w := 0$ $\quad halfsweep_h := atan\left(\frac{1}{8}\right)$ $\quad halfsweep_v := atan\left(\frac{1}{3}\right)$

$$C_{Lalpha.w} := \frac{AR_w \cdot 2 \cdot \pi}{2 + \sqrt{\left(AR_w \cdot \frac{B}{k}\right)^2 \cdot \left[1 + \frac{\left(\tan\left(halfsweep_w\right)\right)^2}{B^2}\right] + 4}}$$ 4.1.3.2-49

$C_{Lalpha.w} = 4.056$

$$C_{Lalpha.h} := \frac{AR_h \cdot 2 \cdot \pi}{2 + \sqrt{\left(AR_h \cdot \frac{B}{k}\right)^2 \cdot \left[1 + \frac{\left(\tan\left(halfsweep_h\right)\right)^2}{B^2}\right] + 4}}$$

$C_{Lalpha.h} = 3.23$

Longitudinal Stability Derivative Calculations:

$$C_{malpha.w} := \frac{-l_w \cdot C_{Lalpha.w}}{cbar_w} \qquad 4.1.4.2\text{-}1$$

$$C_{malpha.w} = -1.014$$

$$down\_wash := .38785 \qquad 4.4.1 - 7$$

$$C_{malpha.h} := \frac{-l_h \cdot C_{Lalpha.h}}{cbar_w} \cdot \frac{S_h \cdot (1 - down\_wash)}{S_w} \qquad 4.5.2.1\text{-}2$$

$$C_{malpha.h} = -3.29$$

$$C_{malpha} := C_{malpha.w} + C_{malpha.h}$$

$$C_{malpha} = -4.304$$

$$C_{mq.w} := -.7 \cdot C_{lalpha} \cdot \frac{\cos(qsweep_w)}{B} \cdot \left[\frac{AR_w \cdot \left[.5 \cdot \frac{l_w}{cbar_w} + 2 \cdot \left(\frac{l_w}{cbar_w} \right)^2 \right]}{AR_w + 2 \cdot \cos(qsweep_w)} + 0 + \frac{1}{8} \right] \qquad 7.1.1.2\text{-}2$$

$$C_{mq.w} = -1.391$$

$$C_{mq.h} := -2 \cdot \left(\frac{l_h}{cbar_w} \right)^2 \cdot \frac{S_h}{S_w} \cdot C_{Lalpha.h} \qquad 7.4.1.2\text{-}1$$

$$C_{mq.h} = -47.703$$

$$C_{mq} := C_{mq.w} + C_{mq.h}$$

$$C_{mq} = -49.095$$

Yaw Moment Stability Derivative Calculations:

$C_{nbeta.w} := 0$ at zero lift 5.1.3.1-1

$body_{intfer} := 1$ $htail_{intfer} := .9$ $K_H := .9$ 5.3.1.1-22

$$AR_{v.eff} := body_{intfer} \cdot AR_v \cdot \left[1 + K_H \cdot \left(htail_{intfer} - 1\right)\right]$$ 5.3.1.1-2

$$AR_{v.eff} = 1.365$$

$$C_{Lalpha.v} := \frac{AR_{v.eff} \cdot 2 \cdot \pi}{2 + \sqrt{\left(AR_{v.eff} \cdot \frac{B}{k}\right)^2 \cdot \left[1 + \frac{\left(\tan\left(halfsweep_v\right)\right)^2}{B^2}\right] + 4}}$$

$$side\_wash := .724 + 3.06 \frac{\left(\frac{S_v}{S_w}\right)}{1 + \cos\left(qsweep_w\right)} + 0 + .009 \cdot AR_w$$ 5.4.1-1

$$C_{ybeta.v} := -C_{Lalpha.v} \cdot \frac{S_v \cdot (side\_wash)}{S_w}$$ 5.3.1.1-3

$$C_{nbeta.v} := -C_{ybeta.v} \cdot \frac{l_v}{b_w}$$ 5.6.3.1-1

$$C_{nbeta.v} = 1.156$$

$$C_{nbeta} := C_{nbeta.w} + C_{nbeta.v}$$

$$C_{nbeta} = 1.156$$

$C_{nr.w} := 0$ at zero lift 7.1.3.3-2

$$C_{nr.v} := 2 \cdot \left(\frac{l_v}{b_w}\right)^2 \cdot C_{ybeta.v}$$ 7.4.3.3-1

$$C_{nr.v} = -2.745$$

$$C_{nr} := C_{nr.w} + C_{nr.v}$$

$$C_{nr} = -2.745$$

Roll Moment Stability Derivative Calculations:

$$dihedeff := -.00015 - \frac{.00005}{3} \qquad 5.1.2.1-29$$

$$compcor := 1 + \frac{.1}{4} \qquad 5.1.2.1-30a$$

$$C_{lbeta.w} := gama \cdot dihedeff \cdot \frac{180^2}{\pi^2} \cdot compcor \qquad \text{at zero aoa} \quad 5.1.2.1-2$$

$$C_{lbeta.w} = -0.049$$

$$C_{lbeta.v} := C_{ybeta.v} \cdot \frac{z_v}{b_w} \qquad \text{at zero aoa} \qquad 5.3.2.1-2$$

$$C_{lbeta.v} = -0.183$$

$$C_{lbeta} := C_{lbeta.w} + C_{lbeta.v}$$

$$C_{lbeta} = -0.231$$

$$C_{lr.w} := 0 \qquad \text{negligible at zero aoa} \qquad 7.1.3.2-1$$

$$C_{lr.v} := -2 \cdot l_v \cdot z_v \cdot \frac{C_{ybeta.v}}{b_w^2} \qquad 7.4.3.2-1$$

$$C_{lr.v} = 0.433$$

$$C_{lr} := C_{lr.w} + C_{lr.v}$$

$$C_{lr} = 0.433$$

VITA

Deric Austin Babcock

Candidate for the Degree of

Master of Science

Thesis: AIRCRAFT STABILITY DERIVATIVE ESTIMATION FROM FINITE ELEMENT ANALYSIS

Major Field: Aerospace Engineering

Biographical:

Personal Data: Born in Kingfisher, Oklahoma on July 21, 1980, the son of Larry R. Babcock and Sandra G. Babcock.

Education: Graduated from Lone Grove High School, Lone Grove Oklahoma, in May 1998; received Bachelor of Science degree majoring in Mechanical and Aerospace Engineering from Oklahoma State University, Stillwater, Oklahoma, in May 2002; completed the requirements for the Master of Science degree in Mechanical Engineering at Oklahoma State University in July 2004.

Experience: Tutor, Mathematics Learning Resource Center, 1999-2001; Teaching Assistant, OSU Mechanical and Aerospace Engineering Department, 2002-2004; Research Assistant, OSU MAE Dept. 2003-2004.

Professional Memberships: American Institute of Aeronautics and Astronautics, American Society of Mechanical Engineers, Sigma Gamma Tau.